UNIVERSITY OF CATANIA

DEPARTMENT OF CHEMICAL SCIENCES

PhD Course in

MATERIALS SCIENCE AND NANOTECHNOLOGIES

XXXIII CYCLE

Angelo Nicosia

Polymer-based Graphene Oxide Derivatives as a tunable multi-purpose platform

DOCTORAL THESIS

PhD Coordinator: ***Prof. Giuseppe Romano Compagnini***

Supervisor: ***Prof. Placido Giuseppe Mineo***

ACADEMIC YEAR 2019-2020

Table of Contents

Biographical note on the Author

Angelo Nicosia studied at the University of Catania, where obtained both Bachelor (2014) in Industrial Chemistry (110 cum laude), working on the synthesis and the characterization of acrylic copolymers able to molecular sensing, and M.Sc. degree (2017) in Materials Chemistry (110 cum laude), with the thesis title: "Spontaneous symmetry breaking in aggregates of porphyrin-based polymers: effect of building block structure, physical parameters and chirality induction".

From November 2017, he joined the doctoral program in Materials Science and Nanotechnology (Dept. of Chemical Science, University of Catania), supervised by Prof. P. Mineo. His doctoral research has focused on the synthesis and characterization of graphene oxide polymer derivatives, aiming to produce advanced functional materials suitable for several applications.

During the three year program, he has been a visiting PhD student at TU/e (Eindhoven, NL) in the group of Supramolecular Polymer Chemistry, headed by Prof. R. Sijbesma, where he deepened his knowledge about the advanced properties of Graphene Oxide-Polymer blends.

1 Introduction

Graphene was firstly discovered by Geim and Novoselov in 2004, while graphene was assumed to be unstable in the free state. It was extracted by peeling (through a scotch-tape) from a highly oriented pyrolytic graphite block, obtaining single-layer and few-layers graphene.[1] From its discovery, and the disclosure of its properties, the graphene "gold rush" produced plenty of publications concerning different research fields.

The graphene is theoretically defined as a 2D crystal composed of a single layer carbon honeycomb structure. It is described as a zero-gap semiconductor, with a simple electronic structure and composed of one type of electrons and one type of holes, as charge carriers. The nature of these charge carriers, which interact with the periodic potential of the graphene lattice, is relativistic; so they are described as Dirac fermions moving at the speed of light in a ballistic mode.[2] Nevertheless, the electronic properties of graphene are maintained until the limit of 10 layers, when the graphite electronic properties appear.[3]

In addition to the unique electrical conductivity, graphene also exhibits mechanical flexibility and optical transparency:[4] these features pave the way for a plethora of applications in electronic devices[5] such as transistors,[6] new generation batteries,[7,8] flexible electronic circuits,[9,10] dye-sensitized solar cells.[11,12]

From a physical point of view, graphene is defined as a strong material, thanks to the Young modulus of 1 TPa and the breaking strength of 42 N/m.[13] It is also an incredible thermal conductor thanks to its conductivity value of about 5000 $W*m^{-1}*K^{-1}$,[14] with a negative coefficient of thermal expansion.[15] Moreover, it is impermeable to gases such as helium,[16] making it feasible for application as membrane.[17]

The graphene applications are not circumscribed to electronics. Since this carbon-based honeycomb has shown high efficacy in protecting metals from oxidation,[18] it is also applied as corrosion-inhibiting coatings.[19] Moreover, it has been also involved in innovative applications in polymer nanocomposites, drug delivery, theranostic,[20] water remediation,[21,22] and photocatalysis.[23]

Nevertheless, all of these applications are feasible thanks to interesting and various functionalizations of the graphene moiety. So, a variety of chemical and physical functionalizations of this carbon platform[24] allows us to exploit the graphene properties making it extremely versatile in many research fields.

Graphene is produced essentially through: mechanical exfoliation of graphite, chemical vapour deposition, liquid phase exfoliation and epitaxial growth. It is noteworthy to highlight that these methods are useful for small scale production, because of the costs and the production rate.

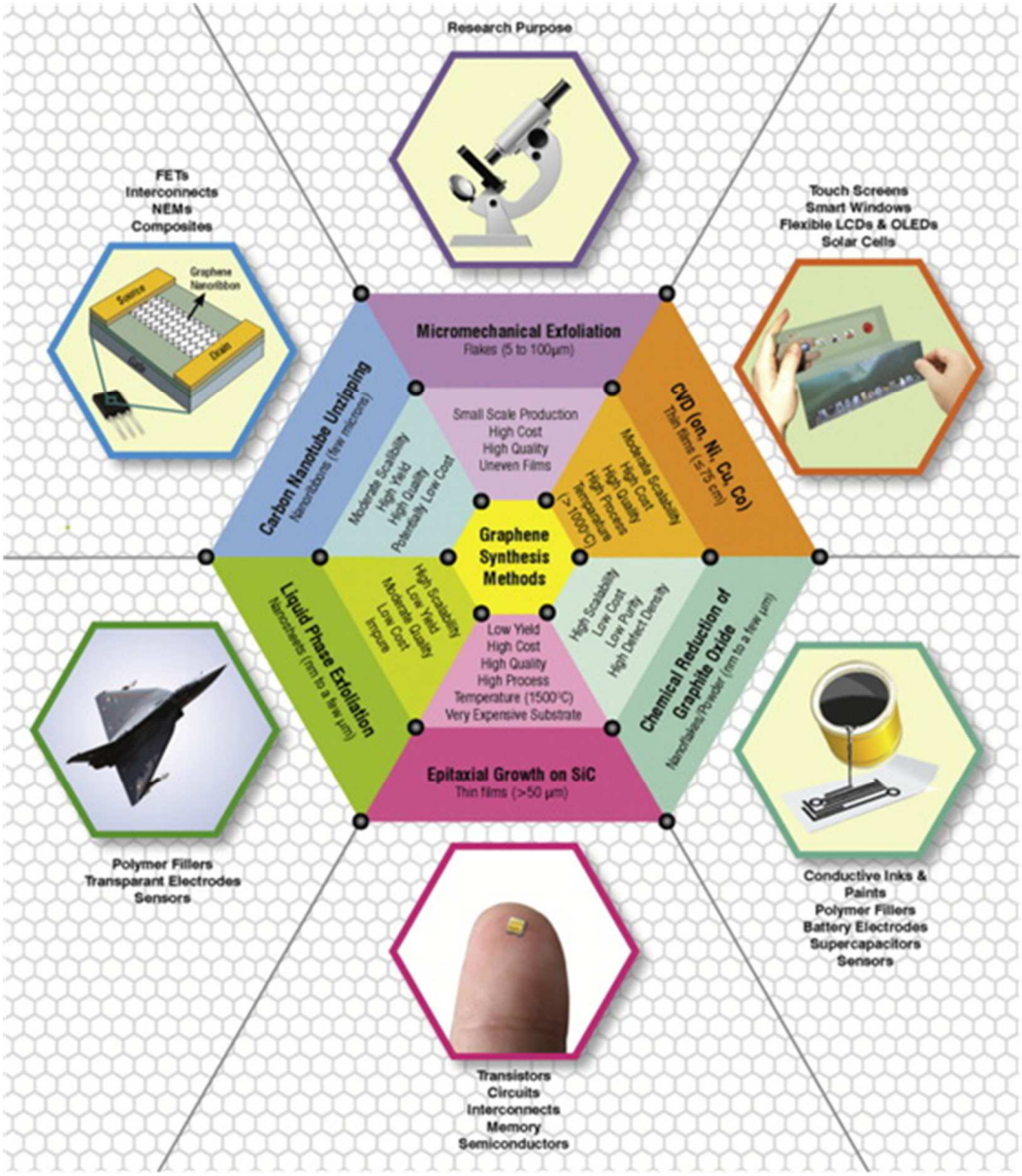

Figure 1.1 Schematic illustration of the Graphene Synthesis Methods and of their features and applications. The image was taken from Mittal et al.[25]

Despite the graphene amazing chemical-physical features, there are issues concerning the production of graphene as self-standing sheets, due to its spontaneous aggregation driven by Van der Waals forces. In particular, there is difficulty in large scale production of stable graphene suspension without the use of surfactants or polymers to stabilize it.[26] From a chemistry point of view, handling the Graphene in suspension or solution is also useful to make easier any further functionalization of its carbon structure. So, the most common and facile way to produce graphene is the chemical reduction of Graphene Oxide (GO).

Thus, GO has become the most diffused Graphene derivative and, due to its features, it has been chosen as the keystone of this thesis.

1.1 Graphene Oxide

To understand the origin of the Graphene Oxide (GO), it is necessary to look back in scientific research history and focus on the study related to its precursor material, the graphite, and its oxidation. The first work about the oxidation of graphite was published by Schafhaeutl in 1840.[27-29] The graphite oxidation is a useful method to increase the interlayer distance of the graphene moieties. The further increase of the interlayer distance thanks to the intercalation/solvation, and the consequent stabilization of the sheets composed by few- and mono-layers, gave rise to a new material which will later be called GO.

Different graphite oxidation methods were developed among the years, and one of the most common is the Hummers and Offemann.[30]

This method concerns the graphite flakes oxidization by treatment with sodium nitrate, sulphuric acid, potassium permanganate and, finally, hydrogen peroxide. The obtained Graphite Oxide needs further exfoliation procedures, such as ultrasonication, to achieve the separation of the layers up to single or few-layers Graphene Oxide (Figure 1.2). This method has gained success in the GO research due to its easiness and less toxic by-product compared to the other synthetic methods.[31]

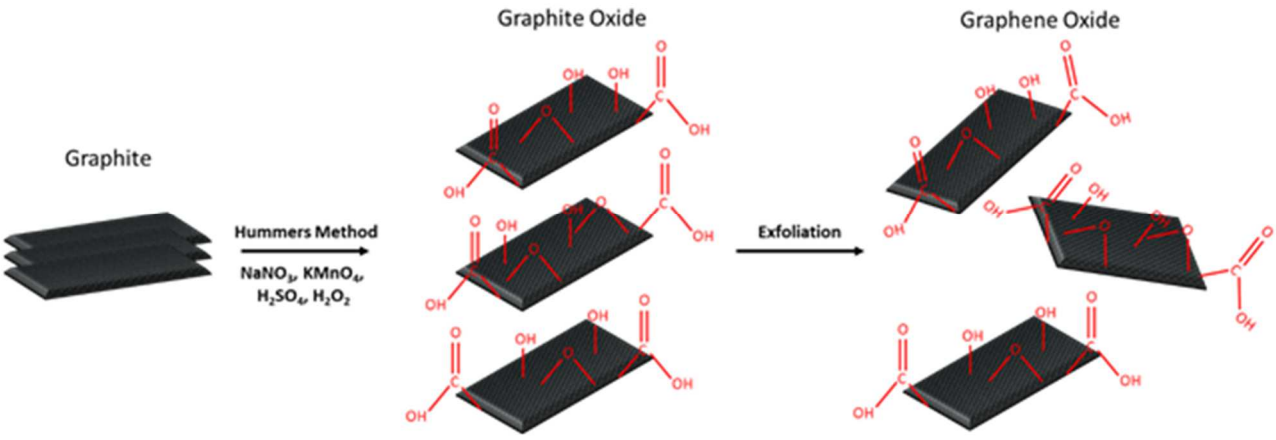

Figure 1.2 Schematic illustration of Graphene Oxide synthesis.

It is noteworthy to say that the GO is a not-well standardized material because its structure and the relative amount of functional groups strictly depends on the synthetic procedure and the starting material as well. Indeed, the flake graphite is a complex material which has intrinsic defects due to its origin (natural or synthetic).[32] Since the oxidation reaction affects unsaturated aliphatic double bonds,[33] the defects in the aromatic π-structure of the graphite are fundamental to determine the characteristics and structure of the GO, strongly influencing the synthetic repeatability.

Several studies have challenged to define the structure of GO.[34] One of the most accepted model structures is the one which has epoxides and hydroxyl groups randomly spread on the carbon platform, while the carboxylic acid groups are located in the edges. Thus, such structure composed of aromatic regions and aliphatic moieties, containing also isolated double bonds, results in a nearly flat platform surrounded by oxygen layers on both sides (Figure 1.3).[35]

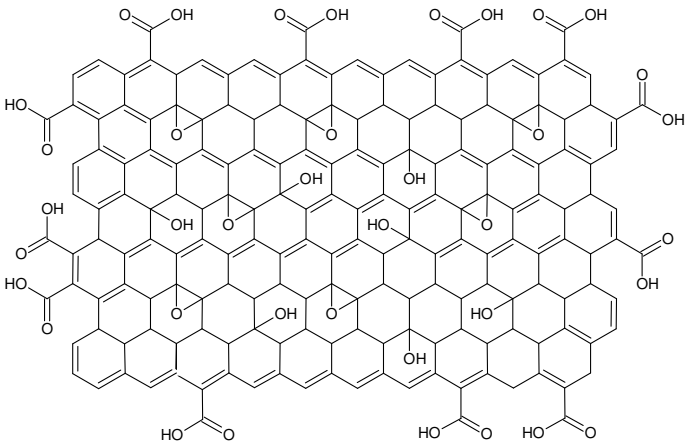

Figure 1.3 Graphene Oxide, an exemplification of structure.

The strong oxidation leads to a hydrophilic material. It is known to be stable in water dispersion as mono- and few-layers GO, but it is also stable in some common polar organic solvents.[36] This evidence is reasonably attributable to the oxygen functional groups which help to stabilize the GO suspension avoiding the aggregation, thanks to the electrostatic repulsion of the partially negative charged oxygen moieties.

This unique structure enables several approaches to further functionalize this carbon platform. There are three main approaches:[37]

- *non-covalent functionalization* employing hydrophobic, electrostatic, and Van der Waals forces due to the sp^2 carbon structure of GO;
- *covalent functionalization* through electrophilic substitution or cycloaddition reactions,[38] involving the sp^2 carbon platform and the alkenes double bonds;
- *covalent functionalization* of the oxygen functional groups, which could also be conducted selectively on one of the three types: epoxide, hydroxyl and carboxylic groups.[34]

Nevertheless, the oxidation of the sp^2 graphitic carbon structure disrupts the conjugation and gives rise to the insulating capability of the GO, in contrast with Graphene. Since the electrical conductivity

is one of the most interesting features of Graphene moieties, the reduction of the GO results as a fundamental reaction to recover the electrical properties typical of the graphite lattice.

As an example, recently GO has been found out suitable for conductive ink production.[39,40] Ink-jet printing represents a potential method for industrial scalable production of flexible electronics,[41] that represent the new era of electronics. Since GO suspension exhibits stability in both water and organic polar solvents,[42] GO-based inks do not need any stabilizing agents in contrast with Graphene-based.[43] Suitable solvents for GO-based inks are water or water/methanol mixture.[10,39,44-46] Despite everything, further reduction of the GO printed film is fundamental to achieve conductivity.[10,43,46]

Nevertheless, the so-called reduced-GO (rGO) will never be able to fully recover the conductivity related to the pristine Graphene platform. Indeed, it is noteworthy to say that some structural defects in GO structure occurring during the oxidation process (holes on the grid) are not recoverable through the reduction.

The rGO could be obtained through thermal reduction or chemical reduction. In literature, many variations on these two reduction methods were reported.[47] The chemical reduction is low cost and user-friendy: indeed, there is no need to use high temperature and/or special equipment (in contrast to the thermal reduction); moreover, it is easily scalable, and all of these features make the chemical reduction the most commonly used method. Several methods were proposed in literature,[47] and they differ from the type of reductant used and the reaction conditions. Nevertheless, the most accepted and widespread approach is the use of hydrazine as a reducing agent.

An in-depth discussion about the reduction procedures and mechanisms is elsewhere reported (see Chapter 5.1).

All of the functionalization pathways here reported are useful to obtain Graphene-based advanced functional materials.

Among all the possible functionalization, the Graphene-Polymer composites represent one of the most interesting, thanks to the huge extent of features and chemical-physical properties of polymers. In the following section will be discussed some of the GO features and their synergy with polymers.

1.2 Graphene polymer derivatives

The polymer functionalization of the graphene platform introduces new interesting features to the ones of the Graphene, thus proposing new insights to several areas of materials science.[48] The graphene-polymer nanocomposites are suitable for applications in microelectronics, photocatalysis, molecular sensing, drug delivery, theranostic, dye-sensitized solar cells, coatings and material for special uses.

Moreover, as a nanofiller, graphene could also improve the mechanical properties of the Polymer. This feature is attributed to the load transfer from polymer to the carbon platform and is highly influenced by the intensity of the interfacial interaction. Nevertheless, a limiting factor for the application of Graphene and GO as nanofillers is due to their tendency to aggregate: this results in inhomogeneous dispersion within the polymer matrices, weakening the interfacial interactions. Thus, GO functional groups have been exploited to produce highly compatible nanofillers to improve bulk polymer properties.[49,50]

Although the structural defects of GO influence its intrinsic electrical properties, they could be exploited in molecular sensing. In particular, the valence band of reduced-GO is influenced by the adsorption of oxidative (or reducing) gaseous molecules, altering the number of holes and the conductivity, consequently.[51,52]
The sensing capability of the Graphene moiety could be improved synergistically by blending it with suitable functional polymers. These last could act as an adsorbent layer for gaseous molecules, or as a dopant. As an example, it has been demonstrated that GO embedded within conductive polymers (i.e. polyaniline) acts as a conductivity enhancer, due to the π-π stacking with the conjugated polymer and to its influences on the polymer conformation. The interaction of a suitable vapour molecule (i.e. methanol) with the polymer induces conformational changes due to hydrogen bonds, which increase the resistivity of the composite.[53]

GO has been revealed as an acceptor in Förster resonance energy transfer (FRET). Its high long-distance energy transfer rate (inversely proportional to the fourth power of distance),[54,55] implicates that the fluorescence of a dye is quenched only when it is spatially close to the GO platform. The FRET property of GO could be matched with the sensitivity of stimuli-responsive polymers to produce sensors. In particular, a fluorescent dye bonded to a stimuli-responsive polymer will be subjected, or not, to the FRET mechanism depending on the elongated or shrunk polymer conformation (Figure 1.4). These mechanisms have been exploited to produce colorimetric pH- and thermo-sensors.[56-58]

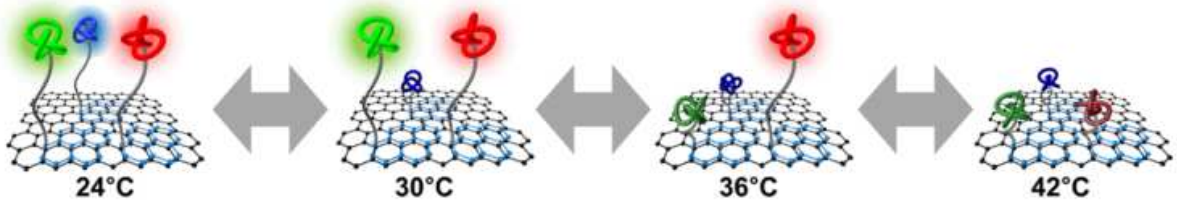

Figure 1.4 Scheme of a polymer functionalized GO colorimetric thermosensor. The image has been taken from Yang et al.[58]

Reduced GO has shown high absorption in the Near-Infrared Region (NIR), correlated to high photothermal conversion efficiency. It has been shown that reduction processes induce aggregation of oxygen atoms at the edge of the defects, also producing cyclic edge ether which are the most stable oxygenated species of the graphene. The free electrons located in the proximity of the oxygen gives rise to forced resonant vibration processes,[59] converting NIR radiation energy to heat. The NIR-responsive behaviour of graphene has been widely exploited in different fields.

GO-based polymer composites have been used to produce light-induced healing materials, both structural polymers or hydrogels.[60,61] In particular, the self-healing occurs when the material is subjected to NIR energy because of the conversion from irradiation energy to heat, which promotes the polymer chains mobility and the consequent interchain diffusion across the cropped surface.

Graphene platform has also been used in biological applications, such as drug delivery. Since common drugs are aromatic and insoluble in water, a compatibilizer is needed to perform their direct delivery within a biological environment. Thanks to the high surface area sp^2 hybridized and its water stability, GO represents a powerful drug carrier. Nevertheless, GO exhibits cytotoxicity that relies on several parameters, such as layer thickness, size, dose, and occurs through different mechanisms.[62]

In this frame, the polymer functionalization of the GO is needed for a double reason: it reduces the intrinsic GO citotoxicity[63] and improves its solubility in biological media and the cell viability.[64]

Anyway, polymer functionalized-GO has shown high loading of doxorubicin, an aromatic anticancer drug, through π-π stacking and hydrophobic interactions.[65]

Since NIR radiation could deeply penetrate biological tissues, it can be used as a trigger to perform stimuli-triggered drug release.[66] Thus, the induced heating of the GO platform modifies the binding energy of the drug, triggering its release within the biological environment.[65] Moreover, the heating of the GO sheets is suitable for photothermal therapy.[67] It has been found that the combination of drug release and photothermal therapy operated by GO results in higher efficiency in terms of tumor recurrence than that detected by using only drugs or only photothermal therapy.[68]

Noteworthy, if targeting agents are bond to the polymer targeted cell treatments could be performed.[67]

Although GO bio-compatibility allows biological treatments, it is known also as a powerful antimicrobial agent.[69,70] The GO activity towards bacteria has been described as dual: membrane and oxidative stress. Indeed, the cell deposition occurs through the GO oxygenated functional groups; then, through direct contact, the membrane stress occurs by disrupting and damaging the bacteria cell membrane, while induces oxidative stress. In this last case, rGO is more efficient than GO.[71] Anyway, this feature makes GO a suitable tool for antibacterial coatings which are fundamental in biomedical applications, as it represents a green, biocompatible and cheap substitute to the common antibacterial agents and or silver coatings.[72] It has been verified that polymer coatings containing a suitable amount of GO could prevent the metal substrate from oxidation and bacterial adhesion, meanwhile maintaining a positive cell adhesion and response exploitable for surgery implants.[73]

Electronic properties of GO are exploitable also in the fields of photovoltaic and photocatalysis.[74]
It has been seen that the work function of reduced GO lies between the ones of titanium dioxide (TiO_2) and Indium Tin Oxide. This means that, by using rGO-TiO_2 derivatives as photoanodes in Dye-Sensitized Solar Cells (DSSC), the electron-hole recombination is suppressed by facilitating the electron collection at the anode. Moreover, the high surface area of GO improves the efficiency of the dye loading than that of pure TiO_2.[75]
Polymer-based solar cells exploit the formation of electron-hole pairs at *p-n* heterojunction interface, formed by *p-type* and *n-type* polymer. In these structures, graphene derivatives have been used to support the electron-hole separation and the charge transport, also introducing continuous electron pathways between isolated domains of polymeric heterojunction.[76-78] Graphene derivatives have also been used in these solar cells as an alternative transparent electrode[79] or hole transport layer.[80]
As an electron acceptor and efficient charge carrier, rGO is useful also in photocatalysis because of the suppression of the charge recombination. Indeed, rGO-TiO_2 nanosystems have shown increased photocatalytic efficiency in the degradation of dye mimicking pollutants (as Methylene blue).[81] Furthermore, thanks to the high surface area it enhances the adsorptivity of the dye onto the photocatalytic system, and also extends the photoresponding range (compared with bare TiO_2) due to the Ti-O-C interactions which decrease the TiO_2 band gap.[82]

In this landscape, it is clearly evident that the polymer functionalization of GO represents a fundamental tool to improve and/or tune the GO properties. By changing the polymers and modifying the GO structure, the development possibilities for nanotechnological applications become potentially unlimited.

1.3 Aim of the thesis

The work exposed in this thesis aims to exploit the polymer features synergistically with that of the GO, to fulfil the needs of advanced functional materials.
Different polymers are investigated to interact, covalently or not, with the GO counterpart, by employing cheap and green approaches. Thanks to the versatility of the polymers, potential applications of the resulting GO-based nanosystems are investigated in the fields of: optical sensing of pollutants, photocatalysis, drug-delivery and anti-bacterial surfaces.
The optical and thermal properties, the size, and the structure of the developed nanosystems are characterized by means of suitable analytical techniques. A brief description of the following chapters is below reported.

-A supramolecular approach towards the synthesis of GO-based nanosystems is described in Chapter 2. A PEGylated Porphyrin derivative is used to produce a stable supramolecular adduct with GO. To shed light on the supramolecular interactions occurring, such an adduct is in-depth characterized through spectroscopic techniques. Finally, the spectroscopic properties of the adduct are investigated to develop an optical sensor for aromatic pollutants in the aqueous environment.

-PEGylation of GO is a well-known functionalization useful to improve the solubility and the biocompatibility of the graphene platform in water and is fundamental in drug delivery. Usually, esterification reactions are performed to covalently bond PEG chains over GO, involving different reactants and solvents depending on the method adopted. In Chapter 3 the development of a solvent-free method to produce PEGylated GO is described. Moreover, the effects of the PEGylation on the chemical-physical properties are investigated.

-Chapter 4 is focused on the synthesis, characterization, and photocatalytic performances of a novel covalent adduct produced by the etherification between a Porphyrin derivative and the GO platform. Through an *in-situ* polymerization, the GO-Porphyrin system was embedded within a polymer matrix. The resulting nanocomposite was used as thin film to perform photocatalytic water remediation experiments.

-An advanced feature of biomedical devices and common use objects is the antibacterial property. It is usually ensured through suitable additives or coatings. To hinder the already reported toxic and adverse effects of the common antibacterial organic agents, a nanotechnological approach towards the synthesis of a potential antibacterial nanosystem is reported in Chapter 5.

1.4 References

1 Novoselov, K. S. Electric Field Effect in Atomically Thin Carbon Films. *Science* **306**, 666-669, doi:10.1126/science.1102896 (2004).

2 Geim, A. K. & Novoselov, K. S. The rise of graphene. *Nature Materials* **6**, 183-191, doi:10.1038/nmat1849 (2007).

3 Partoens, B. & Peeters, F. M. From graphene to graphite: Electronic structure around the K point. *Physical Review B* **74**, doi:10.1103/PhysRevB.74.075404 (2006).

4 Blake, P. *et al.* Graphene-Based Liquid Crystal Device. *Nano Letters* **8**, 1704-1708, doi:10.1021/nl080649i (2008).

5 Randviir, E. P., Brownson, D. A. C. & Banks, C. E. A decade of graphene research: production, applications and outlook. *Materials Today* **17**, 426-432, doi:10.1016/j.mattod.2014.06.001 (2014).

6 Schwierz, F. Graphene transistors. *Nature Nanotechnology* **5**, 487-496, doi:10.1038/nnano.2010.89 (2010).

7 Raccichini, R., Varzi, A., Passerini, S. & Scrosati, B. The role of graphene for electrochemical energy storage. *Nature Materials* **14**, 271-279, doi:10.1038/nmat4170 (2014).

8 Tan, C. *et al.* Recent Advances in Ultrathin Two-Dimensional Nanomaterials. *Chemical Reviews* **117**, 6225-6331, doi:10.1021/acs.chemrev.6b00558 (2017).

9 Hyun, W. J., Park, O. O. & Chin, B. D. Foldable Graphene Electronic Circuits Based on Paper Substrates. *Advanced Materials* **25**, 4729-4734, doi:10.1002/adma.201302063 (2013).

10 Huang, L., Huang, Y., Liang, J., Wan, X. & Chen, Y. Graphene-based conducting inks for direct inkjet printing of flexible conductive patterns and their applications in electric circuits and chemical sensors. *Nano Research* **4**, 675-684, doi:10.1007/s12274-011-0123-z (2011).

11 Roy-Mayhew, J. D., Bozym, D. J., Punckt, C. & Aksay, I. A. Functionalized Graphene as a Catalytic Counter Electrode in Dye-Sensitized Solar Cells. *ACS Nano* **4**, 6203-6211, doi:10.1021/nn1016428 (2010).

12 Zhang, D. W. *et al.* Graphene-based counter electrode for dye-sensitized solar cells. *Carbon* **49**, 5382-5388, doi:10.1016/j.carbon.2011.08.005 (2011).

13 Lee, C., Wei, X., Kysar, J. W. & Hone, J. Measurement of the Elastic Properties and Intrinsic Strength of Monolayer Graphene. *Science* **321**, 385-388, doi:10.1126/science.1157996 (2008).

14 Balandin, A. A. *et al.* Superior Thermal Conductivity of Single-Layer Graphene. *Nano Letters* **8**, 902-907, doi:10.1021/nl0731872 (2008).

15 Yoon, D., Son, Y.-W. & Cheong, H. Negative Thermal Expansion Coefficient of Graphene Measured by Raman Spectroscopy. *Nano Letters* **11**, 3227-3231, doi:10.1021/nl201488g (2011).

16 Bunch, J. S. *et al.* Impermeable Atomic Membranes from Graphene Sheets. *Nano Letters* **8**, 2458-2462, doi:10.1021/nl801457b (2008).

17 Geim, A. K. Graphene: Status and Prospects. *Science* **324**, 1530-1534, doi:10.1126/science.1158877 (2009).

18 Chen, S. *et al.* Oxidation Resistance of Graphene-Coated Cu and Cu/Ni Alloy. *ACS Nano* **5**, 1321-1327, doi:10.1021/nn103028d (2011).

19 Prasai, D., Tuberquia, J. C., Harl, R. R., Jennings, G. K. & Bolotin, K. I. Graphene: Corrosion-Inhibiting Coating. *ACS Nano* **6**, 1102-1108, doi:10.1021/nn203507y (2012).

20 Yang, K., Feng, L., Shi, X. & Liu, Z. Nano-graphene in biomedicine: theranostic applications. *Chem. Soc. Rev.* **42**, 530-547, doi:10.1039/c2cs35342c (2013).

21 Pal, M., Mondal, M. K., Paine, T. K. & Pal, P. Purifying arsenic and fluoride-contaminated water by a novel graphene-based nanocomposite membrane of enhanced selectivity and sustained flux. *Environmental Science and Pollution Research* **25**, 16579-16589, doi:10.1007/s11356-018-1829-1 (2018).

22 Viraka Nellore, B. P. *et al.* Bio-Conjugated CNT-Bridged 3D Porous Graphene Oxide Membrane for Highly Efficient Disinfection of Pathogenic Bacteria and Removal of Toxic Metals from Water. *ACS Applied Materials & Interfaces* **7**, 19210-19218, doi:10.1021/acsami.5b05012 (2015).

23 Pastrana-Martínez, L. M., Morales-Torres, S., Figueiredo, J. L., Faria, J. L. & Silva, A. M. T. in *Multifunctional Photocatalytic Materials for Energy* 79-101 (2018).

24 Georgakilas, V. *et al.* Functionalization of Graphene: Covalent and Non-Covalent Approaches, Derivatives and Applications. *Chemical Reviews* **112**, 6156-6214, doi:10.1021/cr3000412 (2012).

25 Mittal, G., Dhand, V., Rhee, K. Y., Park, S.-J. & Lee, W. R. A review on carbon nanotubes and graphene as fillers in reinforced polymer nanocomposites. *Journal of Industrial and Engineering Chemistry* **21**, 11-25, doi:10.1016/j.jiec.2014.03.022 (2015).

26 Li, D., Müller, M. B., Gilje, S., Kaner, R. B. & Wallace, G. G. Processable aqueous dispersions of graphene nanosheets. *Nature Nanotechnology* **3**, 101-105, doi:10.1038/nnano.2007.451 (2008).

27 Boehm, H.-P. & Stumpp, E. Citation errors concerning the first report on exfoliated graphite. *Carbon* **45**, 1381-1383, doi:10.1016/j.carbon.2006.12.016 (2007).

28 Schafhaeutl, C. LXXXVI. On the combinations of carbon with silicon and iron, and other metals, forming the different species of cast iron, steel, and malleable iron. *The London, Edinburgh, and Dublin Philosophical Magazine and Journal of Science* **16**, 570-590, doi:10.1080/14786444008650094 (2009).

29 Schafhaeutl, C. Ueber die Verbindungen des Kohlenstoffes mit Silicium, Eisen und anderen Metallen, welche die verschiedenen Gattungen von Roheisen, Stahl und Schmiedeeisen bilden. *Journal für Praktische Chemie* **20**, 465-485, doi:10.1002/prac.18400200164 (1840).

30 Hummers, W. S. & Offeman, R. E. Preparation of Graphitic Oxide. *Journal of the American Chemical Society* **80**, 1339-1339, doi:10.1021/ja01539a017 (1958).

31 Compton, O. C. & Nguyen, S. T. Graphene Oxide, Highly Reduced Graphene Oxide, and Graphene: Versatile Building Blocks for Carbon-Based Materials. *Small* **6**, 711-723, doi:10.1002/smll.200901934 (2010).

32 Wissler, M. Graphite and carbon powders for electrochemical applications. *Journal of Power Sources* **156**, 142-150, doi:10.1016/j.jpowsour.2006.02.064 (2006).

33 Trömel, M. & Russ, M. Dimanganheptoxid zur selektiven Oxidation organischer Substrate. *Angewandte Chemie* **99**, 1037-1038, doi:10.1002/ange.19870991009 (1987).

34 Dreyer, D. R., Park, S., Bielawski, C. W. & Ruoff, R. S. The chemistry of graphene oxide. *Chem. Soc. Rev.* **39**, 228-240, doi:10.1039/b917103g (2010).

35 Lerf, A., He, H., Forster, M. & Klinowski, J. Structure of Graphite Oxide Revisited‖. *The Journal of Physical Chemistry B* **102**, 4477-4482, doi:10.1021/jp9731821 (1998).

36 Paredes, J. I., Villar-Rodil, S., Martínez-Alonso, A. & Tascón, J. M. D. Graphene Oxide Dispersions in Organic Solvents. *Langmuir* **24**, 10560-10564, doi:10.1021/la801744a (2008).

37 Hsiao, M.-C. *et al.* Preparation of Covalently Functionalized Graphene Using Residual Oxygen-Containing Functional Groups. *ACS Applied Materials & Interfaces* **2**, 3092-3099, doi:10.1021/am100597d (2010).

38 Neri, G. *et al.* Repurposing of oxazolone chemistry: gaining access to functionalized graphene nanosheets in a top-down approach from graphite. *Chemical Science* **6**, 6961-6970, doi:10.1039/c5sc02576a (2015).

39 Wang, S. *et al.* High Mobility, Printable, and Solution-Processed Graphene Electronics. *Nano Letters* **10**, 92-98, doi:10.1021/nl9028736 (2010).

40 Dua, V. *et al.* All-Organic Vapor Sensor Using Inkjet-Printed Reduced Graphene Oxide. *Angew Chem Int Edit* **49**, 2154-2157 (2010).

41 Sirringhaus, H. *et al.* High-resolution inkjet printing of all-polymer transistor circuits. *Science* **290**, 2123-2126 (2000).

42 Konios, D., Stylianakis, M. M., Stratakis, E. & Kymakis, E. Dispersion behaviour of graphene oxide and reduced graphene oxide. *Journal of Colloid and Interface Science* **430**, 108-112, doi:10.1016/j.jcis.2014.05.033 (2014).

43 Kamyshny, A. & Magdassi, S. Conductive Nanomaterials for Printed Electronics. *Small* **10**, 3515-3535 (2014).

44 Shin, K.-Y., Hong, J.-Y. & Jang, J. Micropatterning of Graphene Sheets by Inkjet Printing and Its Wideband Dipole-Antenna Application. *Advanced Materials* **23**, 2113-2118, doi:10.1002/adma.201100345 (2011).

45 Park, S., Vosguerichian, M. & Bao, Z. A. A review of fabrication and applications of carbon nanotube film-based flexible electronics. *Nanoscale* **5**, 1727-1752 (2013).

46 Kong, D., Le, L. T., Li, Y., Zunino, J. L. & Lee, W. Temperature-Dependent Electrical Properties of Graphene Inkjet-Printed on Flexible Materials. *Langmuir* **28**, 13467-13472, doi:10.1021/la301775d (2012).

47 Pei, S. & Cheng, H.-M. The reduction of graphene oxide. *Carbon* **50**, 3210-3228, doi:10.1016/j.carbon.2011.11.010 (2012).

48 Kuila, T. *et al.* Chemical functionalization of graphene and its applications. *Progress in Materials Science* **57**, 1061-1105, doi:10.1016/j.pmatsci.2012.03.002 (2012).

49 Guo, S. *et al.* Covalent grafting of triazine derivatives onto graphene oxide for preparation of epoxy composites with improved interfacial and mechanical properties. *Journal of Materials Science* **53**, 16318-16330, doi:10.1007/s10853-018-2788-0 (2018).

50 Xu, Z. *et al.* Organosilane-functionalized graphene oxide for enhanced antifouling and mechanical properties of polyvinylidene fluoride ultrafiltration membranes. *Journal of Membrane Science* **458**, 1-13, doi:10.1016/j.memsci.2014.01.050 (2014).

51 Robinson, J. T., Perkins, F. K., Snow, E. S., Wei, Z. & Sheehan, P. E. Reduced Graphene Oxide Molecular Sensors. *Nano Letters* **8**, 3137-3140, doi:10.1021/nl8013007 (2008).

52 Fowler, J. D. *et al.* Practical Chemical Sensors from Chemically Derived Graphene. *ACS Nano* **3**, 301-306, doi:10.1021/nn800593m (2009).

53 Konwer, S., Guha, A. K. & Dolui, S. K. Graphene oxide-filled conducting polyaniline composites as methanol-sensing materials. *Journal of Materials Science* **48**, 1729-1739, doi:10.1007/s10853-012-6931-z (2012).

54 Swathi, R. S. & Sebastian, K. L. Long range resonance energy transfer from a dye molecule to graphene has (distance)−4 dependence. *The Journal of Chemical Physics* **130**, doi:10.1063/1.3077292 (2009).

55 Liu, C. H., Wang, Z., Jia, H. X. & Li, Z. P. Efficient fluorescence resonance energy transfer between upconversion nanophosphors and graphene oxide: a highly sensitive biosensing platform. *Chemical Communications* **47**, 4661-4663, doi:10.1039/C1CC10597C (2011).

56 Lee, J. *et al.* Colorimetric Thermometer from Graphene Oxide Platform Integrated with Red, Green, and Blue Emitting, Responsive Block Copolymers. *Chem Mater* **28**, 3446-3453, doi:10.1021/acs.chemmater.6b00913 (2016).

57 Paek, K., Yang, H., Lee, J., Park, J. & Kim, B. J. Efficient Colorimetric pH Sensor Based on Responsive Polymer–Quantum Dot Integrated Graphene Oxide. *ACS Nano* **8**, 2848-2856, doi:10.1021/nn406657b (2014).

58 Yang, H., Paek, K. & Kim, B. J. Efficient Temperature Sensing Platform Based on Fluorescent Block Copolymer-Functionalized Graphene Oxide. *Nanoscale* **5**, doi:10.1039/c3nr01486j (2013).

59 Acik, M. *et al.* Unusual infrared-absorption mechanism in thermally reduced graphene oxide. *Nature Materials* **9**, 840-845, doi:10.1038/nmat2858 (2010).

60 Zhang, E. *et al.* Fast Self-Healing of Graphene Oxide-Hectorite Clay-Poly(N,N-dimethylacrylamide) Hybrid Hydrogels Realized by Near-Infrared Irradiation. *ACS Applied Materials & Interfaces* **6**, 22855-22861, doi:10.1021/am507100m (2014).

61 Kim, J. T., Kim, B. K., Kim, E. Y., Kwon, S. H. & Jeong, H. M. Synthesis and properties of near IR induced self-healable polyurethane/graphene nanocomposites. *European Polymer Journal* **49**, 3889-3896, doi:10.1016/j.eurpolymj.2013.10.009 (2013).

62 Wei, Y., Tao, L., Li, J., Hu, W. & Zhang, X. A comparative study of cellular uptake and cytotoxicity of multi-walled carbon nanotubes, graphene oxide, and nanodiamond. *Toxicology Research* **1**, 62-68, doi:10.1039/c2tx20006f (2012).

63 Wang, K. *et al.* Biocompatibility of Graphene Oxide. *Nanoscale Research Letters*, doi:10.1007/s11671-010-9751-6 (2010).

64 Liu, Z., Robinson, J. T., Sun, X. & Dai, H. PEGylated Nanographene Oxide for Delivery of Water-Insoluble Cancer Drugs. *Journal of the American Chemical Society* **130**, 10876-10877, doi:10.1021/ja803688x (2008).

65 Kim, H., Lee, D., Kim, J., Kim, T.-i. & Kim, W. J. Photothermally Triggered Cytosolic Drug DeliveryviaEndosome Disruption Using a Functionalized Reduced Graphene Oxide. *ACS Nano* **7**, 6735-6746, doi:10.1021/nn403096s (2013).

66 Weissleder, R. A clearer vision for in vivo imaging. *Nature Biotechnology* **19**, 316-317, doi:10.1038/86684 (2001).

67 Robinson, J. T. *et al.* Ultrasmall Reduced Graphene Oxide with High Near-Infrared Absorbance for Photothermal Therapy. *Journal of the American Chemical Society* **133**, 6825-6831, doi:10.1021/ja2010175 (2011).

68 Hu, S.-H. *et al.* Photoresponsive Protein-Graphene-Protein Hybrid Capsules with Dual Targeted Heat-Triggered Drug Delivery Approach for Enhanced Tumor Therapy. *Advanced Functional Materials* **24**, 4144-4155, doi:10.1002/adfm.201400080 (2014).

69 Hu, W. *et al.* Graphene-Based Antibacterial Paper. *ACS Nano* **4**, 4317-4323, doi:10.1021/nn101097v (2010).

70 Akhavan, O. & Ghaderi, E. Toxicity of Graphene and Graphene Oxide Nanowalls Against Bacteria. *ACS Nano* **4**, 5731-5736, doi:10.1021/nn101390x (2010).

71 Liu, S. *et al.* Antibacterial Activity of Graphite, Graphite Oxide, Graphene Oxide, and Reduced Graphene Oxide: Membrane and Oxidative Stress. *ACS Nano* **5**, 6971-6980, doi:10.1021/nn202451x (2011).

72 Liu, Y. *et al.* Antibacterial graphene oxide coatings on polymer substrate. *Applied Surface Science* **436**, 624-630, doi:10.1016/j.apsusc.2017.12.006 (2018).

73 Szaraniec, B., Pielichowska, K., Pac, E. & Menaszek, E. Multifunctional polymer coatings for titanium implants. *Materials Science and Engineering: C* **93**, 950-957, doi:10.1016/j.msec.2018.08.065 (2018).

74 Huang, X., Qi, X., Boey, F. & Zhang, H. Graphene-based composites. *Chem. Soc. Rev.* **41**, 666-686, doi:10.1039/c1cs15078b (2012).

75 Tang, Y.-B. *et al.* Incorporation of Graphenes in Nanostructured TiO2 Films via Molecular Grafting for Dye-Sensitized Solar Cell Application. *ACS Nano* **4**, 3482-3488, doi:10.1021/nn100449w (2010).

76 Yu, D., Yang, Y., Durstock, M., Baek, J.-B. & Dai, L. Soluble P3HT-Grafted Graphene for Efficient Bilayer–Heterojunction Photovoltaic Devices. *ACS Nano* **4**, 5633-5640, doi:10.1021/nn101671t (2010).

77 Liu, Q. *et al.* Polymer Photovoltaic Cells Based on Solution-Processable Graphene and P3HT. *Advanced Functional Materials* **19**, 894-904, doi:10.1002/adfm.200800954 (2009).

78 Liu, Z. *et al.* Organic Photovoltaic Devices Based on a Novel Acceptor Material: Graphene. *Advanced Materials* **20**, 3924-3930, doi:10.1002/adma.200800366 (2008).

79 Xu, Y. *et al.* Polymer photovoltaic devices with transparent graphene electrodes produced by spin-casting. *Carbon* **48**, 3308-3311, doi:10.1016/j.carbon.2010.05.017 (2010).

80 Li, S.-S., Tu, K.-H., Lin, C.-C., Chen, C.-W. & Chhowalla, M. Solution-Processable Graphene Oxide as an Efficient Hole Transport Layer in Polymer Solar Cells. *ACS Nano* **4**, 3169-3174, doi:10.1021/nn100551j (2010).

81 Du, J. *et al.* Hierarchically Ordered Macro−Mesoporous TiO2−Graphene Composite Films: Improved Mass Transfer, Reduced Charge Recombination, and Their Enhanced Photocatalytic Activities. *ACS Nano* **5**, 590-596, doi:10.1021/nn102767d (2010).

82 Zhang, H., Lv, X., Li, Y., Wang, Y. & Li, J. P25-Graphene Composite as a High Performance Photocatalyst. *ACS Nano* **4**, 380-386, doi:10.1021/nn901221k (2009).

2 Graphene Oxide/PEGylated Porphyrin supramolecular adduct as a potential sensor of cationic pollutants

2.1 Introduction

The spectroscopic properties of porphyrins make them excellent organic dyes to study the formation of supramolecular systems with the Graphene Oxide.[1-5] Among all the porphyrin derivatives, the water-soluble porphyrins are the most used dyes to investigate about the supramolecular aggregation, which occurs because of π-π and/or hydrophobic and/or electrostatic interactions. Indeed, to make the porphyrins water soluble, their functionalization with suitable ionic groups[6-8] (such as sulfonate, phosphonate, etc.) is usually performed. Nevertheless, as a challenging point in the study of the supramolecular aggregation phenomenon, the ionic contribution could be so strong to hide the π-π interaction contribution; moreover, the charges could hinder the binding processes in the field of sensors.

Thus, a class of PEGylated porphyrin derivatives has been developed starting from the 5,10,15,20-tetrakis-[*p*-hydroxyphenyl]-porphyrin, through the etherification of the porphyrin's hydroxyphenyl groups with Poly-ethylene glycol-mono methyl ether chains having different lengths,[9] these last already reported in the literature as biocompatible species in the biomedical field and as environmental friendly in materials science. During the design and study of the properties of this class of uncharged water-soluble porphyrin derivatives, it has been found that the molecular architectures influence not only their structural properties in water at neutral pH, from monomers to self-assembled aggregates,[10-12] but also the different aggregates morphology, namely H- or J- type and, consequently, their typical optical properties.[13] Some of these PEGylated derivatives were also used as a potential probe for inorganic sensing of pH, NO_x, and Oxygen,[14-17] but also in photodynamic therapy.[18,19]

In this chapter, a PEGylated derivative of the 5,10,15,20-tetrakis-[*p*-hydroxyphenyl]-porphyrin functionalized with three PEG chains (P3PEG) with a weight average molecular weight of 750 Da and its non-covalent adduct with Graphene Oxide (GO) are discussed. Such a porphyrin derivative, in contrast with its other analogues, shows a monomer-dimer equilibrium in water solution which depends on the concentration, and no higher-order supramolecular aggregates are formed (at low concentration). This equilibrium and the related spectroscopic properties will be investigated to perceive a better comprehension of the adduct formation and the mechanism involved.

The interactions between GO and P3PEG were studied through spectroscopy techniques, and the attention was focused on the mechanisms generating the spectroscopic quenching phenomenon observed for the P3PEG when involved in the P3PEG/GO supramolecular adduct formation.

The P3PEG/GO complex was formed through two interactions routes: one regards the interaction with the nitrogen atoms of the porphyrin core and the carboxylic acid groups of the GO, and the other by means of π-π interaction occurring between the porphyrin core and the GO platform surface. The supramolecular complex produced is stable and resistant to centrifugation and next redispersion in water. Thus, a proof of concept was conducted to test the GO-P3PEG adduct as a potential fluorescence sensor of a cationic pollutant.

The research work here exposed resulted in a paper entitled "Supramolecular Structures Formed in Water by Graphene Oxide and Nonionic PEGylated Porphyrin: Interaction Mechanisms and Fluorescence Quenching Effects", *J. Phys. Chem. C* 2019, 123, 25977−25984 (DOI:10.1021/acs.jpcc.9b06800).

2.2 Materials and Methods

All the reagents and solvents were purchased from Sigma-Aldrich.

The synthesis of the 5,10,15-[*p*-(ω-methoxy-polyethyleneoxy)-phenyl]-20-[*p*-hydroxyphenyl]-porphyrin (P3PEG) is elsewhere reported.[9,20]

Graphene oxide (GO) was purchased by "Nanesa srl" as 4.5 g/L aqueous solution. The flake sizes are in the range 1-6 µm (50% of mass below 4 µm) and <1 µm thickness.

The solutions used for spectroscopic analyses were produced by adding to GO aqueous solutions at several concentrations (from 1 to 10 mg/L) the amount of P3PEG stock solution prepared in the concentration range 0.1-10 µM by diluting a P3PEG stock solution at 250 µM. All the prepared solutions, whose measured pH was equal to 6.5, were stored 3 hours in the dark before the experiments, accounting that the ageing effect is negligible within 24 hours.

The concentration values used were chosen to obtain an extinction value (at the fluorescence excitation wavelength) well below 0.1, to avoid any *a-posteriori* spectral correction or quenching effect related to absorption phenomena along the incident path.

Particular care was taken to avoid the inner filter effect due to the GO extinction overlapping the P3PEG fluorescence emission wavelength.

2.3 PEGylated Porphyrin aqueous solution spectroscopic properties

As a common feature of this class of porphyrin derivatives, independently from the number, position, and length of the PEG chains bounded to the porphyrin core, the P3PEG in organic solvent doesn't produce any aggregation phenomenon. Its absorption spectrum is characterized by the S_0-S_2 transition

at 421 nm (the Soret band) and the S_0-S_1 electronic transition revealed by four Q-bands at 517, 553.4, 594.6 and 652.1 nm, respectively (Figure 2.1).

In aqueous solution, although the Q-band region doesn't show any shift, the Soret band extremely changes. It is constituted by two partially overlapped bands whose relative amplitude depends on the concentration, as shown in Figure 2.1.

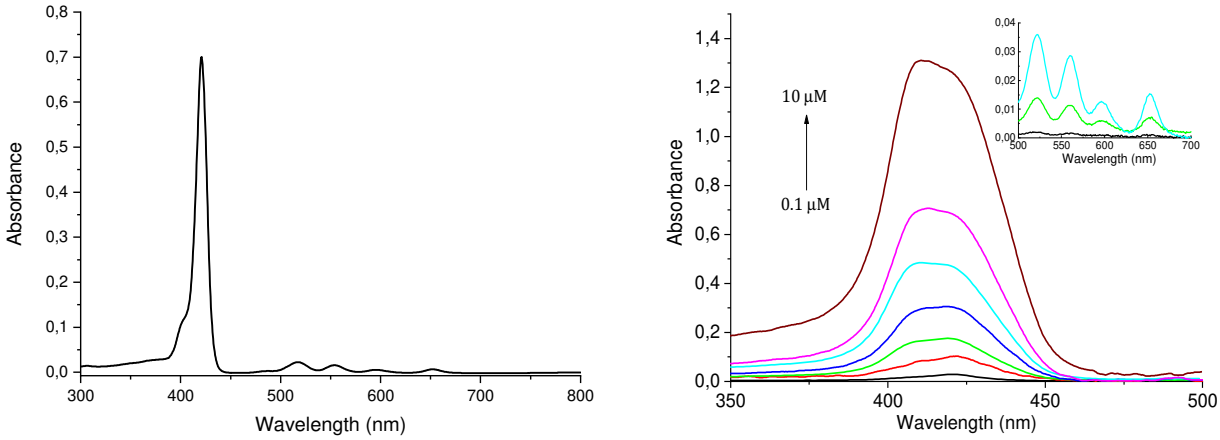

Figure 2.1 Left: UV-vis spectrum of P3PEG THF solution (1.6·µM). Right: Absorption spectra of the P3PEG aqueous solutions at different concentration values, from 0.1 up to 10 µM. Inset: Q-bands spectra region of the aqueous solution at 0.1, 1 and 3 µM.

To clarify this evidence, spectral deconvolution was conducted (Figure 2.2). It reveals the monomer contribution at 422 nm and a blue-shifted absorption band centered at 408 nm, reasonably attributable to the formation of the H-type dimer. Increasing the P3PEG concentration, the relative absorbance of the dimer increases while the monomer one decreases.

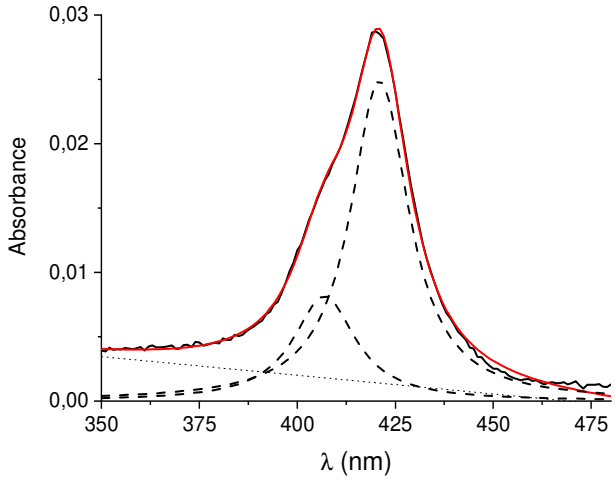

Figure 2.2 Spectral deconvolution of P3PEG aqueous solution at 0.1 µM (Soret region).

Because a linear dependence between the total Soret area and the porphyrin concentration is revealed (Figure 2.3), the extinction coefficient of the dimer is reasonably the same as the monomer. It means that the oscillator strength of the dimer is double than that of the monomer.

Nevertheless, the dependence of the Soret area from the P3PEG concentration lost the linearity above 3 μM, probably because of the formation of bigger aggregates. The dimer-monomer equilibrium is so well defined that, in the concentration range below 3 μM, it is possible to measure the concentration of each species (monomer-dimer) from the values of absorbance at their typical wavelengths. Two almost-linear regions of the monomer-dimer composition were identified, with a slope variation occurring at about 1 μM.[21]

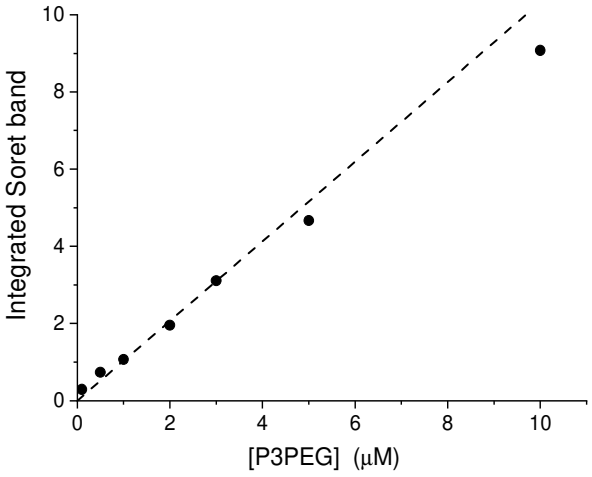

Figure 2.3 Concentration/Soret band area dependence of the P3PEG water solution.

Also, the fluorescence spectra show emission intensity which is proportional to the porphyrin concentration below 3 μM, without any appreciable wavelength shift. In Figure 2.4 the emission spectra of the P3PEG water solutions at 1 and 3 μM are reported, for the sake of clarity.

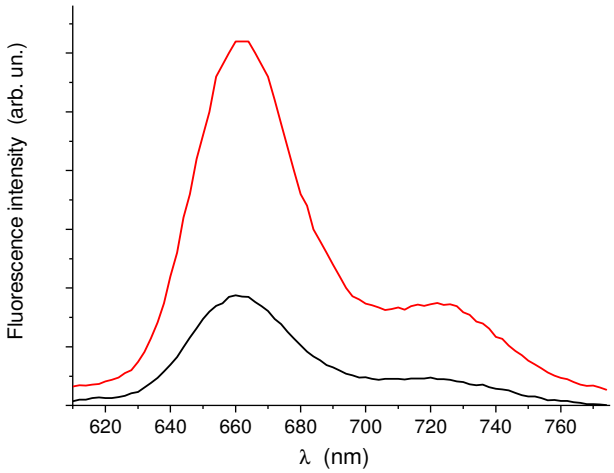

Figure 2.4 Emission spectra of P3PEG water solutions at 1 μM (black line) and 3 μM (red line), λ_{exc}=422 nm.

The time-resolved fluorescence study revealed that two different exponential decay characterize the species in solution. In particular, a longer (about 9 ns) and a shorter lifetime (<1 ns) were revealed; the energy contribution of the shorter one raises while increasing the porphyrin concentration. The longer lifetime is attributable to the monomer,[10,22] while the shorter one is reasonably due to the excited state of the dimer,[23,24] accordingly to literature data.

The study of the equilibrium monomer-dimer is fundamental to afford the successive study related to the interaction in solution of the P3PEG with another species.

2.4 GO/PEGylated Porphyrin supramolecular adduct formation study

The spectroscopic study was conducted on two different porphyrin concentrations: the aqueous solutions at 1 and 3 μM were chosen as representative of the two monomer-dimer equilibrium regions. The GO extinction signal in the wavelength range 350-800 nm is attributable to the scattering effects: indeed, it does not change during the porphyrin addition in solution. This also means that no aggregation effects are induced by the porphyrin among GO sheets. In Figure 2.5 were reported the absorption spectra of these P3PEG solutions at different GO concentrations (since the considerations about the GO extinction, its contribution was subtracted in each spectrum). The analysis of the absorption profiles reveals that, in both P3PEG solutions, appears a new Soret band red-shifted at 440 nm. Moreover, at low P3PEG concentration (1 μM), the Soret band is also more evident and red-shifted of 2 nm.

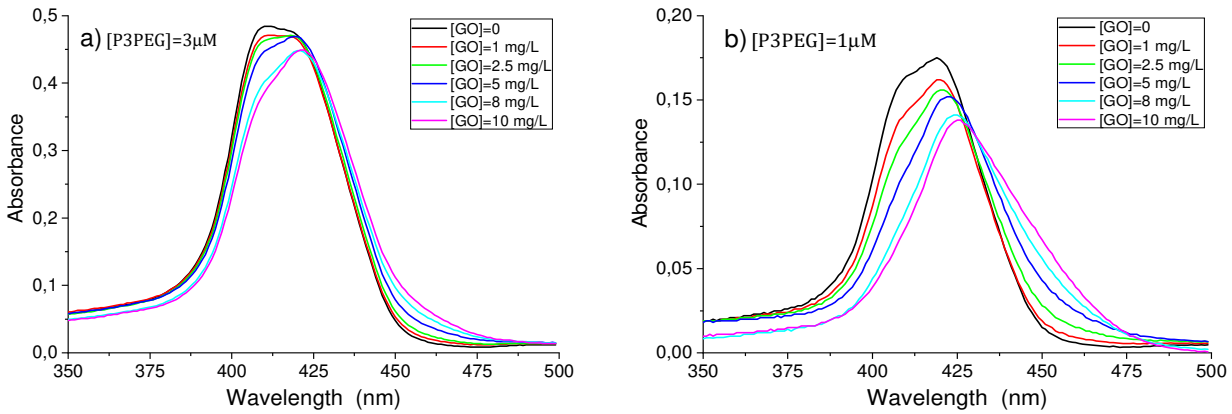

Figure 2.5 Absorption spectra of the P3PEG aqueous solution at 3 µM (a) and 1 µM (b), acquired during the GO titration.

To investigate on the obtained supramolecular system, the P3PEG aqueous solution (1 µM) with the highest amount of GO was centrifuged for 15 min at 9000 rpm, and the supernatant was removed (Figure 2.6, Top).

The extinction spectrum of the collected solid dispersed in water (Figure 2.6, Bottom, b) shows the band in the range 440-445 nm, which looks like the solution before the centrifugation (Figure 2.6, Bottom, a), but with different relative amplitude. The extinction spectrum of the supernatant reveals the presence of the free P3PEG (Figure 2.6, Bottom, c), but also of the GO.

Analysing the Q-bands region, a band at 675 nm appears in the redispersed precipitate spectrum, resembling the one of the protonated P3PEG.[14,20,25] The electronic transitions related to the Q-band region are clearer when the GO contribution is subtracted (Figure 2.7, inset).

Since the pKa of the P3PEG (~3,5)[20] is well lower than the working pH (~6,5), the protonation of the porphyrin core can be excluded. Instead, at this pH value, the GO carboxylic acids are mostly dissociated.[26] So, the appearance of the new Q-band could be due to a ground-state complex between the porphyrin macrocycle and the GO, made by the interactions of the protons from the acids and the pyrrolic nitrogens. Moreover, due to these interactions, the bulk concentration of the porphyrin decreases and influences the monomer-dimer equilibrium.[21]

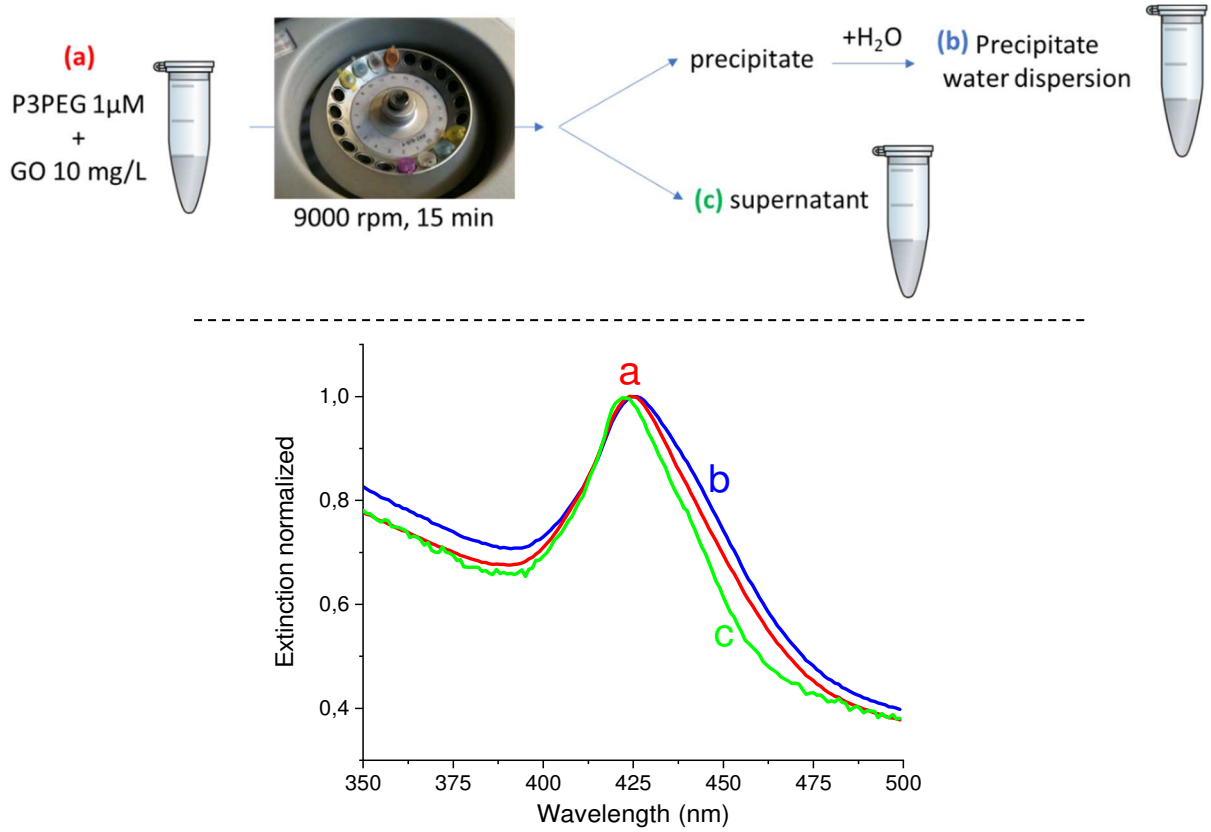

Figure 2.6 Top) Schematic illustration of the procedure to isolate the P3PEG/GO supramolecular adduct. Bottom) Normalized extinction spectra of the P3PEG/GO (1 µM and 10 mg/L, respectively) before (a) and after (b) centrifugation and redispersion, and the extinction spectra of the supernatant (c).

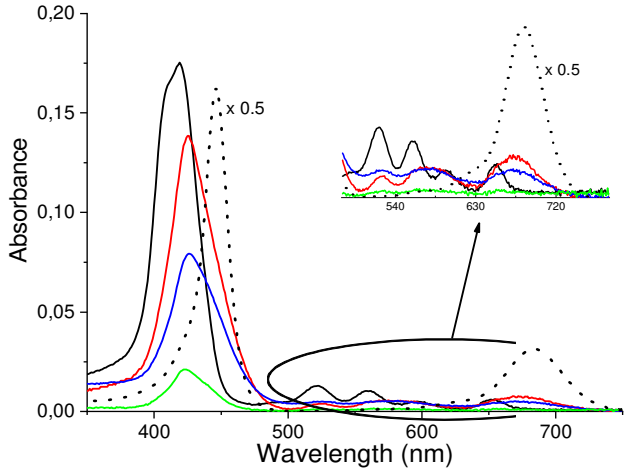

Figure 2.7 Absorption spectra of the P3PEG aqueous solution (1 µM) at the working pH (6.5) with GO added (10 mg/L) before and after centrifugation and redispersion (red and blue line, respectively), and the spectrum of the supernatant (green line), compared with those of P3PEG 1 µM at the working pH without GO (black continuous line) and under acidic conditions (black dotted line).

In order to verify this kind of interactions, spectroscopic studies adding a competitor to the redispersed precipitate solution were conducted. TEA was chosen as proton scavenger. As a result, the contribution to the Soret (440-445 nm) and the Q-band (675 nm) decreases (Figure 2.8), but does not disappear, suggesting other mechanisms involved in the interaction between P3PEG and GO.

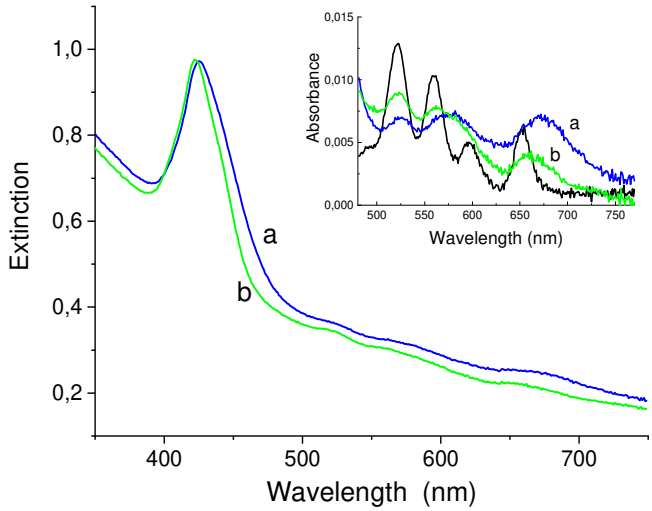

Figure 2.8 Comparison of the normalized extinction profiles of P3PEG/GO redispersed precipitate before (a) and after (b) TEA addition (1 μM). Inset: comparison of the Q-band regions (extinction contribution of the GO subtracted) with P3PEG alone at the same concentration (black line).

Fluorescence spectroscopy studies revealed that the quenching of fluorescence in P3PEG/GO solutions increases as a function of GO concentration, without any change in the emission wavelength. This event was also verified by changing the excitation wavelength: initially 500 nm, close to the Q-band, then 450 nm, closer to the complex's Soret band.

This evidence is in accordance with the formation of a ground-state complex between a dye and an electron-rich moiety, which was further investigated by determining the Stern-Volmer constant related to the fluorescence quenching. Steady-state fluorescence studies evidenced that the inverse of P3PEG fluorescence intensity is proportional to the GO concentration, obeying to the Stern-Volmer equation:[27]

$$F_0/F=1+K_{SV}[GO]$$

where F_0 is the emission intensity of P3PEG in the absence of GO, F is the emission intensity of P3PEG at different GO concentration, [GO], and K_{SV} the Stern-Volmer constant.

It has been verified that the measured K_{SV} scales with the P3PEG concentration (Figure 2.9, left), being about 0.22 L/mg for [P3PEG]=1 μM and about 0.08 L/mg [P3PEG]=3 μM.

This evidence is in accordance with the formation of stable P3PEG/GO adducts, whose concentration is not negligible with respect to the GO one.

Since the constant scales with P3PEG concentration, the non-linear form of the Stern-Volmer equation should be used:[28,29] the obtained data confirmed the results found out from the previous calculation (data not shown for brevity).

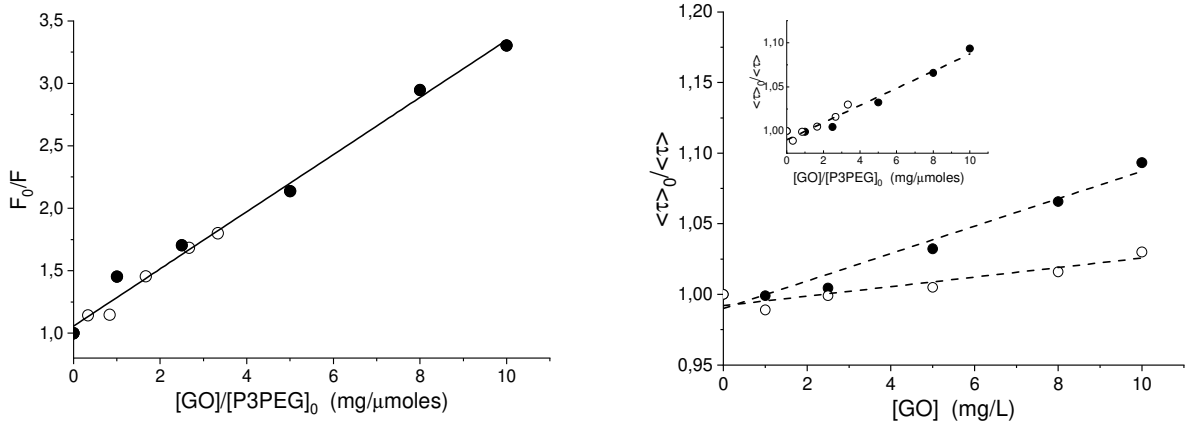

Figure 2.9 Left: Stern-Volmer plot scaled for P3PEG initial concentration ([P3PEG]$_0$=1 μM, filled circle; [P3PEG]$_0$=3 μM, hollow circles) for the steady-state fluorescence emission (λ_{ex}=500 nm, λ_{em}=660 nm). Right: Stern-Volmer plot for the average fluorescence lifetime (λ_{ex}=500 nm, λ_{em}=660 nm) for two P3PEG initial concentration values: 1 μM (filled circles) and 3 μM (hollow circles). The same plot scaled for P3PEG initial concentration is reported in the inset.

Table 2.1 Fit parameters of the fluorescence decay curves (λ_{ex}=500 nm, λ_{em}=660 nm).

	[P3PEG]=1 μM						
[GO] (mg/L)	**A_1 (%)**	**E_1 (%)**	**$\tau_1 \pm 0.2$ (ns)**	**A_2 (%)**	**E_2 (%)**	**$\tau_2 \pm 0.1$ (ns)**	**<τ> (ns)**
0	5	0.5	0.8	95	99.5	9.1	9.1
1	4	0.5	1	96	99.5	9.1	9.1
2.5	17	0.9	0.4	83	99.1	9.1	9.0
5	18	1.5	0.6	82	98.5	8.9	8.8
8	30	2.4	0.5	70	97.6	8.7	8.5
10	44	3.6	0.4	56	96.4	8.5	8.2
	[P3PEG]=3 μM						
0	20	1	0.4	80	99	9.1	9.0
1	10	0.7	0.6	90	99.3	9.2	9.1
2.5	10	0.7	0.6	90	99.3	9.1	9.0
5	18	1	0.4	82	99	9.1	9.0
8	32	2	0.4	68	98	9.0	8.8
10	25	2	0.6	75	98	8.9	8.7

As a confirmation of such hypothesis, fluorescence lifetimes were analysed. The fluorescence decay curves are constituted of two exponential contributions as the P3PEG alone in water, but the increase of the GO concentration induces a progressive increase of the amplitude of the shorter component and shortening of the longer lifetime (as reported in Table 2.1). Since both these effects contribute to the steady-state fluorescence quenching, the average lifetime was considered for the related Stern-Volmer plot (Figure 2.9, right). Also, the time-resolved fluorescence indicates a dependence of the quenching constant on the porphyrin initial concentration (Figure 2.9, right, inset). Nevertheless, the values of the constants obtained by the Stern-Volmer equation for lifetimes, about 9.7×10^{-3} L/mg and 3.4×10^{-3} L/mg, are significantly smaller than those obtained from the steady-state fluorescent experiment.

2.5 A fluorescent "turn-on" sensor for cationic pollutants

In the last century, intensive agriculture has introduced within the environment several pollutants whose dangerousness is due to their good water solubility that induces the spreading over wide areas. In particular, herbicides have become common pollutants of agricultural, drinking, and ground-waters: one of them, the 1,1'-dimethyl-4,4'-bipyridinium dichloride also known as Paraquat (PQ, Figure 2.10), is an extremely toxic water-soluble cationic molecule. The sensing of these pollutants is fundamental to pursue environmental monitoring and prevent pollution.

The cheapest and easier-to-apply sensors are the fluorescence-based ones, because of the cheap instruments needed and the high sensitivity of this spectroscopic technique. In this context, the detaching phenomenon of the P3PEG from the P3PEG/GO adduct could be exploited to sense pollutants through the induced turn-on fluorescent signal.

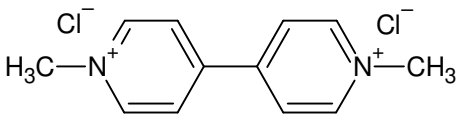

Figure 2.10 Molecular scheme of 1,1'-dimethyl-4,4'-bipyridinium dichloride, also known as Paraquat.

The PQ molecular structure exhibits charges and aromatic structures which could be exploited for the supramolecular binding with the GO platform. The ability of the adduct P3PEG/GO to sense the presence of PQ was investigated through the addition of increasing amounts of PQ (from 0.5 up to 8 μM) to the P3PEG/GO re-dispersed precipitate solution. The fluorescence studies (shown in Figure 2.11, a) reveal that increasing the PQ concentration, the fluorescence is gradually restored. Also, the

extinction spectra show a progressive decrease of the adduct peaks intensity while increasing the PQ concentration (Figure 2.11, b).

This evidence is attributable to the PQ capability to detach the porphyrin from the GO: even though PQ is well-known to quench the fluorescence of dyes and also porphyrins,[30] it prefers to compete with the porphyrin to bind with GO, thus restoring the free bulk P3PEG concentration.

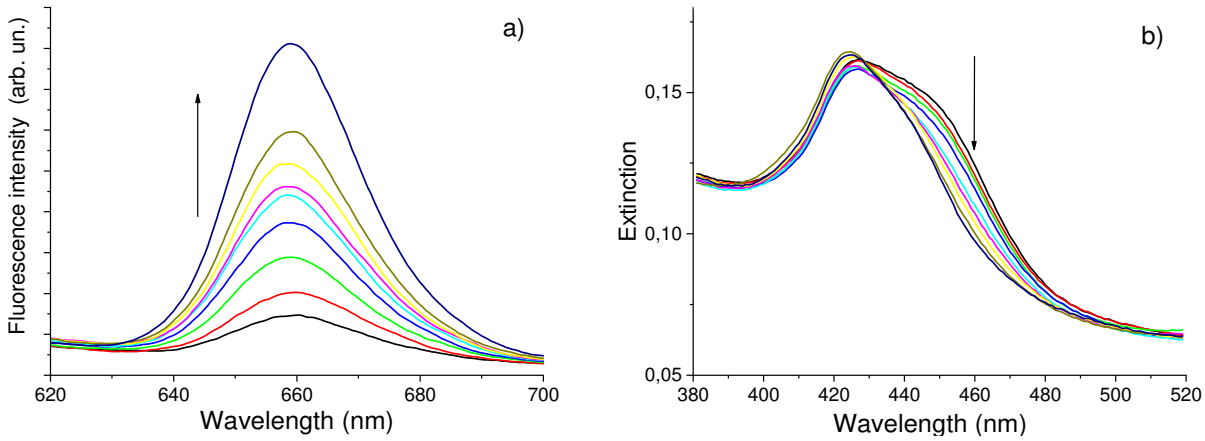

Figure 2.11 Fluorescence and extinction spectra of the P3PEG/GO re-dispersed precipitate (a and b, respectively) with increasing amounts of PQ, from 0 (black line) up to 8 μM (blue navy line).

2.6 Discussion

The formation of a stable supramolecular adduct between P3PEG and GO occurs spontaneously in aqueous solutions; moreover, the adduct has revealed strong enough to hold out to centrifugation and redispersion. About the monomer-dimer P3PEG equilibrium and its relation with the GO, it is unlikely that the dimer interacts with GO, because of the π-π stacking between the porphyrins (H arrangements) and the high steric hindrance of the PEG chains of the two porphyrins moieties involved. Instead, it could be possible that the interaction of the monomer P3PEG with GO decreases the free P3PEG concentration, and it alters the monomer-dimer equilibrium in favor of the monomer, as evidenced at the corresponding bulk P3PEG concentration without GO.

The evidence suggests that the P3PEG forms a static complex with GO, by means of two mechanisms that give rise to a ground-state complex. The first involves the interaction between the carboxylic acid groups at the edges of the GO sheets and the pyrrolic porphyrin cores, while the second one is related to P3PEG/GO platform π-π stacking complex formation. Fluorescence studies revealed that this supramolecular interaction between the dye and the GO quenches the porphyrin fluorescence emission. Because of the dependence of the constant on the initial P3PEG concentration, the non-linear Stern-Volmer equation must be applied to study this quenching phenomenon. This last

occurrence suggests that the fluorescence quenching by collisional interaction depends on the available remaining sites after the adduct formation. This means that the higher the P3PEG concentration (at fixed GO amount), the smaller the number of sites available for collisional quenching: so, the quenching by collision is diffusion controlled. By the way, this type of quenching can be neglected with respect to the overall quenching mechanisms related to this supramolecular adduct.

Since the GO could act as an electron donor-acceptor system, the fluorescence quenching could be induced from a Photo-induced Electron Transfer process (or PET) occurring in the adduct. It means that the adduct is no more emissive because of a fast deactivation of the singlet excited state. Time-resolved fluorescence study also evidenced an increase of the excited-state short lifetime contribution to the fluorescence time decay while the GO was added to the P3PEG solutions, which could be ascribed to a non-radiative charge recombination.[31,32]

Since the strong interaction occurring between P3PEG and GO in the supramolecular adduct, only the addition of TEA perturbates its equilibrium. But, when PQ was added, the strong interaction with the negatively charged acid groups (together with the π-π stacking and charge transfer) forces out the P3PEG, which is released in bulk and its fluorescence restored. The results exposed pave the way for potential uses of the P3PEG/GO supramolecular adduct as a "turn-on" fluorescence sensor of pollutants in water.

2.7 Conclusions

By means of two mechanism, the P3PEG interacts spontaneously with GO in aqueous solution, forming a ground-state supramolecular complex. The first mechanism involved is the proton counter ion-mediated, occurring between the carboxylic acid groups of GO and the pyrrolic nitrogen atoms of the porphyrin core; the second mechanism is related to the π-π stacking interaction between the macrocyclic porphyrin core and the GO sheet. These interactions lead, overall, to a static quenching of the P3PEG fluorescence, but also to a small influence of dynamic quenching due to the free GO sites after the adduct formation.

At the working pH conditions, the bulky porphyrins are not in the protonated form, but the carboxylic acid of GO could be dissociated. This means that the local acidity (nearby the acid GO groups) could be high enough (pH = 3.8) to induce the P3PEG protonation.

This electrostatic interaction between the two moieties is not negligible and is the base to let the supramolecular adduct acts as a "turn-on" sensor. The capability to sense a cationic aromatic water-soluble pollutant as the PQ, a common herbicide, was tested by adding the PQ to an aqueous solution

of the supramolecular adduct. The interaction of the PQ with the GO chemical groups is stronger than that of the P3PEG, so the P3PEG is forced out from the adduct and its fluorescence emission restored. This evidence paves the way to applications of GO-P3PEG supramolecular complex as potential sensor for pollutants in water and in heterogeneous gas phases.

Since time-resolved fluorescence experiments evidenced a PET process occurring in the supramolecular adduct, there could be also the possibility of applications in energy conversion devices.

2.8 References

1 Ge, R. *et al.* The influence of combination mode on the structure and properties of porphyrin–graphene oxide composites. *Colloids and Surfaces A: Physicochemical and Engineering Aspects* **483**, 45-52, doi:10.1016/j.colsurfa.2015.05.056 (2015).

2 Larowska, D. *et al.* Cationic Porphyrin-Graphene Oxide Hybrid: Donor-Acceptor Composite for Efficient Photoinduced Electron Transfer. *ChemPhysChem* **20**, 1054-1066, doi:10.1002/cphc.201900040 (2019).

3 Zhu, K. *et al.* The study of a novel cobalt-implanted pyridylporphyrin/graphene oxide nanohybrid for enhanced photocatalytic hydrogen evolution and its electron transfer mechanism. *Nanoscale* **10**, 18635-18641, doi:10.1039/c8nr06138f (2018).

4 Wang, Y. *et al.* A Photoinduced Electron Transfer System by Graphene Oxide Non-covalently Linked Porphyrin Antennae in Water. *Electrochemistry* **83**, 950-955, doi:10.5796/electrochemistry.83.950 (2015).

5 Monteiro, A. R. *et al.* Hybrids Based on Graphene Oxide and Porphyrin as Tools for Detection and Stabilization of DNA G-Quadruplexes. *ACS Omega* **3**, 11184-11191, doi:10.1021/acsomega.8b01366 (2018).

6 Ribó, J. M., Crusats, J., Farrera, J.-A. & Valero, M. L. Aggregation in water solutions of tetrasodium diprotonated meso-tetrakis(4-sulfonatophenyl)porphyrin. *J. Chem. Soc., Chem. Commun.*, 681-682, doi:10.1039/c39940000681 (1994).

7 Aggarwal, L. P. F. & Borissevitch, I. E. On the dynamics of the TPPS4 aggregation in aqueous solutions. *Spectrochimica Acta Part A: Molecular and Biomolecular Spectroscopy* **63**, 227-233, doi:10.1016/j.saa.2005.05.009 (2006).

8 Lauceri, R. *et al.* Hierarchical self-assembly of water-soluble porphyrins. *Synthetic Metals* **147**, 49-55, doi:10.1016/j.synthmet.2004.05.031 (2004).

9 Mineo, P., Scamporrino, E. & Vitalini, D. Synthesis and Characterization of Uncharged Water-Soluble Star Polymers Containing a Porphyrin Core. *Macromolecular Rapid Communications* **23**, 681-687, doi:10.1002/1521-3927(20020801)23:12<681::Aid-marc681>3.0.Co;2-i (2002).

10 Angelini, N. *et al.* Interactions between water soluble porphyrin-based star polymer and amino acids: Spectroscopic evidence of molecular binding. *Phys Rev E* **71**, doi:10.1103/PhysRevE.71.021915 (2005).

11 Micali, N. *et al.* Aggregation phenomena in aqueous solutions of uncharged star polymers with a porphyrin core. *J Phys Chem B* **107**, 5095-5100, doi:10.1021/jp026999p (2003).

12 Villari, V., Mineo, P., Scamporrino, E. & Micali, N. Spontaneous self-assembly of water-soluble porphyrins having poly(ethylene glycol) as branches: Dependence of aggregate properties from the building block architecture. *Chem Phys* **409**, 23-31, doi:10.1016/j.chemphys.2012.09.022 (2012).

13 Villari, V., Mineo, P., Scamporrino, E. & Micali, N. Role of the hydrogen-bond in porphyrin J-aggregates. *Rsc Adv* **2**, 12989-12998, doi:10.1039/c2ra22260d (2012).

14 Mineo, P. G., Vento, F., Abbadessa, A., Scamporrino, E. & Nicosia, A. An optical sensor of acidity in fuels based on a porphyrin derivative. *Dyes Pigments* **161**, 147-154, doi:10.1016/j.dyepig.2018.09.045 (2019).

15 Gulino, A., Mineo, P., Scamporrino, E., Vitalini, D. & Fragala, I. Molecularly engineered silica surfaces with an assembled porphyrin monolayer as optical NO2 molecular recognizers. *Chem Mater* **16**, 1838-1840, doi:10.1021/cm049902f (2004).

16 Gulino, A. *et al.* Photoluminescence of a covalent assembled porphyrin-based monolayer: Optical behavior in the presence of O-2. *J Phys Chem B* **110**, 16781-16786, doi:10.1021/jp062967g (2006).

17 Mineo, P. G. *et al.* PEGylate porphyrin-gold nanoparticles conjugates as removable pH-sensor nano-probes for acidic environments. *Colloid Surface A* **546**, 40-47, doi:10.1016/j.colsurfa.2018.02.061 (2018).

18 Mineo, P., Faggio, C., Micali, N., Scamporrino, E. & Villari, V. A star polymer based on a polyethylene glycol with a porphyrinic core as a photosensitizing agent for application in photodynamic therapy: tests in vitro on human erythrocytes. *Rsc Adv* **4**, doi:10.1039/c3ra47913g (2014).

19 Mineo, P. *et al.* Gold nanoparticles functionalized with PEGylate uncharged porphyrins. *Dyes Pigments* **141**, 225-234, doi:10.1016/j.dyepig.2017.02.018 (2017).

20 Mineo, P. G. *et al.* PEGylate porphyrin-gold nanoparticles conjugates as removable pH-sensor nano-probes for acidic environments. *Colloids and Surfaces A: Physicochemical and Engineering Aspects* **546**, 40-47, doi:10.1016/j.colsurfa.2018.02.061 (2018).

21 Micali, N., Mineo, P., Vento, F., Nicosia, A. & Villari, V. Supramolecular Structures Formed in Water by Graphene Oxide and Nonionic PEGylated Porphyrin: Interaction Mechanisms and Fluorescence Quenching Effects. *The Journal of Physical Chemistry C* **123**, 25977-25984, doi:10.1021/acs.jpcc.9b06800 (2019).

22 Villari, V., Mineo, P., Scamporrino, E. & Micali, N. Role of the hydrogen-bond in porphyrin J-aggregates. *RSC Advances* **2**, doi:10.1039/c2ra22260d (2012).

23 Maiti, N. C., Ravikanth, M., Mazumdar, S. & Periasamy, N. Fluorescence Dynamics of Noncovalently Linked Porphyrin Dimers, and Aggregates. *The Journal of Physical Chemistry* **99**, 17192-17197, doi:10.1021/j100047a024 (1995).

24 García-Ortega, H., Bourdelande, J. L., Crusats, J., El-Hachemi, Z. & Ribó, J. M. Excited Triplet States in Aggregates and Monomers of Water Soluble Meso-Aryl Substituted Porphyrins. *The Journal of Physical Chemistry B* **108**, 4631-4639, doi:10.1021/jp037587z (2004).

25 Dattilo, S., Mineo, P., Scamporrino, E., Spina, E. & Vitalini, D. Synthesis and characterization of new copolyacrylates containing porphyrin units as pendant groups and their use as sensors. *Journal of Polymer Science Part A: Polymer Chemistry* **49**, 796-802, doi:10.1002/pola.24494 (2011).

26 Konkena, B. & Vasudevan, S. Understanding Aqueous Dispersibility of Graphene Oxide and Reduced Graphene Oxide through pKa Measurements. *The Journal of Physical Chemistry Letters* **3**, 867-872, doi:10.1021/jz300236w (2012).

27 Lakowicz, J. R. *Principles of Fluorescence Spectroscopy*. (2006).

28 Campbell, K., Zappas, A., Bunz, U., Thio, Y. S. & Bucknall, D. G. Fluorescence quenching of a poly(para-phenylene ethynylenes) by C60 fullerenes. *Journal of Photochemistry and Photobiology A: Chemistry* **249**, 41-46, doi:10.1016/j.jphotochem.2012.08.015 (2012).

29 Ciotta, E., Prosposito, P. & Pizzoferrato, R. Positive curvature in Stern-Volmer plot described by a generalized model for static quenching. *Journal of Luminescence* **206**, 518-522, doi:10.1016/j.jlumin.2018.10.106 (2019).

30 Thordarson, P. *et al.* Highly Negative Homotropic Allosteric Binding of Viologens in a Double-Cavity Porphyrin. *Journal of the American Chemical Society* **125**, 1186-1187, doi:10.1021/ja028463n (2003).

31 Arcudi, F. *et al.* Porphyrin Antennas on Carbon Nanodots: Excited State Energy and Electron Transduction. *Angew Chem Int Edit* **56**, 12097-12101, doi:10.1002/anie.201704544 (2017).

32 Yu, P. *et al.* Efficient electron transfer in carbon nanodot–graphene oxide nanocomposites. *Journal of Materials Chemistry C* **2**, doi:10.1039/c3tc32395a (2014).

3 A solvent-free PEGylation of Graphene Oxide and its effects on the supramolecular interactions

3.1 Introduction

Graphene Oxide covalent functionalization could be approached by several methods that have pros and cons, as it is already well reported in literature.[1-6] The dual necessity to produce advanced functional materials and to go beyond environmental issues, have pushed scientists to find greener reaction pathways, compared to the common strategies, yet ensuring the same product quality.

In this field, the development of GO polymer derivative without solvents or toxic reagents is a not yet reached milestone. Different pathways are already studied,[7,8] but all of them involve either expensive techniques or the functionalization of the moieties before the covalent bonding between them.

The poly-(ethylene glycol) (PEG) is a biocompatible poly-ether characterized by very-low toxicity and lacks immunogenicity,[9] high solubility in water and other common solvents.[10]

The applications of PEG is well known in pharmacology,[11] where it has been used not only for the solvent compatibilization of water-insoluble drugs,[12] but also to improve their biocompatibility and half-life.[13]

Such effects have been fundamental for the application of Graphene Oxide (GO) in the biomedical field.[14-17] Indeed, the biocompatibility of GO systems directly injected and/or implanted is still a controversial point. In particular, due to the several production methods adopted, the GO materials exhibit intrinsic differences in terms of oxidation degree, size, thickness, residues, and physicochemical properties, influencing the way they interact with the biological matter.[18,19]

The GO covalent functionalization with a polymer having stealth properties represents a way to improve the biocompatibility of the GO platform.[20] Nevertheless, the functionalization reactions could leave undesired residues that increase not only the GO toxicity, also alter its physicochemical properties.[19] For these reasons, such an inconvenience may be an issue not only in the biomedical field but also in electronics.[21]

With the aim to avoid any unwanted residue related to the solvents adopted to covalently functionalize GO with polymers, a solvent-free GO functionalization reaction was developed, exploiting the PEG ability to solubilize GO powder and using a microwave-assisted procedure to obtain PEGylated GO derivatives. The GO in powder form was homogeneously mixed with PEGME chains, and the microwaves in nitrogen atmosphere were used to catalyze a condensation reaction involving the carboxylic acids of the GO and the alcohol of the PEGME. The obtained GO-polymer derivative was

characterized utilizing FT-IR spectroscopy, Thermogravimetric analysis, Differential Scanning Calorimetry, and Dynamic Light Scattering. The functionalization degree of the GO platform was calculated employing two different methods. As a comparison with the un-modified GO shown in the previous section, the formation of a supramolecular adduct between the PEGylated GO and the P3PEG was investigated. Moreover, supramolecular properties of the resulting complex were further investigated by the addition of a P3PEG stacking competitor, the 1,1'-dimethyl-4,4'-bipyridinium dichloride (also known as Paraquat, PQ).

3.2 Materials and methods

All the reagents and solvents used in this synthesis were purchased by Sigma-Aldrich.
The Graphene Oxide (GO) was purchased by Nanesa s.r.l (Arezzo, Italy) in water solution 4,5 g/L; in order to obtain a GO in form of dry powder, the stock solution was dried through a rotary evaporator and vacuum oven.

Synthesis of the polyethylene glycol monomethyl ether-esterified-Graphene Oxide (PEGME5k@GO): 1.014 g of Polyethylene glycol monomethyl ether (average molecular mass 5 kDa, PEGME5k) and 53 mg of dried GO were left at 50 °C in a vacuum oven, overnight. In order to improve the homogeneity, the materials were mixed and sonicated at 70°C for 1 hour. Then, the mixture was poured into a 10 mL vessel and this last was placed into a Microwave reactor. The system was set to apply a microwave-induced thermal ramp (60°C/min) up to 150°C, and then the sample irradiation was performed to maintain a constant temperature (150°C). Anhydrous nitrogen was fluxed into the reaction mixture to ensure a dry environment.
After four hours, the mixture was dissolved in THF (50 mL) and filtered on a Buchner funnel, in order to purge out the unreacted GO.
The filtered solution was then centrifuged (5000 rpm, 10 minutes, 5°C), and the precipitate was collected and washed twice with 20 mL of THF. The obtained powder was then dried in vacuum oven overnight (50°C).
Synthesis of the Polyethylene glycol monomethyl ether-esterified-Graphene Oxide (PEGME750@GO): 1.014 g of Polyethylene glycol monomethyl ether (average molecular mass 750 Da, PEGME750) and 51.2 mg of dried GO were used. The procedure that has been used is the same as the one of PEGME5k@GO.

Blended mixtures were prepared by weighting suitable amounts of PEGME and GO, to obtain different weight ratios between the moieties. In particular, the weight ratios PEGME/GO of 95/5, 80/20, 50/50, 20/80 to produce a total amount of 50 mg of the mixture were chosen. Then, the weighted samples were put together into a vial, and left in a heated sonicating bath at 70°C for one hour. The same procedure has been followed for both PEGME5k and PEGME750.

3.3 Structural and chemical-physical characterizations

In order to monitor the success of the esterification reaction, IR analyses were conducted.

The FT-IR spectrum of GO (Figure 3.1, black line) shows signals at 3400 cm^{-1} (O-H stretching), 1729 cm^{-1} (C=O stretching), 1621 cm^{-1} (C=C stretching), 1380 cm^{-1} (O-H stretching), 1226 cm^{-1} (C-O-C asymmetric stretching) and 1055 cm^{-1}(C-O-C symmetric stretching).[22]

The PEGME750 exhibits the typical signals (Figure 3.1, red line) at 3400 cm^{-1} (O-H stretching), 2890 cm^{-1} (C-H stretching), 1737 cm^{-1} (C=O stretching), 1641 cm^{-1} (C-H scissoring), 1460 cm^{-1} (CH_2 scissoring), 1350 cm^{-1} (CH_2 wagging), 1299 cm^{-1} (CH_2 twisting), 1249 cm^{-1} (CH_2 twisting), 1106 cm^{-1} (C-O stretching), 950 cm^{-1} (CH_2 rocking), 847 cm^{-1} (C-O and C-C stretching, CH_2 rocking). The unexpected signal at 1737 cm^{-1}, attributed to the C=O stretching, comes from aldehydes, which might be present as a degradation product of the PEGME.[23] Nevertheless, these products were eliminated from the PEGylated GO during the purification procedures.

The polymer derivative PEGME750@GO (Figure 3.1, blue line) shows the signal attributed to the carbonyl stretching at 1745 cm^{-1}, which is shifted to higher wavenumber with respect to the GO. Such evidence is attributable to the ester group formation, occurring between the acid group of the GO and the PEGME alcohol group.[24]

As expected, the IR spectrum of the PEGME5k@GO traces the pure polymer one, hiding the GO content probably due to the higher chain length. This spectrum will not be shown for brevity.

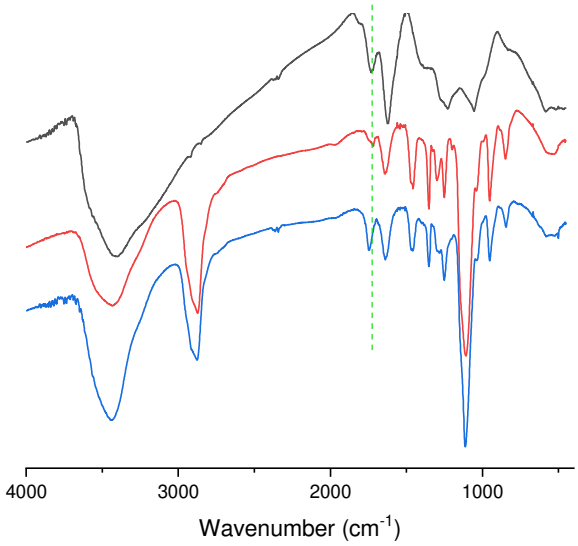

Figure 3.1 FT-IR analyses of GO (black line), PEGME750 (red line), and PEGME750@GO (blue line).

The FT-IR results evidenced the covalent functionalization of the GO platform through ester bonds with the PEG chains, which is further supported by the washing procedures operated on the product obtained from the microwave catalyzed reaction. Indeed, the un-bonded PEG chains must be eliminated by means of the THF washing thanks to their high solubility.

The esterification of GO with PEGME chains also influences the thermal stability of the carbon platform. To compare the stability of the covalent derivative PEGME750@GO with respect to the blends of GO and PEGME750 at different weight ratios, thermal analyses in nitrogen atmosphere were conducted.

The GO trace (Figure 3.2, red dotted line) exhibits two main weight losses: the first above 150°C,[25] while the second above 500°C.

A deeper description of the TGA trace of GO is exposed in Chapter 5.1.

The PEGME750 (Figure 3.2, black dotted line) shows only one weight loss at ~ 350°C, due to the formation of degradation products such as ethyl and methyl alcohol, alkenes, non-cyclic ethers, formaldehyde, acetic aldehyde, ethylene oxide, water, carbon mono- and di-oxide.[23]

Focusing on the TGA traces of the blends, it is noticeable that increasing the PEGME content from 0% up to 95%, the TGA traces gradually change from a GO-like decomposition behaviour composed of a single degradation step above 150°C (20% and 50% PEGME, Figure 3.2 green and blue line, respectively), to a three-stage decomposition (80% PEG, Figure 3.2 red line) which ends below 440°C. Lastly, the 95% PEG blend (black line), exhibits a single step decomposition as the pure PEGME750, which is compatible with the low GO percentage. The results suggest that blending GO within a PEGME matrix improves the thermal stability of the GO platform, as a consequence of the

hydrogen-bonding interactions between GO functional groups and PEG chains, coupled with intra- and inter-chains interactions.[24,26]

The covalent product PEGME750@GO (magenta continuous line) results more thermally stable than all the blends, with a first degradation step at 140 °C (6% loss), a second one at 235 °C (85% loss) and a residue at 800 °C equal to 1%. Reasonably, the first and third steps are attributable to GO, while the one at about 340 °C is attributable to the PEG moiety.

Since the difference between the thermal behaviour of the PEGME750@GO compared to the blends, this result is reasonably attributable to a covalent functionalization of the GO platform.

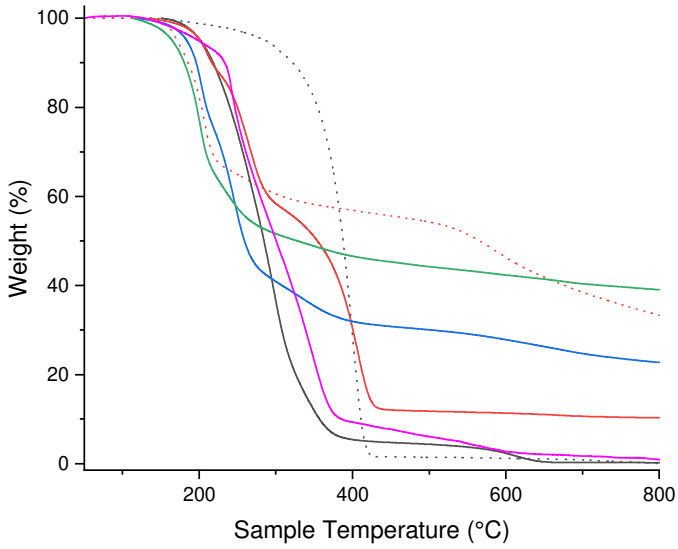

Figure 3.2 TGA traces of GO (red dotted line), PEGME750 (black dotted line), PEGME750@GO (magenta continuous line). The TGA traces of the blends PEGME750-GO (continuous line) are named as PEG weight percentage: 95% (black), 80% (red), 50% (blue), 20% (green).

To determine the degree of functionalization of the GO platform in terms of weight percentage, two methods were approached.

The first is based on the calibration curve calculated on the residue (%) of the blend thermal analysis at 500°C. In Figure 3.3 the plot of the residue (%) measured in the thermal analyses of the blends at different weight percentages of PEGME750 is reported. From the linear fit of the data the Equation (1) is obtained:

$$y = - 0.53x + 54.93 \quad (1)$$

where y is the Residue % of the sample and x is the PEGME % content.

From the (1), considering the residue of the product PEGME750@GO at 500°C (6.24 %), the weight ratio of functionalization was calculated at 92 % in terms of PEGME750.

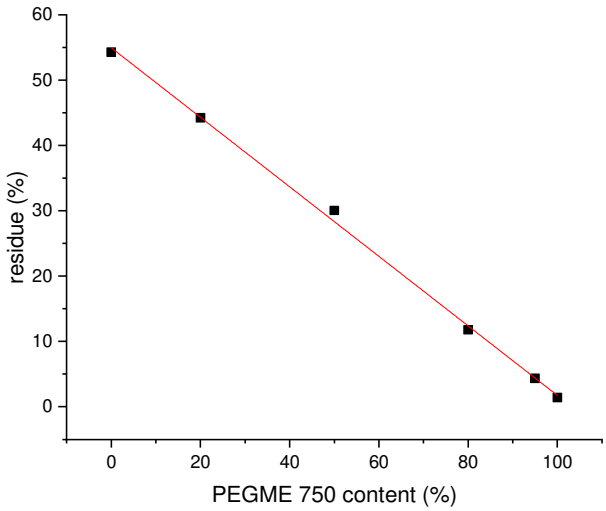

Figure 3.3 Plot of the residue (%) of the blends PEGME750-GO at 500°C in function of the nominal content of PEG in the mixture.

The second approach was taken by Xu et al. It arises from the analyses of the weight losses of the pure GO and polymer, and uses a set of two equations to define the PEG content.[27]
If the weight losses at 500°C are considered, the GO exhibits a value of 46%, the PEGME750 of 98%, and the PEGME750@GO of 94%. The equation set is composed by Equation (2) and (3):

$0.46x + 0.98y = 0.94$ (2)

$x+y = 1$ (3)

where: y = PEG weight percentage, x = GO weight percentage.

Solving the equations (2) and (3), the PEG weight percentage in PEGME750@GO results 92%. This result was confirmed by further proof of concept. Indeed, as a confirmation of the usefulness of the Xu et al. equations, these last were used to determine the PEG content of the blend which must be theoretically similar to the nominal content.
The results (shown in Table 3.1) obtained by the equations confirmed the weighted content of PEGME into the blends.

Table 3.1 PEG content of the blends PEGME750-GO calculated by means of Xu et al. equations.

Nominal PEG content (%)	Weight loss (%)	Calculated PEG %
95	95.7	95
80	88.2	80
50	70.0	46
20	55.8	18

The covalent functionalization of the PEG chains also influences the melting temperature of the polymer. The DSC thermograms, reported in Figure 3.4, show that the blend (dotted black line) have a similar melting temperature of the pure PEGME750 (continuous black line). In particular, the blend PEGME750-GO melts at 30.8 °C (ΔH=28.7 J/g) and the PEGME750 at 28.4°C (ΔH=125.2 J/g). The melting temperature of the covalent product, instead, is 25°C (ΔH=80.4 J/g), and the event is broader than the one of the blend (Figure 3.4, red line). This result could be due to the higher disorder of the PEG chains after their bond on the GO, which reduces the crystallinity of the polymeric moieties.

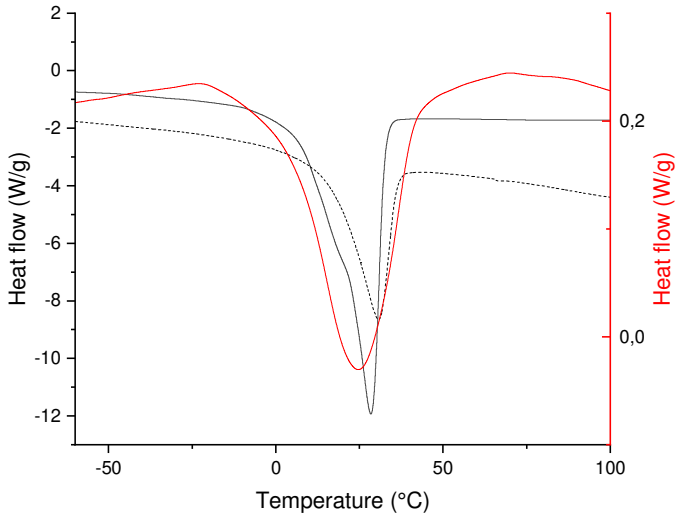

Figure 3.4 DSC traces of PEGME750 (black continuous line), blend PEGME750-GO at 50%PEGME (black dotted line), and PEGME750@GO (red continuous line).

To investigate the chain length effect related to the thermal stability of the GO polymer derivative, also the PEGME5k@GO was characterized through TGA.

The PEGME5k resulted more stable than the PEGME750, showing a single degradation step at 370 °C. In order to measure the degree of functionalization of the GO derivative, the methods already used before were applied also to this analysis. The degree of PEGME functionalization resulted 86%

with the linear fit method, and 84 % with the equation 2 and 3. The lower degree of functionalization compared to the PEGME750@GO is attributable to the higher length of the PEGME5k: a lower concentration of reactive terminal groups, coupled with the steric hindrance of PEG chains, reduce the statistical probability of the GO and PEGME reactive sites to get together.

The covalent derivative PEGME5k@GO exhibits higher thermal stability compared to the PEGME750@GO (Figure 3.5), showing a first degradation step at 304 °C (9% weight loss) and a second one at 368°C (82% weight loss, residue at 800 °C = 5.2%). Despite the lower degree of functionalization of the PEGME5k@GO than the PEGME750@GO, its thermal behaviour is more similar to the pure polymer. This evidence could be due to the longer polymer chains, which makes the thermal behaviour more similar to the PEGME than to the GO.

As a confirmation of the covalent functionalization, the PEGME5k@GO (Figure 3.5, purple continuous line) exhibits higher thermal stability than that of all the blends between PEGME5k and GO. As mentioned above in the case of the blends PEGME750-GO, the blends between PEGME5k and GO show a thermal degradation which is more similar to the polymer by increasing the amount of polymer from 0 to 95 % (Figure 3.5).

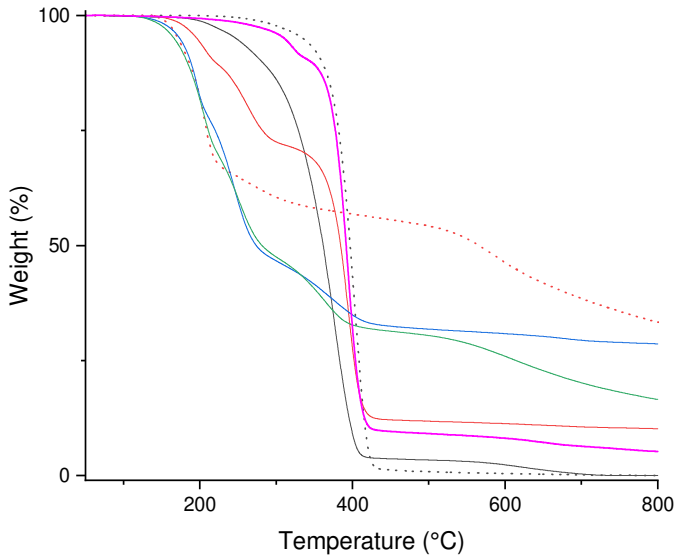

Figure 3.5 TGA traces of GO (red dotted line), PEGME5k (black dotted line), PEGME5k @GO (magenta continuous line). The TGA traces of the blends PEGME5k-GO (continuous line) are named as PEG weight percentage: 95% (black), 80% (red), 50% (blue), 20% (green).

The chain length effect is also evidenced in the DSC analyses, as reported in Figure 3.6. The pure polymer PEGME5k (Figure 3.6, black line), shows two merged melting events at 61.4 and 63.2 °C, with a small shoulder at 55.7 °C (ΔH=183.3 J/g). The blend at 50% PEGME5k exhibits a single melting event at 61.1°C (ΔH=40.5 J/g, Figure 3.6, red line). The covalent product PEGME5k@GO

(Figure 3.6, blue line) shows the melting at 61.6 °C (ΔH=139.1 J/g), which is sharper than the blend DSC trace, resembling the melting event of the pure polymer purged from the higher temperature melting. The sharpening of the melting peak probably results from the crystallinity increase due to the partial losses of the random coil conformation of the PEG chains, consequent to the covalent functionalization.

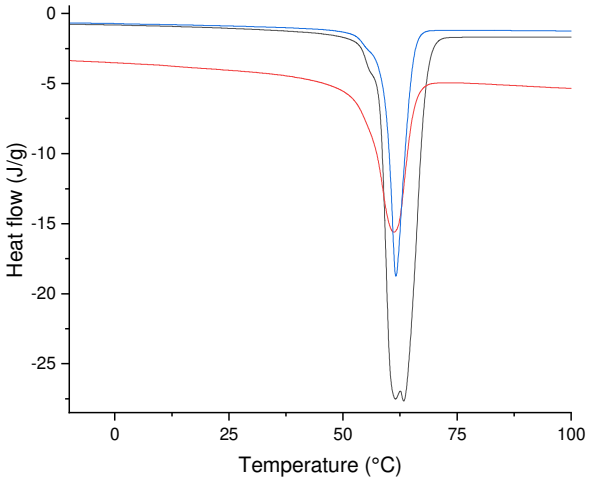

Figure 3.6 DSC trace of the pure PEGME5k (black line), the blend containing 50% (w) of PEGME5k (red line), and the PEGME5k@GO (blue line).

The different chain length between PEGME5k and PEGME750 will influence the water solubility of the nanosystems. As is well known, the aqueous GO solutions are composed by aggregates of platforms in solution, due to the stacking of the layers. One of the reasons for the polymer functionalization is also to improve the inter-layer distance, enhancing the amount of single or few layers dispersed in solution.

The GO in powder form has evidenced difficulty to be re-dispersed in water, due to the aggregation phenomena. In this case, the importance of the hydrophilic polymer functionalization increases.

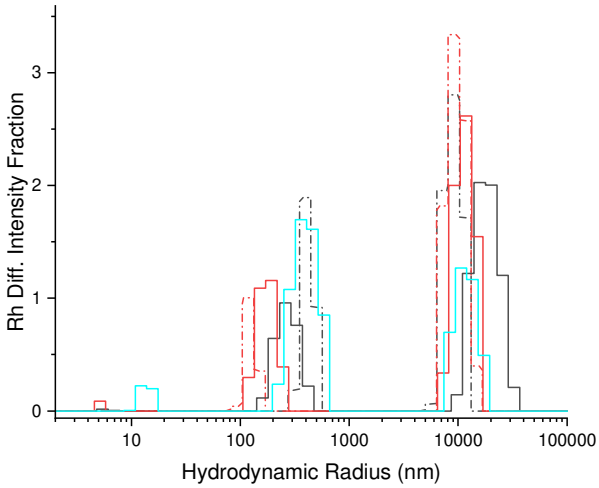

Figure 3.7 DLS analysis of PEGME750 (dash-dotted black line), PEGME5k (dash-dotted red line), PEGME5k@GO (red line),PEGME750@GO (black line), and GO (cyan line) water solution (4 mg/L).

The influences of the polymer chains on the nanosystem solubility have been investigated through DLS analysis. The GO size distribution evidenced three species, with hydrodynamic radius at 14, 400 and 12000 nm (Figure 3.7 cyan line).

The comparison between DLS data (4 mg/L in water solution) of PEGME5K and PEGME750 (Figure 3.7 red and black dash-dotted line), focusing on the region between 100 and 1000 nm hydrodynamic radius, shown that PEGME5k exhibits a lower hydrodynamic radius (119 nm) compared to PEGME750 (400 nm). This effect could be explained by the peculiar amphiphilic nature of the PEG chains, which induces inter-chains interactions: the smaller PEG shows inter-chains entanglements, which are avoided for the bigger chains.[28]

The aggregation-repulsion of the PEG chains is also function of the temperature and the concentration in solution,[28-30] but these two variables are unvaried in our experiments.

As expected, the nanocomposites essentially retrace the size distribution of their polymeric functionalities. Taking into account the mean hydrodynamic radii of the two nanosystems, it has been revealed that the PEGME750@GO has a mean hydrodynamic radius of about 1200 nm, while the PEGME5k@GO of about 600 nm. These data suggest that the longer the polymer chain, the smaller the structures in aqueous solution, probably because of the higher solubility and less inter-chains interactions.

3.4 Study of the supramolecular interactions with PEGylated Porphyrin

The polymer functionalization which involves the carboxylic acid groups of the GO sheets, influences the nanosystem supramolecular properties.

The influence of the GO carboxylic acid groups on its supramolecular properties has been discussed in Chapter 2, where a supramolecular adduct composed by GO and a PEGylated porphyrin derivative was investigated as a turn off sensor for water pollutants.

To investigate on the supramolecular binding properties of the PEG@GO systems, a titration with the 5,10,15-[*p*-(ω-methoxy-polyethyleneoxy)-phenyl]-20-[*p*-hydroxyphenyl]-porphyrin (P3PEG) was conducted. It is noteworthy to say that the working pH of 6.2 was verified for all the solutions used in these experiments.

To a P3PEG aqueous solution 1 μM suitable aliquots of a PEGME750@GO aqueous solution (2.8 mg/mL) were added to obtain a final PEGME750@GO concentration in the range 1-100 mg/L. The dilution effect towards the spectroscopic analysis could be neglected. The raw UV-vis spectra acquired are reported in Figure 3.8. The increase of the PEGME750@GO concentration in solution induces the increase of the scattering and the decrease of absorption intensities of the P3PEG Soret and Q-bands. Such a scattering increase has not been evidenced in PEGME750@GO aqueous solution (100 mg/L), thus confirming that, in contrast with the previously reported supramolecular adduct (Chapter 2), here the porphyrin presence induces the aggregation of the carbon moieties (data not shown for brevity).

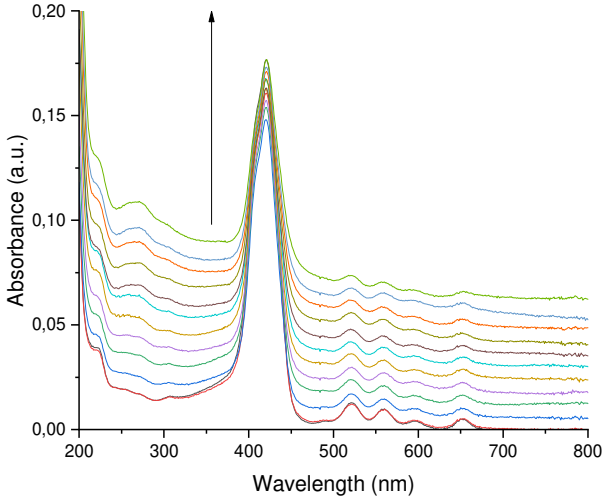

Figure 3.8 UV-vis spectra of P3PEG 1 μM upon the addition of PEGME750@GO solution, from 1 mg/L to 100 mg/L.

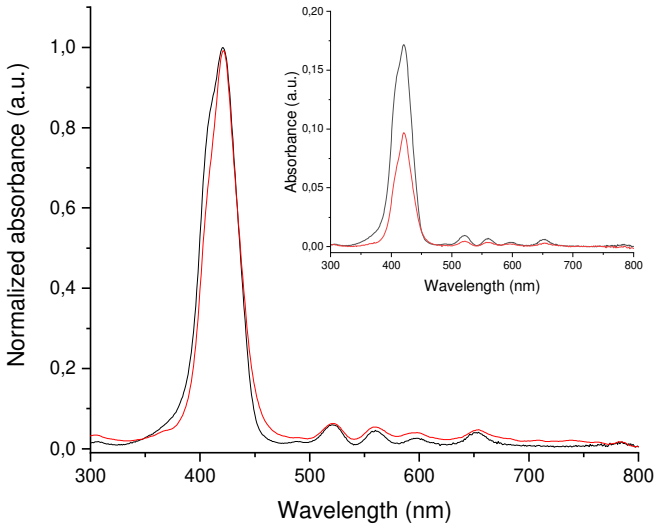

Figure 3.9 Comparison between normalized and subtracted UV-vis absorption spectra of P3PEG (1 μM) aqueous solution (black line) and P3PEG (1 μM) in presence of PEGME750@GO 100 mg/L (red line). Inset: the same UV-vis spectra just subtracted from the scattering contribution.

To better define the spectroscopic changes in P3PEG interactions with PEGME750@GO, the spectra were also compared after subtracting the extinction profile of GO at different concentrations.

The UV-vis spectra of the P3PEG solution (1 μM) before and after the addition of PEGME750@GO 100 mg/L were subtracted from the GO scattering contribution to highlight the optical absorption quenching of the P3PEG signal (inset in Figure 3.9). The comparison evidenced a decrease in the absorption intensity of about 56% compared to the starting P3PEG solution (black line). The normalization of those spectra (Figure 3.9) clearly shows the absence of any changes in the Q-bands region of the P3PEG (black line) after addition of the PEGME750@GO (red line), but it is noteworthy to say that the Soret region shows the decrease of the H-dimer contribution (408 nm).[31]

The solution at 100 mg/L was centrifuged at 9000 rpm (20 minutes), and the supernatant and the precipitate were collected. The precipitate was then resuspended in 1 mL of water. The related UV-vis spectra are shown in Figure 3.10, clearly evidencing that P3PEG is free in the supernatant solution (Soret band at 421 nm, black line), while the precipitate resuspended shows the band at 440-445 nm attributed to the supramolecular complex with PEGME750@GO (red line).

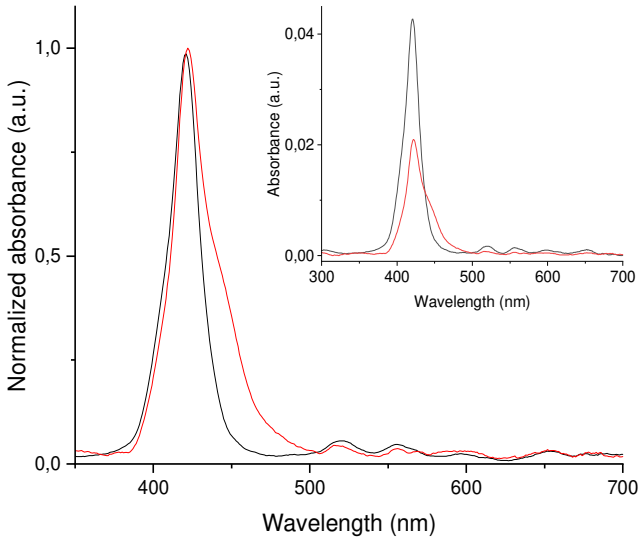

Figure 3.10 Comparison between normalized and subtracted (inset) UV-vis absorption spectra of supernatant solution (black line) and re-suspended PEGME750@GO-P3PEG precipitate (red line).

As previously studied, such contribution to the Soret could be related not only to the π-π interactions between the P3PEG and the GO platform but also to the interactions between the porphyrin core and the acid groups of the GO moiety.[31] Nevertheless, the esterification of the carboxylic groups makes them unable to donate protons in this case. As a consequence, the Q-bands region doesn't show the appearance of any signal attributable to the protonated porphyrin core (which would be centered at 675 nm). Thus, the appearance of the spectroscopic signal at 440-445 nm is only attributable to the supramolecular complex produced by the residual free acid groups of the GO with the porphyrin core. The spectroscopic behaviour during the titration was also investigated by means of monitoring the fluorescence emission at λ_{exc}=500 nm. The spectra (Figure 3.11) show the decrease of the P3PEG emission at 655 nm upon the addition of the GO derivative, as a consequence of the FRET mechanisms occurring.

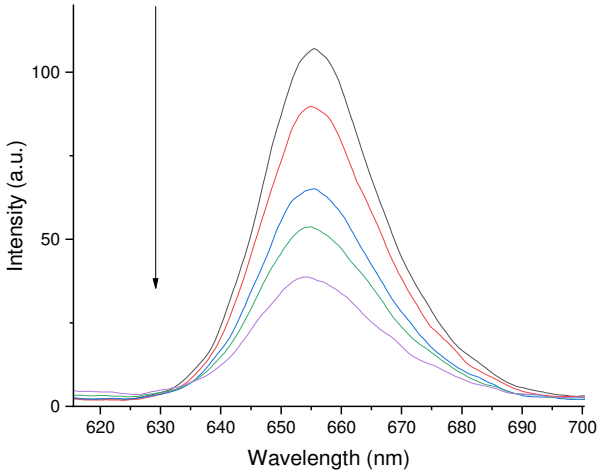

Figure 3.11 Fluorescence spectra of P3PEG 1 µM upon the addition of PEGME750@GO solution, from 1 mg/L to 100 mg/L.

To verify the strength of the π-π stacking between PEGME750@GO and P3PEG, a titration with Paraquat (PQ) was conducted. The aim was to induce the detachment of the P3PEG from the GO surface by using a better π-π stacker, as the PQ. Aliquots of a PQ water solution 517 µM were added to the resuspended precipitate solution.

During the titration, the P3PEG UV-vis extinction signal showed intensity decrease and a red shift upon the addition of PQ. Such evidence is highlighted by subtracting the scattering contribution to the UV-vis spectra (Figure 5.14 left and inset, respectively). It could be hypothesized that the P3PEG porphyrin core interacts with the PQ by means of π-π and polar interactions.

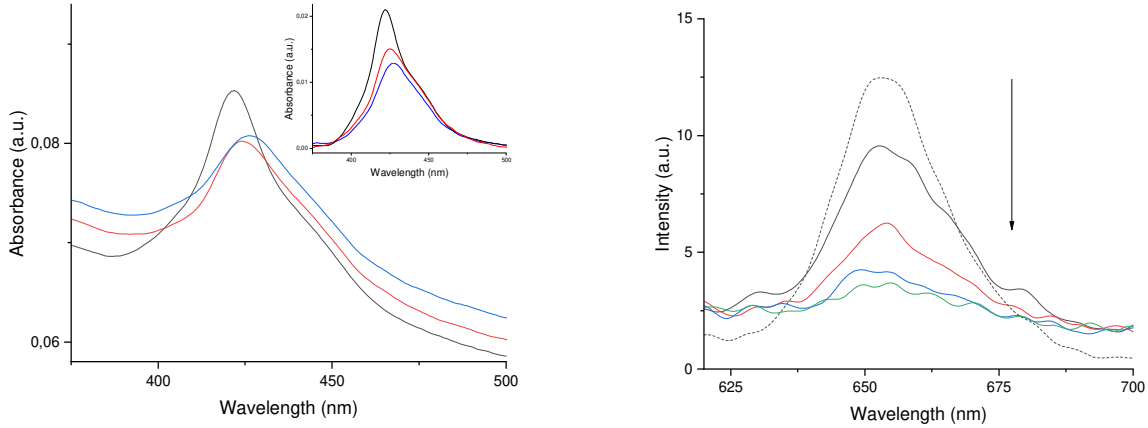

Figure 3.12 Left: UV-vis titration of the PEGME750@GO-P3PEG supramolecular complex upon addition of Paraquat to a final concentration of 2 µM (red line) and 10 µM (blue line). Inset: normalized UV-vis spectra after subtraction of the scattering contribution. Right: Fluorescence spectra related to the titration of the supramolecular complex PEGME750@GO-P3PEG upon the addition of PQ solution, from 0 µM to 3 µM.

Taking into account the fluorescence titration data, the emission related to the P3PEG moiety of the PEGME750@GO-P3PEG shows a further quenching during the addition of PQ (Figure 3.12, Right), with a complete quenching that happened already at 3 µM PQ concentration in solution. Evaluating the spectroscopic data, it is suggested that the PQ interacts with the porphyrin moiety of the PEGME750@GO-P3PEG complex, without the occurrence of P3PEG detachment.

Thus, we hypothesized that the PQ could stack on top of the P3PEG. To verify such hypothesis and investigate on the bare interaction between P3PEG and GO in water solution, a titration was conducted. In order to reproduce the same PQ/P3PEG concentration ratio of the last titration related to the precipitate resuspended, here the titration was conducted by adding aliquots of a Paraquat water solution 517 µM to a P3PEG solution (1 µM), reaching final PQ concentration from 0.5 µM up to 100 µM.

The UV-vis spectra (reported in Figure 3.13) revealed that just a small quenching effect is produced by the addition of Paraquat to the P3PEG solution, without the formation of any extinction band at 440-445 nm. Moreover, the fluorescence quenching during the titration of P3PEG 1 µM water solution with Paraquat (inset of Figure 3.13) is negligible.

This data confirms the hypothesis of the π-π stacking of the Paraquat upon the supramolecular complex, favoured from the Graphene platform presence: indeed, the proximity to Graphene platform could explain the FRET mechanisms that produce the chromophores' fluorescence emission quenching.

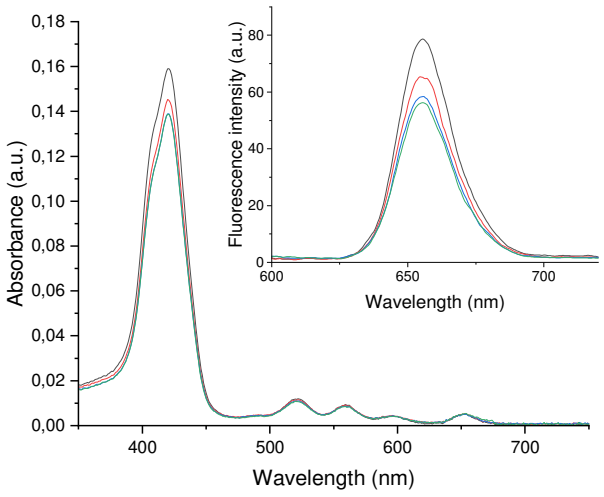

Figure 3.13 UV-vis spectra of the titration of P3PEG 1 µM water solution upon the addition of PQ, from 0 up to 100 µM. Inset: the related fluorescence emission spectra (λ_{exc} 500 nm).

3.5 Conclusions

A solvent-free method for the PEGylation of GO has been developed. The reaction was performed utilizing two PEGME having different chain lengths, corresponding to weight averaged molecular masses of 5 KDa and 750 Da, respectively. Both of the resulting nanosystems, namely PEGME5k@GO and PEGME750@GO have shown improved thermal stability compared to pristine GO. The PEGME degree of functionalization, calculated by TGA data, evidenced a high degree of functionalization of the GO platform.

The influences of the GO PEGylation on the supramolecular binding properties were evaluated through titration with P3PEG. The results evidenced that a stable supramolecular adduct has been formed only exploiting π-π interactions.[31] As a fundamental difference between the supramolecular complex GO-P3PEG shown in Chapter 2, here the GO platform could be approximated as without free carboxylic acid unit able to interact with the P3PEG core by acid/base interactions, due to the esterification occurred with the polymer chains. Nevertheless, residual acid groups could exist and produce a red-shifted Soret band at 440-445 nm.

In a first approximation, the main P3PEG/-GO interactions could unequivocally be based on π-π interactions and charge transfer.

The stability of the PEGME750@GO-P3PEG complex was investigated by the addition of a molecular system, the Paraquat, as a stacking competitor with P3PEG. The PEGME750@GO-P3PEG supramolecular complex has shown quenching of both absorbance and fluorescence emission upon the addition of PQ.

In Chapter 2 was shown that competition between P3PEG and PQ for the supramolecular binding with GO was occurring, proved by the increase of the P3PEG fluorescence and the decrease of its 440-445 nm UV absorption band with the PQ addition.

Instead, this case shows opposite spectroscopic results with the PQ addition. Could be proposed that, since the absence of any available acid-base interactions with GO, the competition between P3PEG and PQ is avoided, so an additional π-π stacking of the PQ moiety onto the P3PEG occurs. It is noteworthy to highlight that the quenching of the P3PEG spectroscopic features is negligible during the interaction of only P3PEG and PQ in water.

Despite these results evidenced the tendency of the PEGME750@GO system to supramolecular bind chromophores without selectivity and/or competition, the ability to stack different “layers” of molecules makes it a potential system to operate as an advanced drug loading system.

Moreover, the ability to bind multiple molecules by stacking layer over layer, makes this system useful also for water de-pollution. These applications must be further tested.

In our knowledge, it is the first report about a solvent-free PEGylation of GO.

3.6 References

1 Georgakilas, V. *et al.* Functionalization of Graphene: Covalent and Non-Covalent Approaches, Derivatives and Applications. *Chemical Reviews* **112**, 6156-6214, doi:10.1021/cr3000412 (2012).

2 Liu, Z., Robinson, J. T., Sun, X. & Dai, H. PEGylated Nanographene Oxide for Delivery of Water-Insoluble Cancer Drugs. *Journal of the American Chemical Society* **130**, 10876-10877, doi:10.1021/ja803688x (2008).

3 Shan, C. *et al.* Water-Soluble Graphene Covalently Functionalized by Biocompatible Poly-l-lysine. *Langmuir* **25**, 12030-12033, doi:10.1021/la903265p (2009).

4 Park, S., Dikin, D. A., Nguyen, S. T. & Ruoff, R. S. Graphene Oxide Sheets Chemically Cross-Linked by Polyallylamine. *The Journal of Physical Chemistry C* **113**, 15801-15804, doi:10.1021/jp907613s (2009).

5 Salavagione, H. J., Gómez, M. n. A. & Martínez, G. Polymeric Modification of Graphene through Esterification of Graphite Oxide and Poly(vinyl alcohol). *Macromolecules* **42**, 6331-6334, doi:10.1021/ma900845w (2009).

6 Lin, Y., Jin, J. & Song, M. Preparation and characterisation of covalent polymer functionalized graphene oxide. *J. Mater. Chem.* **21**, 3455-3461, doi:10.1039/c0jm01859g (2011).

7 Alam, A., Wan, C. & McNally, T. Surface amination of carbon nanoparticles for modification of epoxy resins: plasma-treatment vs. wet-chemistry approach. *European Polymer Journal* **87**, 422-448, doi:10.1016/j.eurpolymj.2016.10.004 (2017).

8 Alzate-Carvajal, N. *et al.* Solvent-free one-step covalent functionalization of graphene oxide and nanodiamond with amines. *Rsc Adv* **6**, 113596-113610, doi:10.1039/c6ra22658b (2016).

9 Prentice, D. E. & Majeed, S. K. Oral toxicity of polyethylene glycol (PEG 200) in monkeys and rats. *Toxicology Letters* **2**, 119-122, doi:10.1016/0378-4274(78)90084-x (1978).

10 Groll, J. & Moeller, M. in *Single Molecule Tools: Fluorescence Based Approaches, Part A Methods in Enzymology* 1-18 (2010).

11 Harris, J. M. & Chess, R. B. Effect of pegylation on pharmaceuticals. *Nature Reviews Drug Discovery* **2**, 214-221, doi:10.1038/nrd1033 (2003).

12 Greenwald, R. B., Pendri, A. & Bolikal, D. Highly Water Soluble Taxol Derivatives: 7-Polyethylene Glycol Carbamates and Carbonates. *The Journal of Organic Chemistry* **60**, 331-336, doi:10.1021/jo00107a010 (1995).

13 Zheng, L. *et al.* A pharmacokinetic and pharmacodynamic comparison of a novel pegylated recombinant consensus interferon-α variant with peginterferon-α-2a in healthy subjects. *British Journal of Clinical Pharmacology* **79**, 650-659, doi:10.1111/bcp.12528 (2015).

14 Wen, H. *et al.* Engineered Redox-Responsive PEG Detachment Mechanism in PEGylated Nano-Graphene Oxide for Intracellular Drug Delivery. *Small* **8**, 760-769, doi:10.1002/smll.201101613 (2012).

15 Thapa, R. K. *et al.* Graphene oxide-wrapped PEGylated liquid crystalline nanoparticles for effective chemo-photothermal therapy of metastatic prostate cancer cells. *Colloids and Surfaces B: Biointerfaces* **143**, 271-277, doi:10.1016/j.colsurfb.2016.03.045 (2016).

16 Ou, L. *et al.* Toxicity of graphene-family nanoparticles: a general review of the origins and mechanisms. *Particle and Fibre Toxicology* **13**, doi:10.1186/s12989-016-0168-y (2016).

17 Xu, C. *et al.* Long circulating reduced graphene oxide–iron oxide nanoparticles for efficient tumor targeting and multimodality imaging. *Nanoscale* **8**, 12683-12692, doi:10.1039/c5nr09193d (2016).

18 Dreyer, D. R., Todd, A. D. & Bielawski, C. W. Harnessing the chemistry of graphene oxide. *Chemical Society Reviews* **43**, doi:10.1039/c4cs00060a (2014).

19 Rodrigues, A. F. *et al.* A blueprint for the synthesis and characterisation of thin graphene oxide with controlled lateral dimensions for biomedicine. *2D Materials* **5**, doi:10.1088/2053-1583/aac05c (2018).

20 Demirel, E., Karaca, E. & Yuksel Durmaz, Y. Effective PEGylation method to improve biocompatibility of graphene derivatives. *European Polymer Journal* **124**, doi:10.1016/j.eurpolymj.2020.109504 (2020).

21 McManus, D. *et al.* Water-based and biocompatible 2D crystal inks for all-inkjet-printed heterostructures. *Nature Nanotechnology* **12**, 343-350, doi:10.1038/nnano.2016.281 (2017).

22 Mermoux, M., Chabre, Y. & Rousseau, A. Ftir and C-13 Nmr-Study of Graphite Oxide. *Carbon* **29**, 469-474, doi:Doi 10.1016/0008-6223(91)90216-6 (1991).

23 Pielichowski, K. & Flejtuch, K. Non-oxidative thermal degradation of poly(ethylene oxide): kinetic and thermoanalytical study. *Journal of Analytical and Applied Pyrolysis* **73**, 131-138, doi:10.1016/j.jaap.2005.01.003 (2005).

24 Zhang, S., Xiong, P., Yang, X. & Wang, X. Novel PEG functionalized graphene nanosheets: enhancement of dispersibility and thermal stability. *Nanoscale* **3**, doi:10.1039/c0nr00923g (2011).

25 Stankovich, S. *et al.* Synthesis of graphene-based nanosheets via chemical reduction of exfoliated graphite oxide. *Carbon* **45**, 1558-1565, doi:10.1016/j.carbon.2007.02.034 (2007).

26 Wang, C. *et al.* Graphene oxide stabilized polyethylene glycol for heat storage. *Physical Chemistry Chemical Physics* **14**, doi:10.1039/c2cp41988b (2012).

27 Xu, Z. *et al.* Covalent Functionalization of Graphene Oxide with Biocompatible Poly(ethylene glycol) for Delivery of Paclitaxel. *ACS Applied Materials & Interfaces* **6**, 17268-17276, doi:10.1021/am505308f (2014).

28 Israelachvili, J. The different faces of poly(ethylene glycol). *P Natl Acad Sci USA* **94**, 8378-8379, doi:10.1073/pnas.94.16.8378 (1997).

29 Branca, C., Magazu, S., Maisano, G., Migliardo, P. & Villari, V. Conformational distribution of poly(ethylene oxide) in molten phase and in aqueous solution by quasi-elastic and inelastic light scattering. *J Phys-Condens Mat* **10**, 10141-10157, doi:10.1088/0953-8984/10/45/004 (1998).

30 Faraone, A. *et al.* The puzzle of poly(ethylene oxide) aggregation in water: Experimental findings. *J Chem Phys* **110**, 1801-1806, doi:10.1063/1.477888 (1999).

31 Micali, N., Mineo, P., Vento, F., Nicosia, A. & Villari, V. Supramolecular Structures Formed in Water by Graphene Oxide and Nonionic PEGylated Porphyrin: Interaction Mechanisms and Fluorescence Quenching Effects. *The Journal of Physical Chemistry C* **123**, 25977-25984, doi:10.1021/acs.jpcc.9b06800 (2019).

4 PVAc supported Graphene Oxide–Porphyrin nanosystem as a sustainable photocatalyst for water remediation

4.1 Introduction

The huge impact of human activities on the environment has influenced the terrestrial biosphere, sometimes so deeply to introduce xenobiotic pollutants into groundwater. These events have determined the Anthropocene era.

Civil, industrial, and agro-industrial wastewater, but also farm wastes are the main source of pollutants. In particular, pesticides and herbicides contain organic substances which are non-biodegradable, persistent, and could also be bioaccumulated, known as Persistent Organic Pollutants (POPs).

Thus, the actual effort is focused on the development of sustainable systems to pursue environmental remediation, efficiently using renewable energy sources. In particular, photocatalysis has gained the attention of the researcher because of the possibility to exploit solar radiation as an infinite and renewable energy source. Indeed, when the electromagnetic radiation interacts with a suitable photocatalyst, the production of an electron-hole pair is induced: these species could degrade the pollutant through a redox reaction directly, or generating secondary oxidizing species.

A suitable material for photocatalysis must be sensitive to solar radiation (visible and near UV), chemically inert, and cheap.[1,2] The metal oxide-based semiconductor materials represent a master in photocatalysis, despite the band-gap of the metal oxides usually falls into the UV-region.

In particular, titanium dioxide nanoparticles (TiO_2 NPs) are well-known as one of the most efficient photocatalysts in several applications.[3,4] Although its band-gap (~3.2 eV) makes it active upon UV irradiation[5] (reducing the photonic efficiency when exposed to solar radiation), the TiO_2 NPs are largely used for water remediation purposes.[4,6] Moreover, it has been already used also to produce self-cleaning surfaces and/or other value-added materials.[7-9] As an example, concrete in blend with TiO_2 NPs are used to produce self-cleaning white surfaces and/or de-pollution cementitious materials.[10]

In order to improve the quantic efficiency by reducing the band-gap, the materials doping with other metals represent a common strategy.[11]

On the other hand, the production of these inorganic semiconductor materials involves expensive transition metals, could express toxicity, and requires suitable production methods to obtain particular crystalline structures.[12]

A potential greener alternative could be the use of organic-based photocatalysts. Nature provides a lot of examples of organic compounds able to interact with visible solar radiation to pursue biological

needs (i.e. chlorophyll). It has been demonstrated that a lot of water-soluble aromatics, heterocycles and highly conjugated compounds (i.e. dyes, porphyrins, and phthalocyanines) can interact with electromagnetic radiations falling into the visible region, generating singlet excited states which could induce energy transfer processes or intersystem crossing to triplet excited states involved in both energy and charge transfer.

These features have been adopted to produce novel carbon-carbon bonds by photocatalyzed reactions,[13] in solar cells,[14] photodynamic therapy[15] but also for wastewater depuration and environmental remediation.[16] Indeed, it has been shown that these organic photocatalysts could directly or undirectly oxidize pollutants through different reaction pathways for each particular pollutant (Figure 4.1). Briefly, the photocatalyst (P) could absorb light at suitable wavelength and reaches the first singlet excited state ($^1P^*$). Then, $^1P^*$ could react with the pollutant (Q) directly through an electron transfer reaction[17] (path *a*), or could undergo intersystem crossing to produce a triplet excited state ($^3P^*$). Both singlet or triplet excited states could react with water producing hydroxyl radicals $OH^\bullet$ (paths *b* and *c*).[18,19] The $^3P^*$ can also induce electron transfer reactions (path *d*) or reacts with oxygen through energy transfer process (path *e*) producing singlet oxygen.

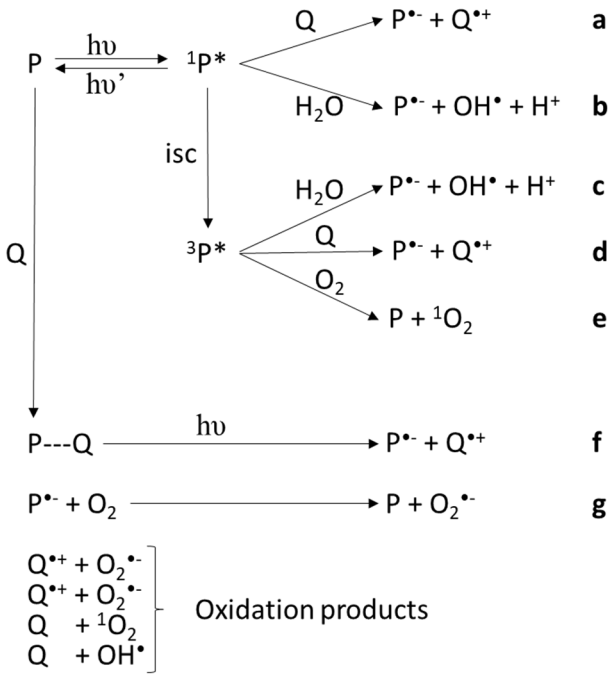

Figure 4.1 Schematic illustration of the most probable photocatalytic degradation pathways.[16] P represents the photocatalyst, Q represents the pollutant.

The ground state of P and Q could also form a complex able to absorb light, resulting in charge separation (path *f*). The semi-reduced form of P ($P^{\bullet-}$) could react with molecular oxygen generating

superoxide radical anion (path *g*). This last species, together with molecular oxygen could furtherly oxidize the pollutant radical cation ($Q^{\bullet+}$). The Q could be sensitive also to singlet oxygen or hydroxyl radicals.

Although these features make homogeneous photocatalysts interesting, their efficiency and stability must be increased to be competitive with the semiconductor-based heterogeneous photocatalysts. The heterogenization improves the stability of these systems by improving the photocatalyst easiness of separation and recycling from de-contaminated water.[16] A reasonable approach consists in using polymers as support: besides the increased photocatalyst stability, it also provides the possibility to apply the photocatalyst in the form of thin films over any suitable substrate.

Among the potential polymer matrices, PolyVinyl Acetate (PVAc) is a suitable candidate as support, due to its stability, filmability, and its transparency to visible light radiations.

The polymer-supported approach could represent a potential industrial-scale application due to the easiness of deposition over several substrates in the form of thin films, and the simplification of the continuous mode depollution.

From a theoretical point of view, by using systems able to act as electron donor and/or acceptor it is possible to mimic the semiconductor photocatalysts. The excited state of the solar antenna, coupled with the electron acceptor system, will act as the electron-hole pair of the semiconductor photocatalyst.

Reduced Graphene Oxide (rGO), thanks to its highly conjugated π structure, could act also as electron acceptor system. Moreover, thanks to its high surface area, could help the photocatalytic processes by adsorbing the pollutants, thus facilitating their contact with the organic antenna and the consequent photo-degradation.

In this section, a porphyrin derivative (5,10,15,20-tetrakis-*p*-hydroxyphenyl-porphyrin, P) as the solar antenna, and rGO as electron acceptor platform have been used to synthesize a covalent nano-system with photocatalytic properties. A reaction involving the nucleophilic attack of the P to the GO structure has been specifically developed. The resulting nanosystem has been named as GOxhyrin, as a fusion of the names of its components. The effects of the reaction conditions on the GO platform have been deeply investigated. In order to produce a nanosystem to be used as "blank" by substituting the P with a molecule insensitive to solar radiation, a covalent complex involving GO and Bisphenol A (BPA) has been synthesized as well. The obtained nanosystems have been characterized by means of UV-vis and fluorescence spectroscopies, Thermogravimetrical analysis, and Differential Scanning Calorimetry. Moreover, the P content of the nanosystem was determined also employing Boron Bromide to induce the cleavage of the ether bonds.

Firstly, the GOxhyrin photo-catalytic properties have been investigated in the form of water suspended powder. Furtherly, by means of "*in-situ*" polymerization, PVAc was used as a support to produce nanocomposites containing GOxhyrin or GO-BPA.

The photocatalytic activity of the resulting nanocomposites has been verified by using them in the form of thin films for photocatalytic degradation experiments of a dye used as mimicking pollutant in water. In particular, Methylene Blue (MB) which photocatalytic degradation relies on a pseudo first-order kinetic was used.[20,21]

4.2 Materials and Methods

Graphene Oxide was purchased by Nanesa s.r.l. Other reagents and solvents were purchased from Sigma Aldrich.

GOxhyrin synthesis

The Graphene Oxide (GO) was previously treated with EDTA to remove any residual of metals. A volume of 22 mL GO water solution (4.5 g/L) was centrifuged (9000 rpm, 20 min, 10 °C), and the precipitate was collected. Then, it was washed two times with 8 mL of EDTA solution (0.1 M) by sonication for 2 minutes and separated by centrifugation. The treated GO was then washed two times with 8 mL of LC-grade water by means of the same procedure. The obtained precipitate was put into a three-neck round bottom flask and diluted up to 22.2 mL with LC-grade water, in nitrogen atmosphere.

An amount of 55.9 mg (82 µmol) of 5,10,15,20-tetrakis-[*p*-hydroxyphenyl]-porphyrin was solubilized in 3.37 mL of sodium hydroxide water solution (0.1 M), so obtaining a sodium porphyrinate (P-Na) solution 24.5 mM (scheme in Figure 4.2, and image in Figure 4.3-A).

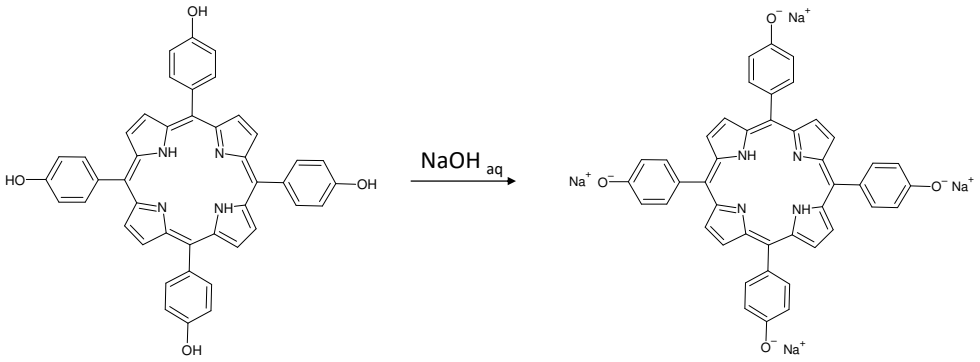

Figure 4.2 Scheme of the 5,10,15,20-tetrakis-[p-hydroxyphenyl]-porphyrin salification.

The reaction was performed by adding the P-Na through volumes ranging from 10 to 400 µL into the treated GO in bubbling nitrogen and under reflux (Figure 4.3-B). Every P-Na addition was spaced from the subsequent by 1 hour to 5 hours, proportionally to the volume added. A total amount of 24.5 µmol of P was added (14% w/w with respect to the GO).

After 13 days, the reaction mixture was slowly cooled to room temperature and then diluted in 200 mL of phosphate buffer solution (PBS, 50 mM), to neutralize the non-reacted P-Na to P (Figure 4.3-C). The resulting mixture was centrifuged (9000 rpm, 10 °C, 20 min), the precipitate was separated and rinsed two times with water (LC-MS grade) through stirring and centrifugation. The precipitate was recovered and dried in vacuum oven (50°C, 12 hours). To get rid of the non-reacted P, the powder was then washed with THF (10 mL) through sonication (2 min) and centrifugation (9000 rpm, 15 min, 5 °C), until the supernatant showed (through Uv-Vis analysis) the absence of P. Finally, the obtained GOxhyrin was dried in vacuum oven (50 °C, 12 hours).

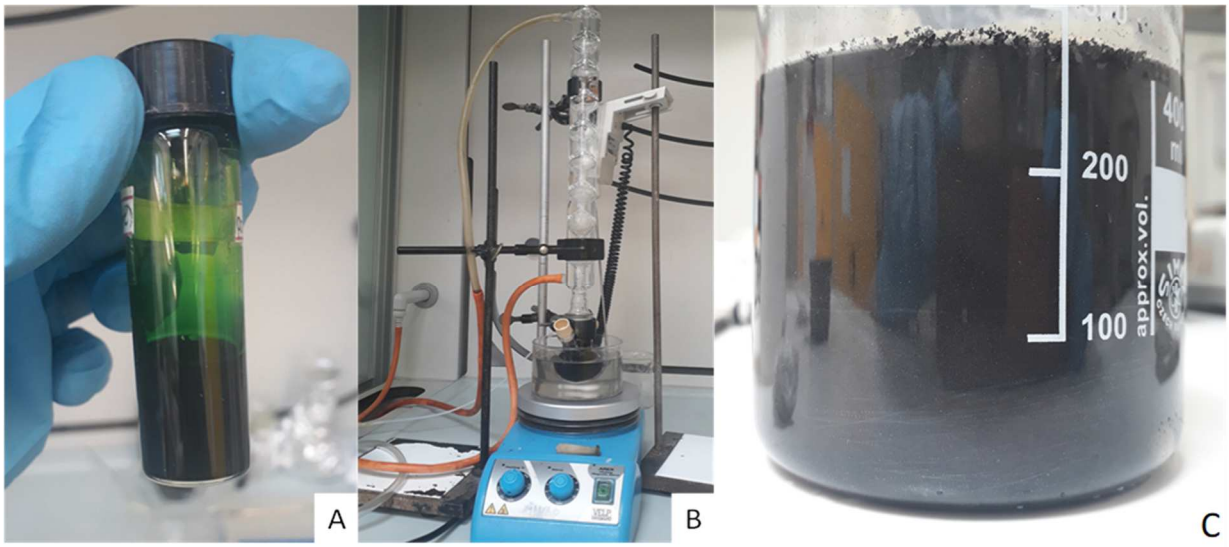

Figure 4.3 A) Porphyrinate solution 24.5 mM; B) Apparatus used to perform the reaction; C) Reaction mixture precipitated in PBS.

GO-BPA synthesis

Briefly, 22 mL of an EDTA treated GO water solution (4.5 g/L) was put into a three-neck round bottom flask in nitrogen atmosphere.

Then, 18.9 mg (83 µmol) of Bisphenol A (BPA) was dissolved into 1.69 mL of a sodium hydroxide water solution (0.1 M). The obtained salt was then diluted with water until a final BPA salt concentration of 24.5 mM.

The reaction was conducted under reflux, by adding the BPA sodium salt solution into the three-neck round bottom flask containing the treated GO and with bubbling nitrogen. The addition was performed through a similar procedure than that of the GOxhyrin, until a final amount of 24.5 µmol of BPA sodium salt was added. After 13 days, the mixture was cooled to room temperature and then precipitated in 200 mL PBS solution (50 mM). The mixture was centrifuged (9000 rpm, 10 °C, 20 min), the precipitate was separated and rinsed two times with water (LC-MS grade) through stirring and centrifugation. The precipitate was recovered and dried in vacuum oven (50°C, 12 hours).

GO-blank

To investigate the effects of the reaction conditions towards the Graphene Oxide structure, in particular, the role of the high temperature and the effect of the base, two new systems have been produced, namely GO_{hot} and GO_{base} respectively. For their synthesis, 22 mL of an EDTA treated GO water solution (4.5 g/L) was split in two parts (11 mL each) and put separately into two different three-neck round bottom flask in nitrogen atmosphere. Then, the one related to GO_{hot} was left under reflux and nitrogen bubbling.

Instead, the one related to GO_{base} was left under reflux and bubbling nitrogen, and has been subjected to the additions of aliquots of sodium hydroxide water solution (0.1 M), by using the same volumes described previously for the GOxhyrin, until reaching a total amount of $4.9*10^{-5}$ mol.

After 13 days, both samples were cooled to room temperature. Every reaction mixture was precipitated in 100 mL PBS (50 mM). Then, every mixture was centrifuged (9000 rpm, 10 °C, 20 min), the precipitate was separated and rinsed two times with water (LC-MS) grade through stirring and centrifugation. The precipitate, respectively GO_{hot} and GO_{base}, were recovered and dried in vacuum oven (50°C, 12 hours).

PVAc-based nanocomposites synthesis

The vinyl acetate (VAc) was previously purified from the inhibitor through a chromatographic column filled with Basic Aluminum oxide and sodium sulphate anhydrous. The 2,2-Azo-bis-isobutyronitrile (AIBN) was used as initiator.

A proper amount of the purified monomer was added into an 8 mL vial and, after the addition of the nanosystem, the mixture was left in a sonicating bath for 30 minutes. Then, a proper amount of initiator was added. The vial was then put into an oil bath at 55°C, under stirring, for 20 hours.

A final solid polymeric mixture was obtained, which was further solubilized in THF (10 mL) and precipitated in *n*-hexane (60 mL). The simplified reaction scheme is reported in Figure 4.12.

By means of this procedure the PVAc-GOxhyrin A 3% and 1 % and the PVAc-GO-BPA were produced.

In order to verify wheter the covalent bond between GO and P influences the photoactivity of the GOxhyrin, a blend with PVAc, GO and P was needed. Therefore, a PVAc homopolymer was synthesized firstly by using purified VAc as the monomer and AIBN as the initiator, leaving the mixture under stirring for 20 hours (55°C) as previously described for the nanocomposites. The PVAc structure has been confirmed through MALDI-TOF mass spectrometry. The spectrum (Figure 4.4) is composed of series of peaks: at m/z 693+n86 (n from 0 to 24) attributed to [M] Na^+ species (*), and at m/z 709+n86 (n from 0 to 20) attributed to [M] K^+ species (#).

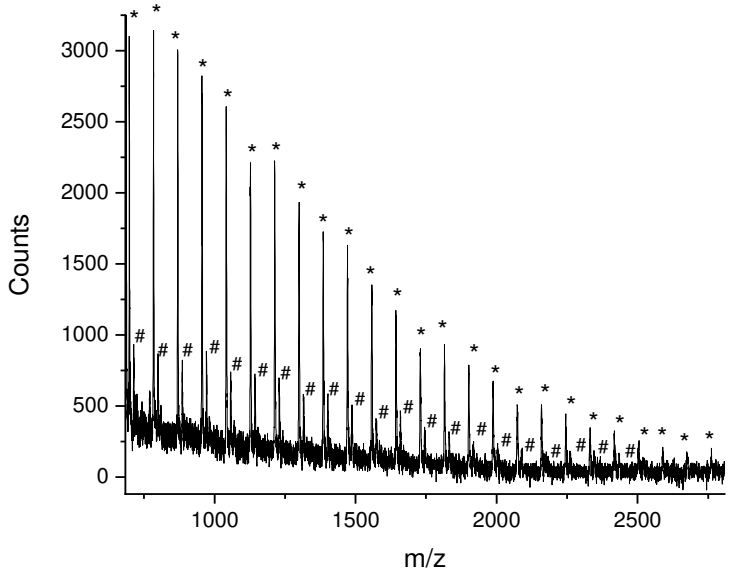

Figure 4.4 MALDI-TOF Mass spectrum of PVAc.

Then, the blend called Blend-PVAc was produced by solubilizing 1.5 mg (2.2 µmol) of P in 1 g (11.6 mmol) of purified VAc, into an 8 mL vial. Then, 48.84 mg of GO in powder form were added, and the mixture was sonicated for 30 minutes. Then 122 mg (0.7 mmol) of AIBN were added, and the vial put into an oil bath at 55°C, under stirring, for 20 hours. The amount of AIBN was previously optimized in order to overtake the radical scavenger ability of the P. The Blend-PVAc was further purified by solubilizing it in THF and precipitating in *n*-hexane as described above.

All the details of the described synthesis have been summarized in Table 4.1.

Table 4.1 Homopolymer, nanocomposites and blend polymerization details.

Homopolymer and	***VAc***		***AIBN***		**Nanofiller**	
Nanocomposites	(g)	(mmol)	(mg)	(mmol)	(mg)	
PVAc	1	11.6	38.2	0.2	/	
PVAcGOxhyrin 3%	1	11.6	38.2	0.2	31.17	
PVAcGOxhyrin 1%	1	11.6	38.2	0.2	10.16	
PVAcGOBPA	1	11.6	38.2	0.2	10.37	
Blend-PVAc	1	11.6	122	0.7	*48.84 (GO)*	*1.5 (P)*

Cleavage of the GO-Porphyrin ether bonds

In order to quantitatively calculate the amount of P bond to the GO platform within GOxhyrin nanosystem, a reaction suitable to break ether bonds was adopted.[22] Briefly, an aliquot of 5 mg of GOxhyrin was stirred into 2 mL of anhydrous acetone. Then, 50 µL (0.53 mmol) of Boron Bromide (BBr_3) were added. The reaction was performed in ice bath, under stirring and in anhydrous nitrogen atmosphere. After 24 hours, 1 mL of water (LC-MS grade) was added and the mixture stirred for 5 minutes. The water phase was separated through centrifugation, and the precipitate was dried in a vacuum oven. Then, the dried powder was washed with several aliquots (1 mL each) of acetone and THF, through sonication and further centrifugation. All the supernatant obtained were collected, dried in vacuum oven (50°C) and solubilized in THF (2 mL).

Preparation of thin-films

To produce the thin-film adopted for the UV-vis measurements starting from the homopolymer (PVAc) and the nanocomposites (PVAc-GOxhyrin 1% and 3%, and PVAc-GO-BPA), a drop-casting method was adopted. Briefly, an aliquot of the sample (100 mg) was dissolved in 1 mL of a mixture of dichloromethane-diethyl ether (1:1). Then, the solution was dropped onto a Petri dish containing deionized water. After evaporation of the organic solvent, the film was ready to be picked up using tweezers and dried under nitrogen-flux.

In order to produce the thin-films to be used during the photocatalytic experiments, for each material, about 15 mg of sample were dissolved in THF (1.5 mL) and drop-cast through the use of a Pasteur pipette onto the inner wall of a 150 mL glass test tube, covering only 180° of the test tube circumference.

Photocatalytic experiments

The photocatalytic experiments were performed in an open wall homemade apparatus (Figure 4.5) equipped with a solar mimicking lamp (OSRAM Ultra Vitalux 300 W E27), a fan, and a magnetic stirrer. Due to the high lamp power, the fan was needed to maintain the temperature inside the chamber at about 35 °C during the whole test. A 150 mL glass test tube (200x30 mm) was opportunely fixed onto the stirrer, at a distance of about 30 cm from the lamp, in a perpendicular position. As a standard procedure, a Methylene Blue solution (MB, $1*10^{-5}$ M) was put into the glass test tube and left in the dark under stirring for 60 minutes. Then, the light was turned on and aliquots of the MB solution were collected every 20 minutes, for two hours totally.

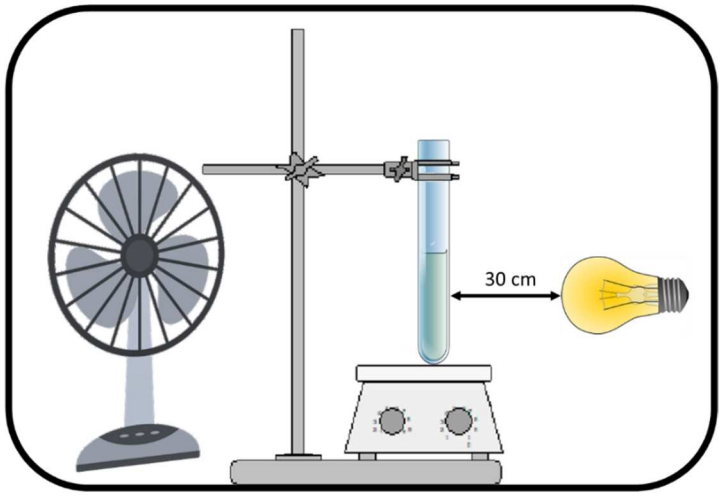

Figure 4.5 Simplified scheme of the home-made photocatalytic experiments apparatus.

4.3 Structural and functional characterizations

GOxhyrin

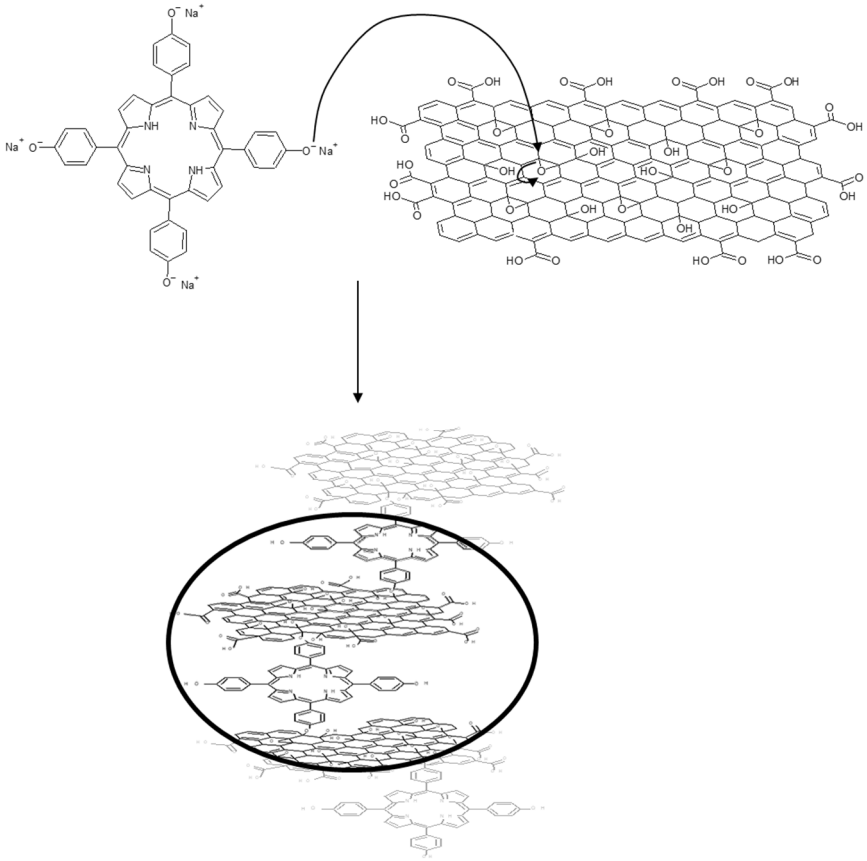

Figure 4.6 Simplified scheme of the GOxhyrin synthesis.

The synthetic pathway of the GOxhyrin was developed to pursuit a covalent bond of the porphyrin moiety onto the GO platform core. The nucleophilic attack of the porphyrin's phenolic groups to the epoxides of the GO was performed by adding very low volumes of P-Na solution to the GO water solution, to maintain the GO in excess and push the reaction towards the formation of the reticulated product (Figure 4.6).

The photocatalytic efficiency of an organic graphene-based system is essentially influenced by the electronic conjugation between the antenna system and the electron acceptor. A covalent bond between the P moiety and the GO platform might ensure such an electronic pathway. The P (1 μM THF solution, Figure 4.7, short dashed line) exhibits a UV-vis absorption profile characterized by the S_0-S_2 transition at 421 nm (the Soret band) and the S_0-S_1 electronic transition revealed by four Q-bands at 517, 553.4, 594.6 and 652.1 nm.

The GO (aqueous solution 4.5 mg/L, Figure 4.7, dashed line) shows the π-π* transition at 230 nm and the n-π* transition at 295 nm. The GOxhyrin (aqueous solution 36 mg/L, Figure 4.7, continuous

line) presents a low intensity absorption band at 267 nm, which is suspected to be a reduced-GO absorbance; moreover, a red-shift of the P signal up to 478 nm (Soret band) and other signals attributable to Q-bands at 593, 628, 675, 708 nm are evidenced. It is noteworthy to say that another absorption signal at 765 nm is evident, and attributable to the protonated P.

Despite the red-shift of the Soret band is usually attributed to the protonation of the porphyrin tetrapyrrolic core, it is not unequivocal. Indeed, it is also known as a result of the supramolecular interaction between the acid groups of the GO and the tetrapyrrolic core of the porphyrin derivative.[23]

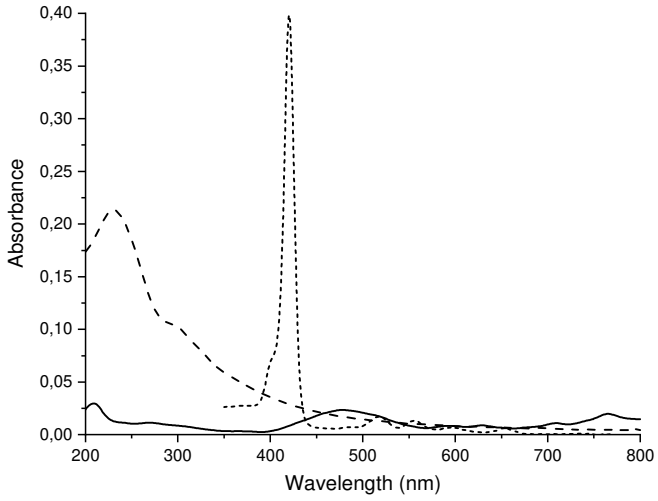

Figure 4.7 UV-vis spectra of GO (dashed line), P (short dashed line) and GOxhyrin (continuous line).

The GO moiety is well-known as an optical quencher of the dyes adsorbed onto its surface, thanks to FRET mechanisms.[24,25] So, it is not suitable to use the UV-vis spectra of GOxhyrin to quantitatively define the content of P.

Also in the case of GO-BPA the UV-vis spectra is not a reliable source of information: as can be seen from the GO-BPA UV-vis spectra (Figure 4.8, continuous line), the scattering strongly influences this system hiding the eventual BPA absorption (7.8 mg/L, Figure 4.8, dotted line).

Anyway, since the GO acts as an optical quencher and hides the dye absorption profile, the scattering of these samples might be due to other modifications that happened to the GO-based system.

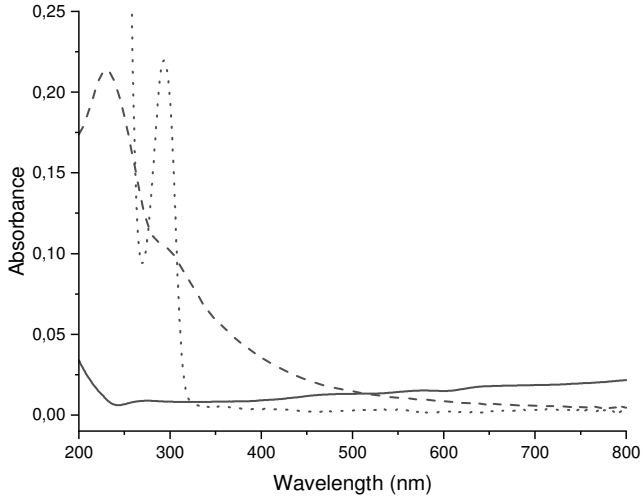

Figure 4.8 UV-vis spectra of GO (dashed line), BPA (dotted line) and GO-BPA (continuous line).

The thermogravimetrical analysis of the GOxhyrin was compared with those of pure GO and P (run in N_2 atmosphere). The GO (Figure 4.9, black line) exhibits a main weight loss at 160 °C and a minor one at 540°C, attributed to the oxygen moieties of the GO platform (Figure 4.9, black line). Instead, the P (Figure 4.9, green line) presents only one main weight loss starting at 260°C. The nanosystem GOxhyrin (Figure 4.9, red line) losses about 13 % at 305 °C, which might be due to the conjugation with the porphyrin and/or to the reduction of the GO platform.

About the BPA, this shows its thermal decomposition starting from 220 °C, which occurs almost totally on the sample leaving any residue (Figure 4.9, magenta line). On the other hand, the thermogram of the GO-BPA is characterized by the absence of any weight loss until 500 °C (Figure 4.9, cyan line), then, a weight loss of about 35 % starting from about 520°C is detected.

To shed light on such a thermal decomposition behaviour of GOxhyrin and GO-BPA, also the GO samples which were subjected to the etherification reaction conditions in absence of crosslinking agent (P or BPA) were analysed: in particular, referring to high temperatures in water and alkaline conditions, these samples were called respectively GO_{hot} and GO_{base}.

The thermogram of GO_{hot} (Figure 4.9, blue dashed line) clearly shows the absence of any weight loss, apart from a slight one at 305 °C (16%), indicating that the GO reduction is occurring due to the high temperature in water solvent.[26,27]

On the other hand, the thermogram of GO_{base} (Figure 4.9, red dashed line) shows a slope variation at about 305°C and a main weight loss at 540 °C (23%): this last weight loss, since the use of sodium hydroxide during the synthesis of GO_{base}, might be attributed to the presence of hydroxyl groups onto the GO platform, resulting from the opening of the epoxides of the GO. Anyway, the absence of any

noteworthy weight loss in the thermograms up to 500°C is enough to attest the reduction of the GO platform subjected to the reaction conditions adopted.[28]

It is noteworthy to highlight the similarity between the GO_{hot} and GOxhyrin thermograms, and the other one between GO_{base} and GO-BPA thermograms. Probably, it resides in the structural differences of the cross-linkers. Indeed, besides the tetra-functionality of P and the bi-functionality of BPA, the P has a bigger steric hindrance than the BPA. These features can facilitate its coming into contact with GO sheets, increasing the GO degree of functionalization that consequently results in the disappearance of the weight loss above ~500°C. Instead, BPA needs a close contact between GO moieties to cross-link, which could be avoided by the residual oxygenated groups present on the GO platform. Anyway, the results from UV-vis analysis and the TGA profiles of both GOxhyrin and GO-BPA suggest the occurring of reduction processes of the GO platform, simultaneously with the etherification reaction. Thus, it was not possible to quantitatively define the amount of P or BPA bonded to the GO considering the TGA residues.

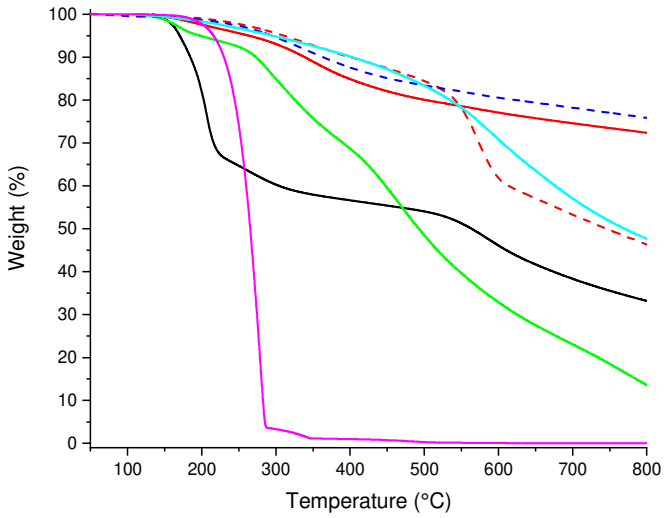

Figure 4.9 Thermograms of GO (black), P (green), Goxhyrin (red), GO_{base} (red dashed), GO_{hot} (blue dashed), GO-BPA (cyan), BPA (magenta).

In order to quantitatively measure the amount of P bound to the GO plaform, a reaction was performed to cleave the ether bridges by means of Boron Bromide (BBr_3) and extraction of P from GOxhyrin.[22] The reaction occurs through the pathway shown in Figure 4.10.

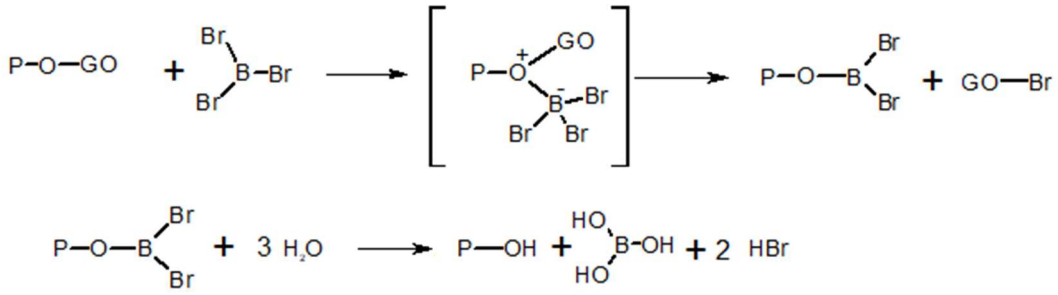

Figure 4.10 Scheme of the ether bond cleavage through the reaction with Boron Bromide.

The UV-vis analysis of the extracted from the hydrolysis product in THF solution, shown in Figure 4.11, points out the presence of two Soret bands at 421 nm and 457 nm attributable to the neutral P together with its protonated form, respectively. As a confirm, also the Q-band related to the protonated P is visible at 702 nm. Such a UV-vis spectrum profile is in accordance with the reaction environment, where hydrobromic acid is produced from Boron Bromide, which could protonate the porphyrin core. As a confirm of the P presence, also the typical porphyrin fluorescence emission centered at 654 nm (λ_{exc}= 420 nm) was evidenced. The fluorescence emission of the protonated moiety is quenched (λ_{exc}= 450 nm). Therefore, taking into account the molar extinction coefficient of the neutral and protonated P in THF (354760 $M^{-1}*cm^{-1}$ and 298700 $M^{-1}*cm^{-1}$, respectively), the 0.54% (w/w) of P in GOxhyrin was calculated. Moreover, such a reaction also confirmed the occurrence of ether bond linking P and GO.

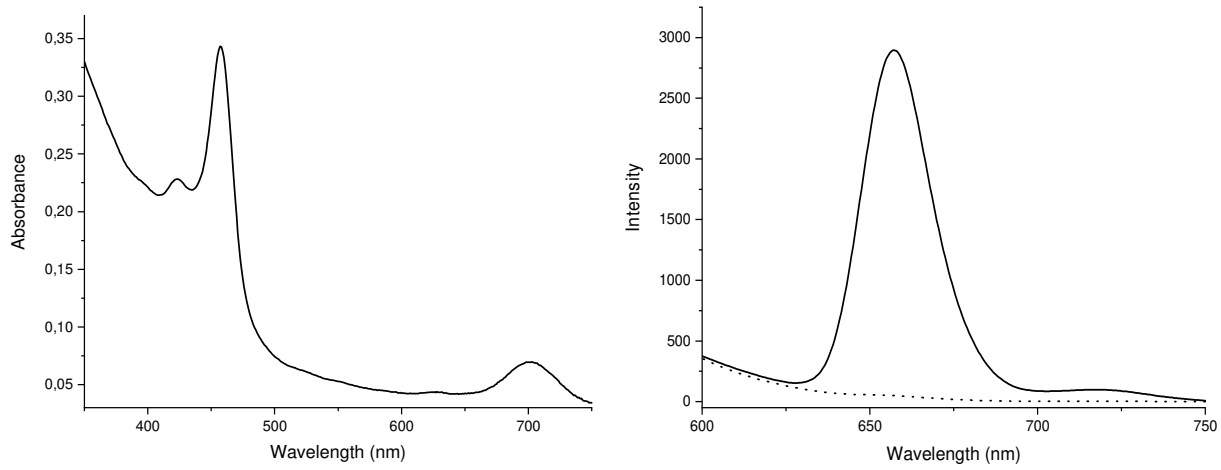

Figure 4.11 UV-vis (left) and fluorescence emission (right) spectra of supernatant related to the ether cleavage reaction.

Once defined the covalent linkage in GOxhyrin, a nanocomposite has been produced by *in-situ* polymerization of the Poly-Vinyl Acetate (PVAc). As nanofillers were used both the GOxhyrin and the GO-BPA, in order to obtain the photoactive nanocomposite (PVAc-GOxhyrin) and the blank (PVAc-GOBPA). In particular, two PVAc-GOxhyrin have been produced by varying the amount of filler loaded, respectively the 3% and 1% (w/w). A simplified scheme of the nanocomposite structure is exposed in Figure 4.12: since the radical polymerization involving PVAc, a copolymer with GOxhyrin results from the opening of the unsaturated carbon bonds of the GO platform.

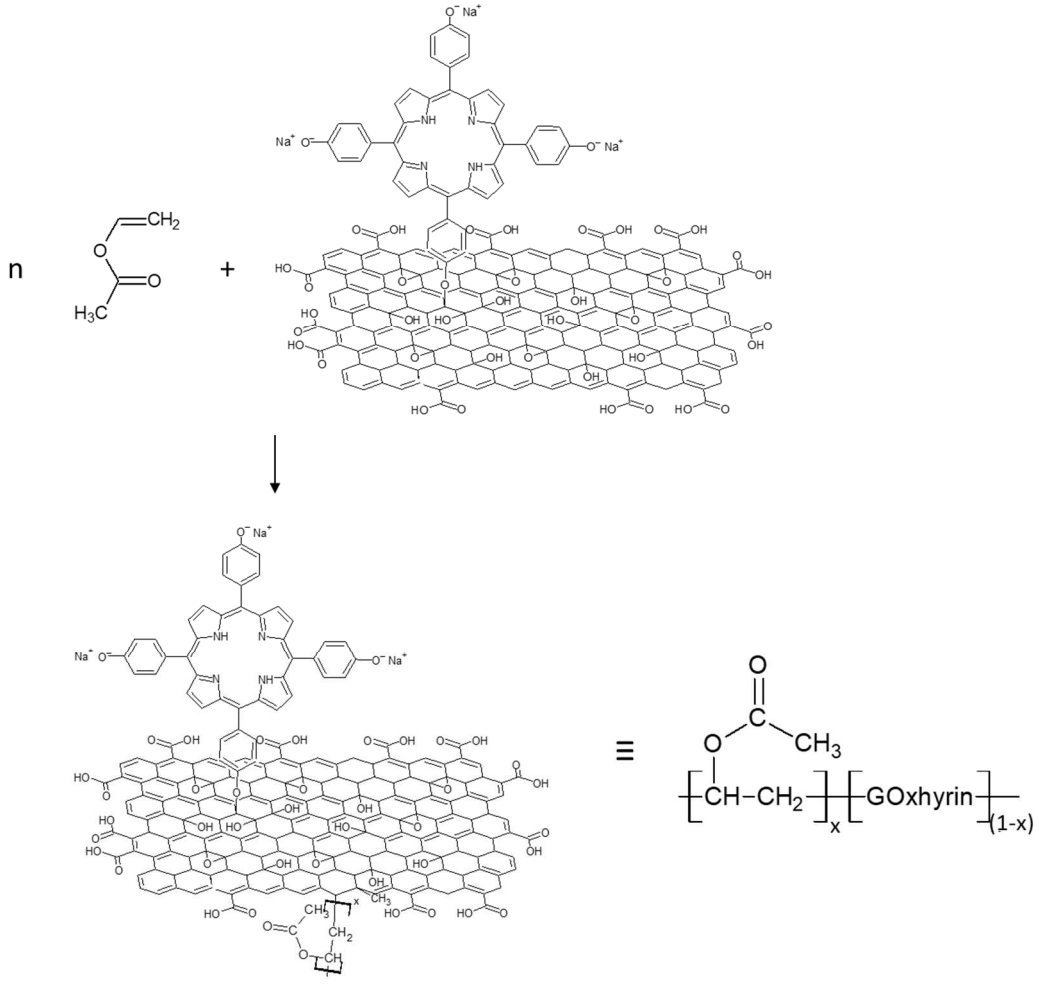

Figure 4.12 Simplified illustration of the PVAc-GOxhyrin synthesis.

To define the spectroscopic properties of the nanocomposites, UV-vis measurements have been performed on their thin films. By analysing the PVAc spectrum (Figure 4.13, dotted line), it can be assumed as transparent in the region 300-800 nm. The same observation could be accepted for PVAc-GO-BPA (Figure 4.13, dashed line). In contrast, the PVAc-GOxhyrin spectrum (Figure 4.13, continuous line) shows a broad exponential absorption from 800 up to 300 nm, to which are

overlapped the absorption signals typical of the GOxhyrin moiety: in particular, are clearly visible bands at 423 nm and 517 nm, respectively attributable to the P Soret band and the first Q-band, and another band at about 700 nm attributable to the Q-band of the protonated P.

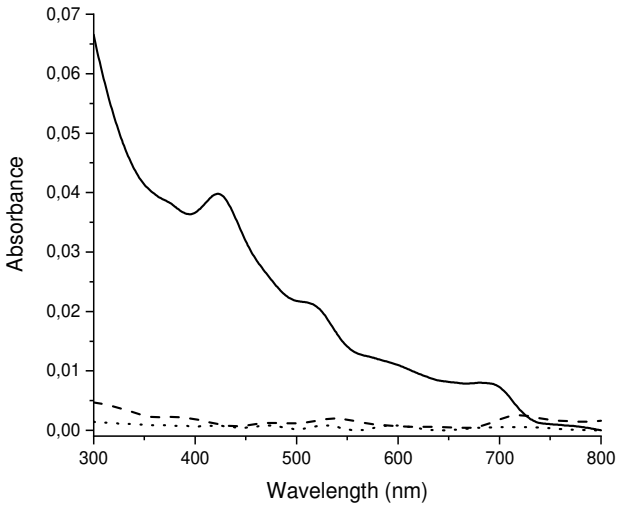

Figure 4.13 UV-vis spectra of PVAc (dotted line), PVAc-GO-BPA (dashed line) and PVAc-GOxhyrin 1% (continuous line)

From the thermal stability point of view, the PVAc (Figure 4.14, red line) shows its deacetylation process at 320°C, while the second weight loss at 436°C is due to the break of the C-C bonds within the polymer chain and the release of volatile aromatic moieties.[29] A residue of about 4.7% at 800°C is also present, due to the carbon residue intrinsic of the degradative pathway.

The thermal characterization of the nanocomposites and the blend-PVAc has revealed that the presence of the nanofiller does not produce any qualitative difference in the PVAc thermal properties. Indeed, the PVAc-GOxhyrin 3% (Figure 4.14, blue line), the PVAc-GO-BPA (Figure 4.14, green line) and the Blend-PVAc (Figure 4.14, cyan line), qualitatively retrace the thermal degradation pathway of the PVAc, with the first degradation occurring at 320 °C and the second one at 436 °C.

The relative content of the nanofiller within the polymer matrix has been calculated taking into account the different residue at 800°C (TGA run in N_2). The results are reported in Table 4.2, and are in accordance with the filler amount added during the synthesis.

Table 4.2 Comparison of the relative content of filler within the nanocomposites between the theoretical amount and the TGA residue.

Nanocomposite	**Nanofiller**	
	Theoretic (%)	TGA (%)
PVAc-GOxhyrin 3%	3	3.14
PVAc-GOxhyrin 1%	1	1.28
PVAc-GO-BPA	1	1

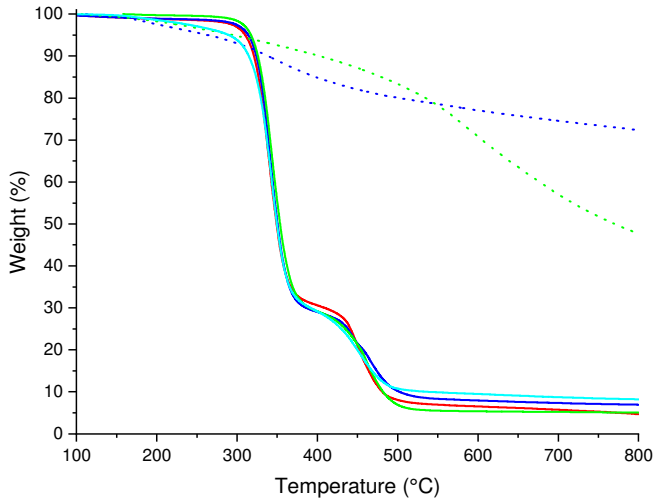

Figure 4.14 TGA thermograms (N_2 atmosphere) of PVAc (red line), Blend-PVAc (cyan line), PVAc-GOxhyrin (blue line) and PVAc-GO-BPA (green line). The respective GOxhyrin (blue dashed line) and GO-BPA (green dashed line) TGA thermograms are also reported for comparison.

Instead, the glass transition temperature (Tg) of the polymer is influenced by the nanofiller presence. The DSC trace of PVAc (Figure 4.15, red line) shows the Tg at 42°C, while both the nanocomposites PVAc-GOxhyrin 3% and PVAc-GO-BPA (Figure 4.15, blue and green line respectively) show increased Tg at 44°C. Interestingly, the Blend-PVAc shows a lower Tg (38°C), probably due to the higher disorder of the polymer chains due to the presence of GO and P as independent moieties dispersed into the polymer matrix.

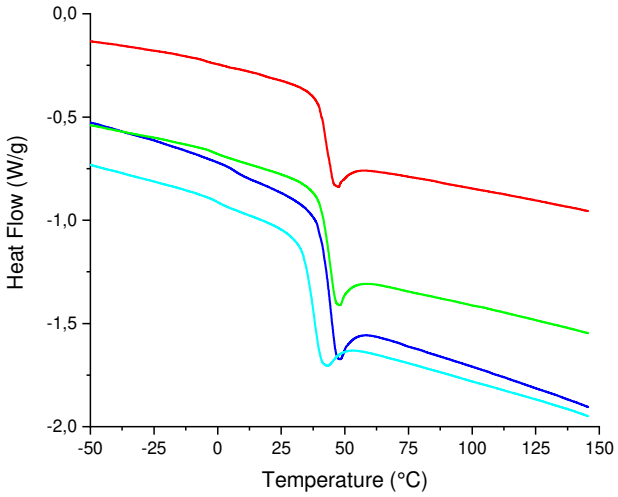

Figure 4.15 DSC traces of PVAc (red line), Blend-PVAc (cyan line), PVAc-GOxhyrin (blue line) and PVAc-GO-BPA (green line).

Photocatalytic activity

The presence of a covalent bond between the antenna-dye (porphyrin) and the reduced GO platform might improve the efficiency of the electron transfer processes, which promote the photocatalytic features of the GOxhyrin. In order to investigate on the photocatalytic efficiency of the GOxhyrin nanosystem, Methylene Blue (MB) was chosen as a pollutant mimic to perform a preliminary photocatalytic experiment. The collected samples from the photocatalytic experiments were analysed through UV-vis spectroscopy. The variations of the dye concentration (C/C_0) as a function of the reaction time were monitored. Since the MB photodegradation relies on a pseudo first-order kinetic,[20,21] the linear fit slope of the $log(C/C_0)$ vs *time* plot represents the kinetic constant (k) of the photo-degradation.

Particular care was taken to avoid any overestimation of the photocatalytic activity, by checking the photobleaching event occurring over the MB and by using blank samples to determine any eventual adsorption process.

The MB is well-known to be subjected to photobleaching, so it slowly degrades autonomously under solar irradiation.[30] This evidence occurred also under the conditions adopted in this experiment, so the kinetic of such a photobleaching process is reported in Figure 4.16 (green line). To perform preliminary photocatalytic tests, in every experiment, about 1 mg of catalysts powder was mixed within 100 mL of MB solution ($1*10^{-5}$ M).

Firstly, the nanosystems GO_{base} and GO-BPA were tested and considered as blank: the GO_{base} represents the contribution of the solely GO platform, while the GO-BPA represents the photocatalytic activity of the etherified GO sample. Indeed, the modifies that occurred during the GO

etherification could modify the area of the nanosystem, acting as a crosslinking process between the GO sheet-like structure, and might also alter its electronic properties.

The MB degradation kinetic of GO_{base} (Figure 4.16, cyan) and GO-BPA (Figure 4.16, magenta) are very similar to the photobleaching one, meaning that these nanosystems are not active as photocatalysts. Instead, the GOxhyrin sample exhibited a *k* of about $26*10^{-4}$ min^{-1}, which is definitely higher than the photobleaching and so indisputably attributed to the occurrence of a photocatalytic process induced by the GOxhyrin.

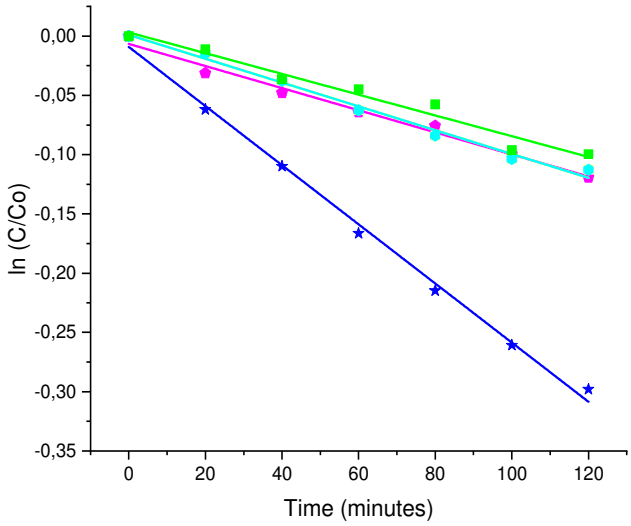

Figure 4.16 Degradation kinetics of MB solutions during the photobleaching test (green), and in presence of GO_{base} (cyan), GO-BPA (magenta) and GOxhyrin (blu). The lines were obtained as the best fit of the data points.

To define the photocatalytic efficiency of the nanosystems, the kinetic constant value has been normalized considering the weight of the nanosystem used (k_{norm}).

The k_{norm} related to the GOxhyrin is 1.91 $min^{-1}*g^{-1}$ (see Table 4.3). Although these experiments indisputably confirmed the GOxhyrin photocatalytic activity, the k_{norm} value is attributed to the complex system GOxhyrin containing the 0.54% (w/w) of P.

Since the photocatalytic activity is attributed to the electron transfer processes between P and GO moieties, an in-depth investigation to point out the effects of the relative P content within the nanosystem is necessary. The optimization of the P content could improve the photocatalytic efficiency of GOxhyrin.

Table 4.3 Experimental details and results related to the photocatalytic experiments of the nanosystems in form of powder. In particular, for each nanosystem have been reported: weight (mg), photo-degradation kinetic constant k (10^{-4} min^{-1}) and k normalized by nanosystem weight ($min^{-1}*g^{-1}$).

Nanosystem	Weight (mg)	k ($*10^{-4}$ min^{-1})	k_{norm} ($min^{-1}*g^{-1}$)
GOxhyrin	1.36	26 ± 1.52	1.91
GOBPA	1.11	- -	- -
GO_{base}	1.29	- -	- -

The practical application of such nanosystems in photocatalysis must overtake some expensive paths, such as the separation of the solution from the photocatalytic powder after the de-pollution processes. The application of photocatalysts in the form of thin film is a promising approach to let water solution be de-polluted without any filtration or separation process after the photocatalytic event.

The photocatalytic activity of the nanocomposites and the blend was tested by applying them as film, deposited from THF solutions. For each system, about 15 mg of sample were dissolved in THF (1.5 mL) and deposited onto the inner wall of the 150 mL glass test tube, covering only 180° of the test tube circumference.

Thus, the PVAc-GOxhyrin photocatalytic activity was compared with its "blank", the PVAc-GO-BPA. Furthermore, to define whether the photocatalytic activity is due to the electronic communication between GO and P, induced through a covalent bond, the photocatalytic activity of the Blend-PVAc was also investigated.

The results of the photocatalytic experiments (Figure 4.17) revealed that, probably due to the presence of the polymer matrix, all the samples analyzed are influenced by an induction time of about 30 minutes (starting from the light turn-on). The PVAc-GO-BPA (Figure 4.17, purple) results inactive from a photocatalytic point of view, in accordance with the results obtained by using GO-BPA powder.

The PVAc-GOxhirin 1% (Figure 4.17, blue) has revealed to be inactive as well. Noteworthy, the PVAc-GOxhyrin 3% (Figure 4.17, red) exhibited a clear photocatalytic activity with a kinetic constant of about $10.5*10^{-4}$ min^{-1}. Thus, it is reasonable that the PVAc-GOxhyrin 1% inactivity was only due to the low amount of GOxhyrin loaded.

As a proof of concept, this data confirms that the photocatalytic activity of this organic photocatalyst is executed also when supported by a polymer matrix, making it interesting for further studies.

Moreover, the inactivity of the Blend-PVAc thin film (Figure 4.17, cyan) despite its high loading (about 5% w/w comprehensive of GO and P) is a confirm of the fundamental need of a covalent

connection between P, which acts as the antenna dye, and the reduced GO platform, which acts as the electron acceptor, to produce a potential polymer supported-photocatalytic organic system.

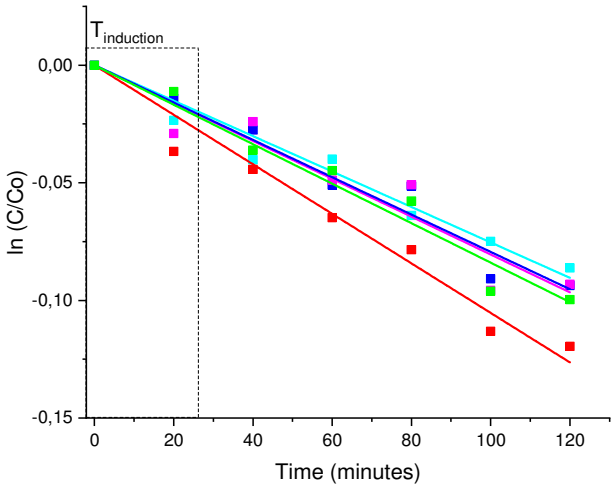

Figure 4.17 Degradation kinetics of MB solutions with PVAcGOxhyrin 3% (red), PVAcGOxhyrin 1% (blue), PVAcGO-BPA (magenta) and Blend-PVAc (cyan), compared with the photobleaching experiment (green). The lines were obtained as the best fit of the data points.

Table 4.4 Experimental details and results related to the photocatalytic experiments of the nanosystems in form of nanocomposites. In particular, for each thin film have been reported: nanofiller content (weight %), nanocomposite amount (mg) used during the photocatalysis experiments, the photo-degradation kinetic constant k (10^{-4} min^{-1}) and k normalized by nanosystem weight ($min^{-1}*g^{-1}$).

Thin film	Nanofiller content (%)	Nanocomposite weighted (mg)	k ($*10^{-4}$ min^{-1})	k_{norm} ($min^{-1}*g^{-1}$)
PVAcGOxhyrin 3%	3.14%	15.09	10.5 ± 0.61	2.22
PVAcGOxhyrin 1%	1.28%	15.19	- -	- -
PVAcGOBPA	0.7%	15.42	- -	- -
Blend-PVAc	4.79%	15.16	- -	- -

4.4 Conclusions

A covalent nanosystem has been synthesized by cross-linking a tetra-hydroxyphenyl porphyrin derivative (P) to the GO platform. The reaction conditions were optimized to pursuit an etherification reaction by exploiting the phenolate groups of the P to perform a nucleophilic attack over the epoxides of the GO platform. Due to the covalent link between the photosensitizer and the carbon platform, the resulting nanosystem named GOxhyrin should perform efficient electron transfer processes, that are involved in photocatalytic activity.

The nanosystem has been characterized through UV-vis and FT-IR spectroscopies. The quantitative determination of the P content was performed by using Boron Bromide, which selectively cleaves the ether bond. Moreover, it also represented indirect evidence of the ether bond formation between P and GO.

The investigation about the structural modifications occurred to the GO platform due to the reaction conditions adopted in GOxhyrin synthesis confirmed that a reduction phenomenon is occurring simultaneously with the etherification. In particular, analyzing the GO blanks, it has been revealed that the solvothermal conditions reduce the GO oxygenated groups while the alkaline conditions could introduce hydroxyl groups on the GO platform.

The photocatalytic activity of GOxhyrin has been evaluated through experiments employing MB as a dye mimicking pollutant. In order to evaluate any absorption phenomenon onto the carbon platform during the photocatalytic experiments, a GO-BPA nanosystem has been synthesised and used as photo-inactive blank. Photobleaching phenomenon occurring on MB has been also taken into account.

Since the polymer-supported photocatalysts represent a cheaper and smarter alternative to the use of photocatalysts in slurry form, PVAc based nanocomposites have been produced by means of *in-situ* polymerization.

The resulting nanocomposite PVAc-GOxhyrin has been characterized through UV-vis spectroscopy, TGA and DSC analyses, and has shown higher glass transition temperatures than the pure polymer, as expected by the nanofiller presence.

The PVAc-GOxhyrin with 3% (w) of GOxhyrin loaded has shown photocatalytic activity during the experiments. Instead, the Blend-PVAc containing a similar amount of GO and P in the form of physical mixture, has been proved inactive in photocatalysis. Probably, the supramolecular interactions between P and GO are not enough to ensure a continuative pathway for the electron transfer processes, leading to the resulting photo-inactivity. On the other hand, these data confirm that the covalent bond between the two moieties of GOxhyrin is fundamental to produce an electron donor-acceptor system suitable for photocatalysis.

Nevertheless, since the photocatalytic efficiency of the nanosystem is based on the P/GO ratio, further investigations are needed to optimize the P content.

The photocatalytic features of PVAc-GOxhyrin exposed in this section represent a proof of concept of a potential cheap and green organic-based photocatalyst. In our knowledge, it is the first polymer-supported graphene-based organic photocatalyst suitable for water remediation.

4.5 References

1 Walter, M. G. *et al.* Solar water splitting cells. *Chem Rev* **110**, 6446-6473, doi:10.1021/cr1002326 (2010).

2 Mills, A., Davies, R. H. & Worsley, D. Water purification by semiconductor photocatalysis. *Chemical Society Reviews* **22**, doi:10.1039/cs9932200417 (1993).

3 Hussain, M., Russo, N. & Saracco, G. Photocatalytic abatement of VOCs by novel optimized TiO2 nanoparticles. *Chemical Engineering Journal* **166**, 138-149, doi:10.1016/j.cej.2010.10.040 (2011).

4 Chong, M. N., Jin, B., Chow, C. W. K. & Saint, C. Recent developments in photocatalytic water treatment technology: A review. *Water Research* **44**, 2997-3027, doi:10.1016/j.watres.2010.02.039 (2010).

5 Pelaez, M. *et al.* A review on the visible light active titanium dioxide photocatalysts for environmental applications. *Applied Catalysis B: Environmental* **125**, 331-349, doi:10.1016/j.apcatb.2012.05.036 (2012).

6 Pozzo, R. L., Baltanás, M. A. & Cassano, A. E. Supported titanium oxide as photocatalyst in water decontamination: State of the art. *Catalysis Today* **39**, 219-231, doi:10.1016/s0920-5861(97)00103-x (1997).

7 Lucas, S. S., Ferreira, V. M. & de Aguiar, J. L. B. Incorporation of titanium dioxide nanoparticles in mortars — Influence of microstructure in the hardened state properties and photocatalytic activity. *Cement and Concrete Research* **43**, 112-120, doi:10.1016/j.cemconres.2012.09.007 (2013).

8 Chen, J. & Poon, C.-s. Photocatalytic construction and building materials: From fundamentals to applications. *Building and Environment* **44**, 1899-1906, doi:10.1016/j.buildenv.2009.01.002 (2009).

9 Faraldos, M., Kropp, R., Anderson, M. A. & Sobolev, K. Photocatalytic hydrophobic concrete coatings to combat air pollution. *Catalysis Today* **259**, 228-236, doi:10.1016/j.cattod.2015.07.025 (2016).

10 Folli, A., Pade, C., Hansen, T. B., De Marco, T. & Macphee, D. E. TiO2 photocatalysis in cementitious systems: Insights into self-cleaning and depollution chemistry. *Cement and Concrete Research* **42**, 539-548, doi:10.1016/j.cemconres.2011.12.001 (2012).

11 Fiorenza, R., Bellardita, M., Scirè, S. & Palmisano, L. Effect of the addition of different doping agents on visible light activity of porous TiO2 photocatalysts. *Molecular Catalysis* **455**, 108-120, doi:10.1016/j.mcat.2018.06.002 (2018).

12 Lazar, M., Varghese, S. & Nair, S. Photocatalytic Water Treatment by Titanium Dioxide: Recent Updates. *Catalysts* **2**, 572-601, doi:10.3390/catal2040572 (2012).

13 Fagnoni, M., Dondi, D., Ravelli, D. & Albini, A. Photocatalysis for the Formation of the C–C Bond. *Chemical Reviews* **107**, 2725-2756, doi:10.1021/cr068352x (2007).

14 Yum, J.-H., Chen, P., Grätzel, M. & Nazeeruddin, M. K. Recent Developments in Solid-State Dye-Sensitized Solar Cells. *ChemSusChem* **1**, 699-707, doi:10.1002/cssc.200800084 (2008).

15 Plaetzer, K., Krammer, B., Berlanda, J., Berr, F. & Kiesslich, T. Photophysics and photochemistry of photodynamic therapy: fundamental aspects. *Lasers in Medical Science* **24**, 259-268, doi:10.1007/s10103-008-0539-1 (2008).

16 Marin, M. L., Santos-Juanes, L., Arques, A., Amat, A. M. & Miranda, M. A. Organic Photocatalysts for the Oxidation of Pollutants and Model Compounds. *Chemical Reviews* **112**, 1710-1750, doi:10.1021/cr2000543 (2011).

17 Hoffmann, N. Photochemical Reactions as Key Steps in Organic Synthesis. *Chemical Reviews* **108**, 1052-1103, doi:10.1021/cr0680336 (2008).

18 Sanjuán, A., Alvaro, M., Aguirre, G., García, H. & Scaiano, J. C. Intrazeolite Photochemistry. 21. 2,4,6-Triphenylpyrylium Encapsulated inside Zeolite Y Supercages as Heterogeneous Photocatalyst for the Generation of Hydroxyl Radical. *Journal of the American Chemical Society* **120**, 7351-7352, doi:10.1021/ja980121n (1998).

19 Sanjuán, A., Aguirre, G., Alvaro, M. & García, H. 2, 4, 6-Triphenylpyrylium ion encapsulated in Y zeolite as photocatalyst. A co-operative contribution of the zeolite host to the photodegradation of 4-chlorophenoxyacetic acid using solar light. *Applied Catalysis B: Environmental* **15**, 247-257, doi:10.1016/s0926-3373(97)00052-0 (1998).

20 Thorat, J. H. *et al.* Architecture of ZnO nanosheets and nanochips via zinc oxalato-hydrazinate complex. *Journal of Nanoparticle Research* **16**, doi:10.1007/s11051-014-2450-y (2014).

21 Fiorenza, R., Bellardita, M., Barakat, T., Scirè, S. & Palmisano, L. Visible light photocatalytic activity of macro-mesoporous TiO 2 -CeO 2 inverse opals. *Journal of Photochemistry and Photobiology A: Chemistry* **352**, 25-34, doi:10.1016/j.jphotochem.2017.10.052 (2018).

22 Ranu, B. C. & Bhar, S. Dealkylation of Ethers. A Review. *Organic Preparations and Procedures International* **28**, 371-409, doi:10.1080/00304949609356549 (1996).

23 Micali, N., Mineo, P., Vento, F., Nicosia, A. & Villari, V. Supramolecular Structures Formed in Water by Graphene Oxide and Nonionic PEGylated Porphyrin: Interaction Mechanisms and Fluorescence Quenching Effects. *The Journal of Physical Chemistry C* **123**, 25977-25984, doi:10.1021/acs.jpcc.9b06800 (2019).

24 Swathi, R. S. & Sebastian, K. L. Long range resonance energy transfer from a dye molecule to graphene has (distance)−4 dependence. *The Journal of Chemical Physics* **130**, doi:10.1063/1.3077292 (2009).

25 Liu, C. H., Wang, Z., Jia, H. X. & Li, Z. P. Efficient fluorescence resonance energy transfer between upconversion nanophosphors and graphene oxide: a highly sensitive biosensing platform. *Chemical Communications* **47**, 4661-4663, doi:10.1039/C1CC10597C (2011).

26 Wang, H., Robinson, J. T., Li, X. & Dai, H. Solvothermal Reduction of Chemically Exfoliated Graphene Sheets. *Journal of the American Chemical Society* **131**, 9910-9911, doi:10.1021/ja904251p (2009).

27 Zhou, Y., Bao, Q., Tang, L. A. L., Zhong, Y. & Loh, K. P. Hydrothermal Dehydration for the "Green" Reduction of Exfoliated Graphene Oxide to Graphene and Demonstration of Tunable Optical Limiting Properties. *Chem Mater* **21**, 2950-2956, doi:10.1021/cm9006603 (2009).

28 Fan, X. *et al.* Deoxygenation of Exfoliated Graphite Oxide under Alkaline Conditions: A Green Route to Graphene Preparation. *Advanced Materials* **20**, 4490-4493, doi:10.1002/adma.200801306 (2008).

29 Costa, L., Avataneo, M., Bracco, P. & Brunella, V. Char formation in polyvinyl polymers I. Polyvinyl acetate. *Polymer Degradation and Stability* **77**, 503-510, doi:10.1016/s0141-3910(02)00108-8 (2002).

30 Nassar, S. J. M., Wills, C. & Harriman, A. Inhibition of the Photobleaching of Methylene Blue by Association with Urea. *ChemPhotoChem* **3**, 1042-1049, doi:10.1002/cptc.201900141 (2019).

5 An on-demand tunable multi-functional nanohybrid system as a potential agent against bacterial contamination

The tunable properties of the polymer-based materials have led to their ubiquitous applications as structural material not only for common use objects but also for value-added devices. As examples, polymer-based materials are employed in kids toys manufacturing, but also to produce biomedical devices such as catheters, ureteral stents and prosthesis.

The bacterial colonisation occurs rapidly if no bactericide agent is applied onto the surface of the material.

Indeed, the bacterial adhesion over a solid surface[1] comes in succession due to the reproduction and the formation of colonies, which develop in biofilms.[2] These could be described as complex structures similar to that of tissues of higher organisms,[3] which allow the bacteria survival in hostile environments thanks to the secretion of exopolysaccharides, extremely protective against bactericide and bacteriostatic agents.[4-8]

Since the strong biofilm resistance, the prevention from the bacterial adhesion over a surface is an important issue in materials science.

In the biomedical field, due to bacterial contaminations, severe infections could occur using invasive devices. Besides the necessity to sterilize the materials before their use,[9] to provide long-term antibacterial efficacy, anti-microbial agents are needed.[10] With this aim, low-weight organic molecules are usually applied as antimicrobial agents and used through spray coating techniques onto objects or blended into the polymer matrix during its processing.[11,12]

Nevertheless, the low adhesiveness, the ubiquitous use of organic-based antimicrobial agents and the subsequential release into the environment has caused the direct exposure of life forms, resulting in bioaccumulation for several species worldwide, including humans.[13,14] It has been recognized worldwide as a serious problem, because of their activity as endocrine disruptors.[15] In particular, due to the risk assessment for human health, some of these molecules have also been banned from both European and American health institutions.[16] Nevertheless, the ban concerned only some particular application, so these additives are still used because of their efficiency towards multiple bacterial targets, especially for biomedical devices coatings (i.e. surgical suture wires).[16]

Nowadays, due to the latest SARS-CoV-2 pandemic, another issue is occurring besides the use of antibacterial agents for biomedical purposes discussed above. The demand of disinfectants agents to ensure sanitised surfaces has seen an exponential rise to reduce the contagion possibilities. The over-

employment of common disinfectants agents (i.e. sodium hypochlorite) resulted in their environmental spreading with toxic side-effects towards the environment and wildlife.[17]

Virus could take advantages from the bacterial contamination: indeed, the viruses could exploit the bacteria biofilm as a shield from the environmental stresses, and then continue the contamination through biofilm spreading.[18]

A solution to these issues is represented by the use of surfaces having intrinsic long-term anti-bacterial properties.

Considering this landscape, thanks to the polymer versatility, a potential approach could be based on antibacterial polymer-based coatings (applied through covalent or physical adsorption, covalent linkages and/or graft copolymerization techniques[19]). The fundamental features of a coating such as the easiness of synthesis and application, the long-term stability in environmental conditions, the absence of any degradation product or toxic product losses, are indeed fulfilled by polymers.

Once defined the proper polymer coating, antimicrobial moieties could be loaded in the polymer matrix and perform their activity towards pathogens. With this aim, several fillers have been tested.[19,20]

In the field of nanotechnology, Silver NanoParticles (AgNPs) have become interesting because of their good conductivity, chemical stability, and catalytic properties which are superior if compared to the bulk material.[20-22] Among all their features, the most important is the antibacterial activity. Silver is well-known as an antibacterial against several micro-organisms, such as Gram-positive and Gram-negative.[23,24] Such peculiar activity is attributable to the release of silver ions that act against pathogens and micro-organisms.[24] It has been discovered a multifaceted mechanism[25] responsible of the broad-spectrum activity of the AgNPs towards bacteria, involving several pathways such as the interaction of the silver ions with thiol groups, which induces inactivation of some enzymes, the losses of replication ability of DNA or the cell membrane alteration.[26-28] Due to their features, AgNPs have been revealed an efficient agent towards multidrug-resistant bacteria.[29]

Nowadays AgNPs started to being used in commercial products so there is the risk of their leaking and consequent negative effects on the environmental and human health.[30-32] An alternative could be the anchoring of the AgNPs onto the carbon platform, which reduces the risk of aggregation[33-35] and might avoid any NPs leakage.

Moreover, the antimicrobial properties of Graphene[36,37] and that of the AgNPs could be merged into a complex hybrid system, showing enhanced synergistic antimicrobial effects than the single moiety or their blend.[38] So, it has been proved as a potential powerful antibacterial tool for the future.

In our knowledge, a universal polymer coating that could be used independently from the substrate and exhibiting high anti-bacterial properties (such as the organic substances) has not been found yet.

This chapter concerns the development of a graphene-based hybrid system as a potential universal antimicrobial coating, suitable for different surfaces. Since the compatibility between the coating layer and the substrate is based on their chemical nature, the aim is to produce a suitable platform easily adaptable for a specific substrate by only changing the polymer of the hybrid system. Moreover, the graphene moiety covalently bound to the polymer will act as an antimicrobial agent itself, but also as a platform to bind a well-known antimicrobial agent, such as silver nanoparticles. In order to respect the green-chemistry principle, this work is also focused on the development of a green strategy towards the synthesis of this nano-system.

The following paragraphs describe step-by-step the proposed new approach to obtain the targeted nanohybrid system.

Firstly, the reduction of the graphene oxide by means of a microwave-assisted method was approached and compared with the hydrazine-mediated one (paragraph 5.1).

Then, in order to improve the adhesiveness of the nanosystem with an ideal polymer surface or matrix, the GO platform esterification with Poly-Vinyl Alcohol (used as a model) was performed (paragraph 5.2).

Finally, the parts that compose the antibacterial nanohybrid system were assembled (paragraph 5.3) through a one-pot reaction, employing a microwave-assisted method to perform the simultaneous reduction of silver nanoparticles and GO. The nanohybrid system so obtained, called PVA@GO-Ag, was characterized by means of UV-vis spectroscopy, Thermal analysis, SEM-EDX, AFM and HR-TEM microscopies, and Differential Light Scattering technique. Finally, preliminary biological tests have been performed as a proof of concept for antibacterial activity.

It is noteworthy to underline that, in order to guarantee the possibility to choose the polymer that better matches with the target substrate, the GO polymer functionalization exposed in this section was performed by means of a reaction suitable for several polymers. Thus, the possibility to interchange the polymer moiety bound to the antibacterial one paves the way to a universal antimicrobial system. This new Nano-Hybrid system containing Polymer, Graphene and Silver Nanoparticles has been named NanoHy-GPS (Figure 5.1).

The PVA@GO-Ag represents the first prototype of the NanoHy-GPS species.

The NanoHy-GPS is conceptually suitable to be blended within the polymer used in the production of invasive biomedical devices. Moreover, with the aim to replace the commonly used antibacterial agents, it could be also sprayed or applied by dipping on any polymer-based surfaces already produced. Such features candidate NanoHy-GPS also as an antibacterial agent of common use objects.

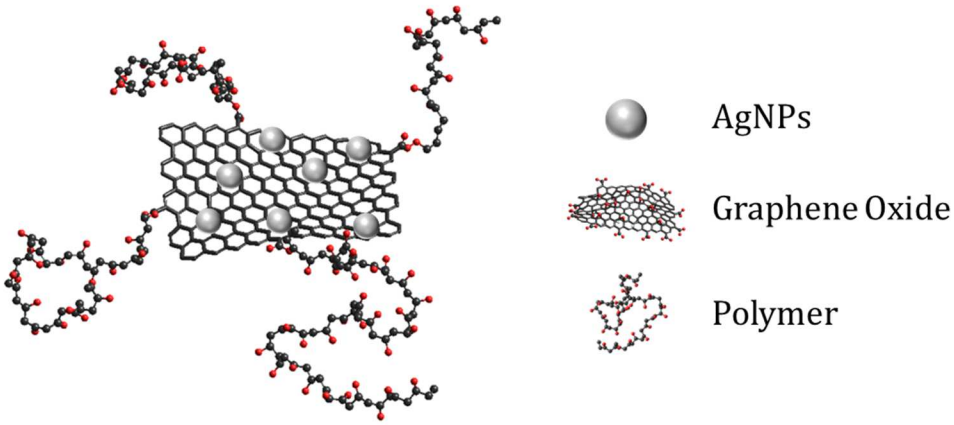

Figure 5.1 Simplified scheme of the NanoHy-GPS.

The idea of a nanohybrid multifunctional system (NanoHy-GPS) able to provide safer antimicrobial surfaces has been awarded as "Best Solution" during the 2019 EIT Health – Translational Fellowship Program, hosted by the Oxford University. An independent jury has awarded the concept designed on the basis of the market need to replace the common toxic antimicrobial agents. They have recognised the innovative nanotechnology approach described in Chapter 5, also positively considering the economic impact of the nanohybrid system.

A part of the research work here exposed resulted in a paper entitled "Polymer-Based Graphene Derivatives and Microwave-Assisted Silver Nanoparticles Decoration as a Potential Antibacterial Agent", published in *Nanomaterials* 2020, 10(11), 2269 (DOI: 10.3390/nano10112269).

5.1 An easy and quick way to Graphene Oxide reduction

Introduction

The impressive electronic and mechanical properties of graphene make it very interesting for the development of advanced materials. Nevertheless, the interest in Graphene has faced the challenge of large scale production, as mentioned in the previous chapters. Indeed, there is not any mechanical method to produce a bulk amount of graphene.[39]

To overcome this issue, the most common pathway is to produce Graphene Oxide by Graphite oxidation, then reduce the Graphene Oxide (GO). The reduction aims to increase the C/O atomic ratio, and to restore the sp^2 conjugation of the carbon platform, making the reduced GO (rGO) chemical-physical properties again similar to the one of pristine graphene. Nevertheless, the obtained rGO shows electrical and chemical properties similar but worse than that of the pristine graphene, due to the residual presence of some GO structural defects such as residual oxygen functionalities or holes within the platform which reduce the area of the sp^2 restored domains.

Despite these drawbacks, the GO reduction is the only method that assures large scale production of graphene-like material and gives also the possibility to covalently functionalize the carbon platform by exploiting the oxygen GO functionalities, before or after the reduction occurs.[40]

Several methods of GO reduction were developed during the years, by using different chemical reducing agents such as hydrazine,[41-43] vitamin C,[44-46] sodium borohydride,[47] lithium aluminum hydride.[48] Also other methods without involving chemical reducing agents were developed, such as thermal,[49] photothermal,[50] solvo- and hydro-thermal,[51-53] photochemical,[54,55] and electrochemical reduction.[56,57] All the methods, which differ in the simplicity of execution, also differ from each other in terms of the extent of the recovered conjugated network and amount of residual oxygen-containing groups: this peculiarity makes the final rGO very different according to the production method.

One of the main risks of the GO reduction processes is that, during the reduction, the Van der Waals interactions could induce the irreversible aggregation of the rGO sheets, increasing the difficulty of any further operation on the material.[58] Since the graphene properties are related to the single sheet, it is important to obtain stable suspension of rGO sheets without aggregation: indeed, the use of stabilizing agents is considered in some methods.[59-61]

In order to pursue the rGO structural characterization, several techniques could be used. Since the reduction phenomenon influences both the oxygen content and the hybridization of the platform, it is a tough point to define the so-obtained reduction degree. Through elemental analysis and/or XPS measurements, the different oxygen content of rGO compared to GO is detected as an increase of the C/O elemental ratio. Changes between GO and rGO are observed also in their FT-IR spectra, where the stretching absorption bands of the oxygenated species show a decrease in intensity after the reduction.

The reduction also changes the thermal stability of the material: the GO exhibits typical weight losses due to the oxygenated moieties, which are absent in reduced samples.[42] Besides this evidence, the recovering of the sp^2 structure also determines the decrease of the electrical resistance of the material, which, in the best-reported case, remains two orders of magnitude higher than that of the graphene.[62]

In this context, Raman spectroscopy could provide clearer pictures of the GO and rGO structures.[63] In fact, the presence of structural defects and the different content of oxygenated moieties modify the optical phonon dispersions of the carbon lattice, resulting in a different intensity ratio between the D band (~1350 cm^{-1}, attributed to six atom rings breathing modes, thus to defective regions) and the G band (~1580 cm^{-1}, attributed to sp^2 C-C high frequency phonon, thus representing defect-free graphene regions).[64,65] Since the phonon mode which produces the D peak is activated by the presence of a structural defect,[65] the decrease of the so-called I_D/I_G ratio suggests the restoration of the

graphene structure, giving informations about the oxidation degree and structural integrity simoultaneously.

Among the different GO reduction methods, the hydrazine reduction is the oldest chemical method used;[66] subsequently, the method was better investigated and developed as one of the first able to produce thin graphene-like sheets.

The hydrazine reactivity towards water is negligible with respect to other strong reducing agents, which makes it the most diffused reactant to reduce water GO dispersions. Moreover, the apparatus and the conditions needed to perceive the reduction are not complicated, so it represents a cheap and easy reduction pathway.[67] Nevertheless, hydrazine is toxic and explosive, so it represents a potential risk in industrial processes.[68]

On the other hand, microwave irradiation is a source able to heat substances homogeneously and quickly. It was already used to synthesize nanomaterials such as metals and metal-oxides without the need for extreme reaction conditions.[69-71]

In the graphene field, microwave irradiation was also used to obtain the reduction of GO, by treating powder in a microwave oven.[72] Zhu et al. found that this method produces a rGO with a lower I_D/I_G ratio and a higher conductivity if compared with the classic hydrazine mediated reduction, which confirms a better conjugation recovery due to this procedure. Anyway, the microwave-assisted procedure is potentially dangerous, because the loss of oxygen moieties is impetuous, characterized by violent fuming and material expansion (sparks and flames).

Since the reduction of GO modifies the properties of the material, which turns from hydrophilic to hydrophobic and also induces the aggregation as before mentioned, the use of a solvent during the reduction could be helpful to prevent aggregation phenomena.[43,73]

Below will be discussed the development of a versatile and quick way to obtain rGO, and suitable for polymer-functionalized GO as well. A chemical reduction method based on a microwave-assisted approach was developed and compared with the classic hydrazine mediated reduction. The two obtained products were characterized by means of FT-IR and Raman spectroscopy, thermal-gravimetrical analysis (TGA), and qualitatively compared.

Materials and Methods

All the solvents and reactants mentioned in this chapter were purchased from Sigma-Aldrich. Graphene oxide (GO) water solution (4.5 g/L), was purchased from Nanesa s.r.l.

Hydrazine mediated chemical reduction

The chemical reduction of GO was performed using a slightly modified Stankovich et al.[42] method. To obtain a GO diluted solution, 6.7 mL of a GO aqueous solution (4.5 g/L) was diluted up to 30 mL with water (LC-MS grade). The obtained GO water dispersion (1 g/L) was put in a 100 mL round-bottomed flask. Then, hydrazine monohydrate (300 µL) was added. The flask was immersed into an oil bath at 110°C, keeping the reaction at reflux for 24 hours. The mixture was cooled and dried employing a rotavap. The solid product, named rGOclassic, was washed copiously with methanol and dried in vacuum oven (50°C, 12 hrs).

Microwave-assisted reduction

A GO solution (0,5 g/L) was prepared by diluting 110 µL of GO aqueous solution (4.5 g/L) up to 1 mL with water (LC-MS grade) into a 10 mL pressure-resistant vessel; then, dimethyl formamide (5 mL) was added.

The mixture was sonicated (2 minutes), and then the vessel was capped and put into the Microwave reactor vessel holder. The reaction was conducted at a fixed power of 300 W for two minutes, cooling the system by means of air flux. Then, the mixture containing a dark solid precipitate was cooled and diluted in methanol (20 mL), and the dark precipitate was separated by centrifugation, copiously washed with ethyl ether, and dried in vacuum oven (80 °C, 12 hrs).

Results

A microwave-assisted reaction which assures an appreciable reduction degree of the GO platform was set-up by optimizing the reaction conditions. The reduction degree has been checked through FT-IR spectroscopy, until a plateau of the decrease of the carboxylic signal intensity was reached (data not shown for brevity).

Then, the product obtained from the microwave-assisted reaction (called rGOmw) was characterized and compared with the product obtained from the typical hydrazine mediated reduction reaction (called rGOclassic).

In general, the GO oxidation degree is due to a certain amount of hydroxyl, epoxides, and carboxylic acid groups. These are well evidenced by utilizing FT-IR analysis. As reported in Figure 5.2, GO sample (black line) shows signals at 3400 cm^{-1} (O-H stretching), 1729 cm^{-1} (C=O stretching), 1621 cm^{-1} (O-H bending overlapped with C=C stretching),[74] 1380 cm^{-1} (O-H stretching), 1226 cm^{-1} (C-O-C asymmetric stretching) and 1055 cm^{-1} (C-O-C symmetric stretching).[75]

The rGOmw shows an FT-IR spectrum (Figure 5.2, red continuous line) different than the GO, reasonably attributable to its reduction. Indeed, the C=O stretching signal (1729 cm^{-1}) was almost faded away, and a new band at 1560 cm^{-1} appears, attributable to the skeletal vibration of graphene.[74] The rGOclassic (Figure 5.2, blue continuous line) shows the reduction of the C=O stretching signal (1729 cm^{-1}) but preserves the C-OH bending at 1634 cm^{-1}. As the rGOmw, the skeletal vibration of graphene is revealed as a new band at 1560 cm^{-1}.[74] An intense signal in the region 960-1300 cm^{-1} attributable to O-H group stretching is evidenced as well, despite the reduction processes.

Hydrazine is widely used as a reducing agent for GO, even if the mechanism and its activity are not well understood. It is reported that it can reduce hydroxyls and epoxides better than carboxylic acid groups,[48] but further studies on model molecules evidenced that hydroxyls are not influenced by the hydrazine action.[76] In accordance to this last case, the presence of O-H groups in rGOclassic is justified.

The rGOmw FT-IR spectrum (Figure 5.2, blue line) looks very similar to the one of the rGOclassic, especially focusing on the C=O stretching signal (1729 cm^{-1}): despite the lower signal to noise ratio, it seems less reduced than the rGOclassic. The absorption signal due to the skeletal vibration of graphene is evident as well as the rGOclassic. Nevertheless, the un-assigned absorption signal in the region 960-1300 cm^{-1} is also present, broader and weaker than the rGOclassic.

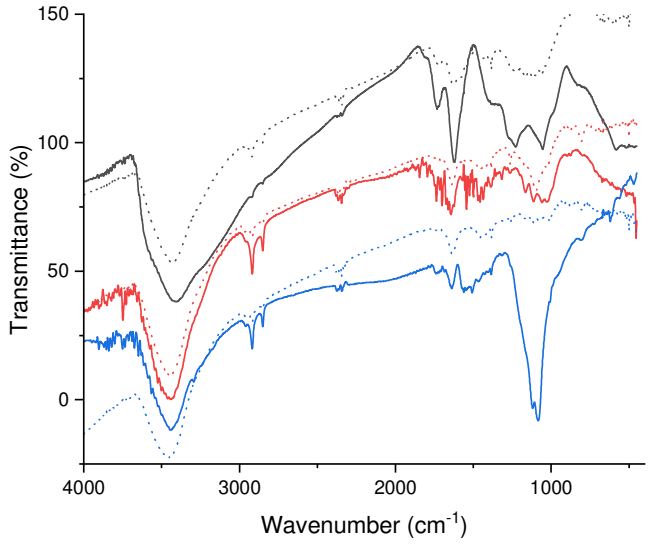

Figure 5.2 FT-IR spectra of the GO (black line), rGOclassic (red line), rGOmw (blue line), heated-GO (black dotted line), heated-rGOclassic (red dotted line) and heated-rGOmw(blue dotted line).

In order to perceive the data and be sure about the oxidation degree of the samples, TGA analyses were conducted. The oxidation state of the GO platform gives rise to typical weight losses when

heated in a nitrogen atmosphere, because of the release of the more thermal labile groups (oxygenated species). The GO (Figure 5.3, black continuous line) exhibits a first weight loss below 130°C due to the water adsorbed (13%), followed by the maximum weight loss (28%) at T_{onset}=175°C, due to the removal of labile oxygenated species.[42,77] A minor weight loss (19%) occurs at T_{onset}=540°C, leading to a residue of 28% at 800°C.

It is well-known that the reduction processes give rise to more stable products, reducing the amount of oxygen onto the graphene platform. As a result, due to the increased hydrophobicity of the rGO structure, these samples show a negligible amount of water absorbed below 130°C with respect to the GO. In particular, the rGOclassic (Figure 5.3, red continuous line) shows a first weight loss at T_{onset}=245°C (8%) and a second one at T_{onset}=586°C (26%), which ends at 800 °C (residue at 800°C = 63%).

The rGOmw (Figure 5.3, blue continuous line) shows a first weight loss at T_{onset}=334°C (15%), exhibiting higher stability than the rGOclassic (Δ=89°C), which is reasonably attributable to a different species than the oxygenated ones. By the way, another weight loss affects the rGOmw at T_{onset}=525°C (44%), which ends with a final residue of 38%.

This behaviour indicates that the residual functional groups are more stable in rGOmw than rGOclassic. Probably, these residual functional groups are different on both rGOmw and rGOclassic, due to the different reduction procedure.

On the other hand, about the attribution of the last weight loss (at about 500 °C), literature data are slightly deficient.

Nevertheless, Park et al. have already reported similar evidences in hydrazine reduced GO samples. In particular, they reported the comparison between the hydrazine mediated reduction of a completely exfoliated GO with a non-exfoliated one: the TGA trace of the exfoliated-reduced GO shows higher weight loss at about 500 °C than the one simply reduced.[41]

Since the evidence of the TGA measurements, and considering the results of Park et al., the microwave-assisted reduction probably resulted in a better exfoliation of rGOmw than that of rGOclassic also inducing the formation of a higher amount of hydroxyls groups onto the rGOmw platelets and/or amine species due to the microwave-assisted reaction process.

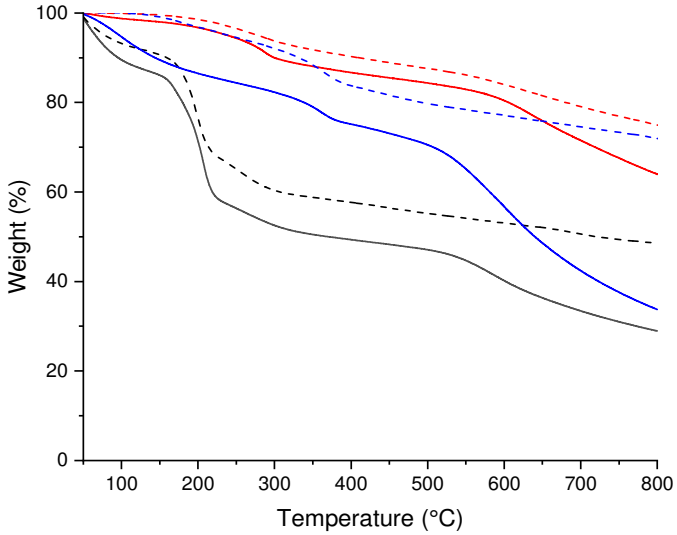

Figure 5.3 TGA traces related to GO (black line), rGOclassic (red line), rGOmw (green line), heatedGO (black dashed line), heated-rGOclassic (red dashed line) and heated-rGOmw (blue dashed line), nitrogen atmosphere.

To shed light on the structural differences between rGOmw and rGOclassic, evidenced by the degradation step at T>500°C, the samples were heated at 100°C in a nitrogen atmosphere for 30 minutes, obtaining the so-called heated-GO, heated-rGOmw and heated-rGOclassic, respectively.

As a result, the heated-GO exhibited a decrease of the intensity of the FT-IR signals in the wavenumber range 1400-900 cm^{-1}, which could be attributed to C-O stretching and O-H stretching,[78] and also the disappearance of the weight loss at T_{onset}=540°C in its TGA trace (Figure 5.3 dashed black line).

The heated rGOclassic shows a flattening of the alcohols FT-IR signals (Figure 5.2 red dashed line). Moreover, its TGA trace showed the absence of any clear degradation step, as a confirm of the absence of any oxygenated species residue. Since the epoxides are well reduced by hydrazine, and the temperature at which the weight loss occurred was too high for hydroxyl groups, some other mechanisms might be involved to produce the weight loss at T>500°C.

Interestingly, in contrast with the heated-rGOclassic, the heated-rGOmw still shows FT-IR signals centered at about 1100 cm^{-1}attributable not only to alcohols stretching, but also to C-N stretching of amine species (Figure 5.2 blue dashed line). Furthermore, the TGA trace of the heated rGOmw shown the total disappearance of the weight loss at 525°C, while the less intense one which starts at 334 °C is still present. Thus, confirming that the heated-rGOmw exhibits stable amine species which are loss at about 334 °C and are not influenced by the thermal treatment in nitrogen.

From the analysis of the TGA and FT-IR data of GO, rGOmw and rGOclassic and the respective heated counterparts, a hypothesis regarding the presence of the high-temperature weight loss (T_{onset}

> 500°C) has been proposed. The presence of hydroxyls groups onto GO and rGO samples enhance the hydrophilicity of the carbon platform, which adsorbs water (which could increase the intensity of the hydroxyl stretching signals in the FT-IR spectra).

When the samples are subjected to TGA analysis (in nitrogen atmosphere), at high temperature, the hydration of the double bonds with the physisorbed water must be also considered, besides other reactions involving water. These side-reactions increase hydroxyl groups and structural defects amount. Subsequently, such structural modifications result in the degradative step evidenced at T_{onset} > 500°C.

The presence of oxygenated species on reduced GO samples is not unexpected. Noteworthy, the reduction of the GO is known to partially eliminate the oxygenated species. Especially in the case of hydrazine mediated processes, it is reported that it can reduce the epoxide and carboxylic acid content, but it is not so efficient on hydroxyls groups.[76]

The reduction mechanism of the graphene oxide is not well understood yet. One of the proposed mechanisms for the hydrazine mediated epoxides reduction[42] process is reported in Figure 5.4.

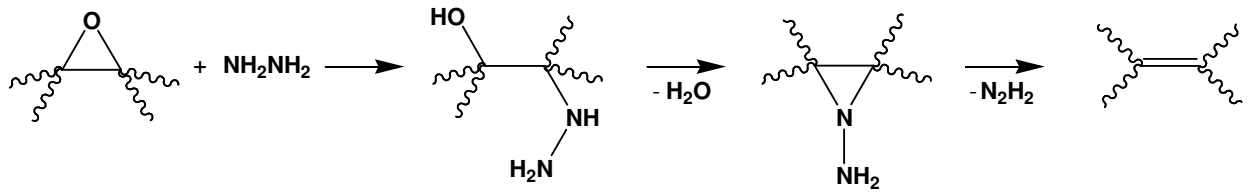

Figure 5.4 Reduction mechanism operated by hydrazine

In order to analyze the structural differences concerning the graphene platform, and investigate on the conjugation recovery due to the reduction processes, Raman spectroscopy analyses were conducted. It is a powerful technique to study the carbon lattices:[79] in particular, double- and conjugated carbon bonds give rise to high Raman intensity.[80]

The typical spectrum of graphene is characterized by the G band, at 1582 cm^{-1}, and the 2D or G' at 2700 cm^{-1}. When defects appear in the structure, or at its edges, also a new band called disordered-induced D band at about 1350 cm^{-1} appears.[81]

In particular, the G band is produced by a first-order Raman scattering process: is due to an in-plane vibration of sp^2 hybridized carbon atoms, and is a doubly degenerate phonon mode with an E_{2g} symmetry, located at the center of the Brillouin zone. The 2D band is originated by a two-phonon double resonance Raman process. Instead, the D band is attributable to a process which involves a phonon (one of the doubly degenerate ones) and a defect.[82]

The GO Raman spectrum (Figure 5.5, black line), shows an I_D/I_G ratio of 1.04, where D band is centered at 1353 cm^{-1} and G band at 1603 cm^{-1}.

The reduction processes produced an increase of the I_D/I_G intensity ratio up to 1.42 and 1.07 related to rGOclassic (Figure 5.5, red line) and rGOmw (Figure 5.5, green line), respectively. In principle, the reduction of GO must reduce the I_D/I_G intensity ratio, because the recovery of the conjugation must increase the intensity of the G peak.

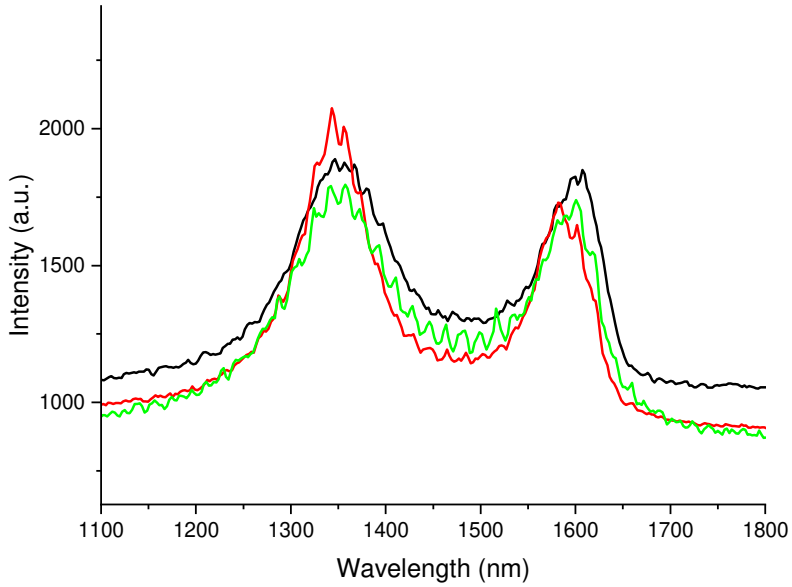

Figure 5.5 Raman spectra of GO (black), rGOclassic (red) and rGOmw (green).

By the way, the increased I_D/I_G intensity ratio after the reduction processes used in this thesis is not contradictory. According to literature[42], these data suggest that the reduction increases the number of sp^2 domains characterized by small size; so, the boundary regions which connect the graphitic domains are defective and give rise to the D band higher intensity than the starting GO.

Luo et al. have shown that some procedures are suitable to reduce the number of defects of the GO platform during the reduction occurring, due to repairing processes.[68] Anyway, here could be proposed that the MW-assisted reduction preserves the I_D/I_G ratio better than hydrazine-mediated reduction.

5.2 A versatile grafting-to approach for the GO platform esterification

Introduction

In the field of materials science, the polymer composites have gained a primary role, thanks to their unique electric,[83] thermal,[84,85] optical[86] and mechanical[83,85] properties. Moreover, by changing the filler and/or the amount loaded within the polymer matrix, these properties can be finely tuned. For these reasons, the polymer composites have a key role in the production of advanced materials covering a broad range of topics. Since the peculiar properties of the composites are primarily due to area to volume ratio of the filler, going from macro- to nano-scale additives definitely represented a milestone in materials science and nanotechnology.

The first noteworthy nanocomposite for both academy and industries was a Nylon-6 filled with montmorillonite, produced by researchers from Toyota Motor Corporation,[87] which exhibited enhanced mechanical properties. Starting from this memorable material, several types of nanofiller were used to produce polymer nanocomposites.[88,89]

Among all the available fillers for polymer matrices, the carbonaceous additives are widely used, such as carbon nanotubes, graphite, graphene, and also graphene oxide.[85] Overlooking the characteristics of these nanocomposites, it is noteworthy to say that from a mechanical point of view the simple intercalation of polymers within these fillers is a critical point. It has been demonstrated the fundamental role of the interfacial interactions between the graphene platform and the polymer matrix in achieving the optimum stress transfer from the matrix to the filler.[90] Indeed, the appearance of fractures within the polymer-graphene nanocomposites is related to the failure of the graphene-polymer interface.[91]

Moreover, the homogeneity of the mixing between the polymer matrix and the graphene is also a key point to optimize the external load transfer from the polymer to the nanofiller. In order to stabilize the dispersion of the GO into the polymer matrix, and to improve their interface interactions, a useful approach is to graft onto the GO platform the polymer of interest.[90]

The strategies to date adopted to link covalently polymers to the graphene platform could be collected in two categories: the *grafting-from* methods, which use the graphene as the base on which the polymerization is initiated,[92] and the *grafting-to* methods, which link an already synthesized polymer onto the graphene platform.[93]

Since it is not widely feasible to immobilize on the GO platform the initiator for the polymerization of specific polymers, the *grafting-from* method is not universally applicable. For this reason, the *grafting-to* method is the strategy that allows us to bind on the GO a plethora of polymers. To use this strategy, the Graphene moiety must present functional groups suitable for the covalent binding

with an appropriate functional group of the polymer chosen. Exploiting its carboxylic acid groups, the epoxides and the hydroxyls groups, the GO has been covalently bond several polymer species such as PVC,[94] PEG,[95] PNIPAM,[96] Poly-L-Lysine,[97] PMMA,[98] PS,[99] and Nylon.[100]

Polyvinyl-alcohol (PVA) is a water-soluble polymer, but it is resistant to the most common organic solvents. It is derived from the hydrolysis of polyvinyl-acetate, and its water solubility and the crystallization degree depends on the degree of hydroxylation. Moreover, thanks to its low environmental impact and its biocompatibility, it is widely used in textile industries, food packaging, paper industry, and medical devices. In particular, it is useful as a biomaterial, because it exhibits bioadhesive characteristics, easiness of processing and it is non-toxic and non-carcinogenic.[101] Since these characteristics, it has been investigated for artificial articular cartilage,[102-105] tissue-engineered scaffolds, soft contact lenses,[106] and drug-delivery. It is also known to be used to fabricate membranes, fabrics, and coatings.

It is commonly used as a model polymer matrix for the developing of nanocomposites and to test their mechanical properties.[90]

In this section, the covalent functionalization of the Graphene Oxide platform with PVA was performed (Figure 5.6).

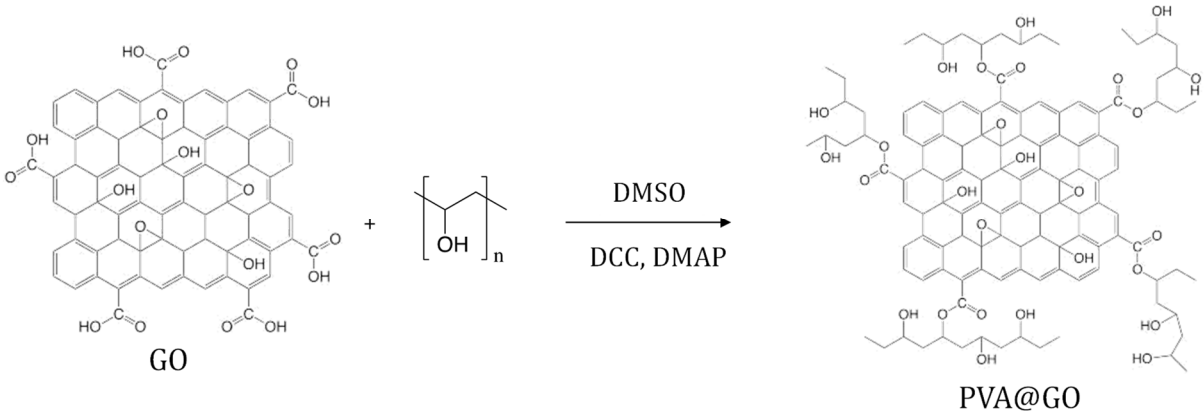

Figure 5.6 Scheme of the PVA@GO synthesis.

The hydroxyls groups of the PVA were exploited to esterify the carboxylic acid of the GO platform by means of Steglich esterification,[107] which involves N,N'-Dicyclohexylcarbodiimide (DCC) and 4-Dimethylaminopyridine (DMAP) as catalysts. The resulting material has been characterized employing ^{1}H-NMR and COSY techniques, and Thermogravimetric analysis. The aim was to use it as an intermediate material to furtherly develop the NanoHy-GPS hybrid system.

Materials and Methods

Natural graphite powder (diameter 5–10 μm, thickness 4–20 nm, layers < 30, purity > 99.5 wt.%), PVA (Mw 200000 Da), N,N'-Dicyclohexylcarbodiimide (DCC), 4-Dimethylaminopyridine (DMAP) and solvents were purchased from Sigma Aldrich.

Graphene oxide (GO) was prepared by oxidizing natural graphite powders using Hummers method[108] and successive exfoliation of graphite oxide by ultrasonication.[109] Briefly, natural graphite (2 g) was added to sulfuric acid (350 mL) cooled at 0°C. To avoid agglomeration and homogenize the dispersion, the mixture was vigorously stirred. Then, sodium nitrate (1g) and potassium permanganate (8 g) were slowly added to the reaction mixture. The temperature was then raised up to 40°C and the mixture was stirred for 1h. Thereafter, deionized water (250 mL) was slowly added into the solution, determining an immediate increase of temperature up to 70°C. The temperature was raised up to 98°C and the reaction stirred for 30 min. Finally, 52 mL of H_2O_2 (30%) were poured into the reaction mixture, resulting in the formation of bright yellow suspension. The graphite oxide was separated by vacuum filtration and washed with HCl (4%) and water to reach a neutral pH. The product was dried to obtain a brown powder (1.8 g). Exfoliation of graphite oxide was carried out by ultrasonication (8h) of the aqueous suspension graphite oxide (500 mg of graphite oxide in 35 mL of deionized water). The obtained homogeneous dark brown dispersion was diluted with deionized water and centrifuged at 10000 rpm for 12 min; then, the residue was eliminated, and the supernatant containing the graphene oxide sheets (GO) was recovered.

The esterification was conducted through a slightly modified method compared to that developed by Salavagione et al.[110] Briefly, 20 mg of GO and 200 mg of PVA were dissolved in DMSO (10 mL) at 70°C under stirring in N_2 atmosphere. After 24 hours, the solution was cooled to room temperature. Then, DCC (926 mg, 4.5 mmol) and DMAP (69 mg, 0.56 mmol) previously solubilized in DMSO (10 mL) in N_2 atmosphere, were added to the PVA solution. The reaction was kept under stirring in N_2 atmosphere for 3 days; after that, the mixture was precipitated in methanol (50 mL). The solution was centrifuged (9000 rpm, 20 minutes) and the precipitate was dissolved in 70 mL hot water (70 °C). So, the water solution was concentrated by means of a rotavap, and then coagulated in methanol and centrifuged (9000 rpm, 20 min). The precipitate was dried for 24 hours in the oven (50 °C) under vacuum.

Structural and chemical-physical characterizations

The formation of the ester bond between the GO acid groups and the PVA hydroxyl ones was verified through NMR mono- and bi-dimensional techniques.

The ^{1}H-NMR spectrum of the PVA@GO (500 MHz, D_2O), shown in Figure 5.7, reveals the signals typical of the PVA, with methylene protons (*b*) in the range 1.15-1.97 ppm, and the C-H attached to the alcohol (*a*) in the range 3.57-4.17 ppm. The singlet at 3.39 is due to the methanol residual. Noteworthy, a small signal is revealed at 5.05 ppm, which is attributable to the protons vicinal to the ester groups (*a'*): indeed, the ester formation will shift the signal to higher ppm value, due to the de-shielding effect of the oxygen atoms. To further confirm this signal attribution, a COSY spectrum was acquired (Figure 5.8). The analysis confirms the correlation between protons *a-b* (Figure 5.8, red circle), but is evident the correlation *a'-b* as well (Figure 5.8, blue circle), thus confirming that the esterification reaction has occurred.

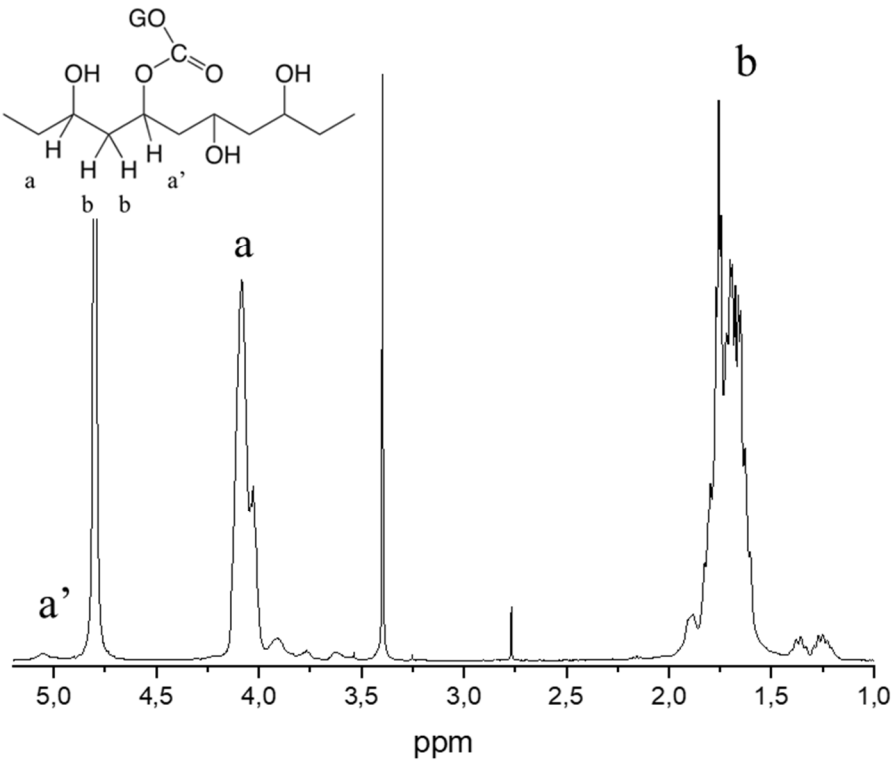

Figure 5.7 ^{1}H-NMR spectrum of PVA@GO (D_2O, 500 MHz).

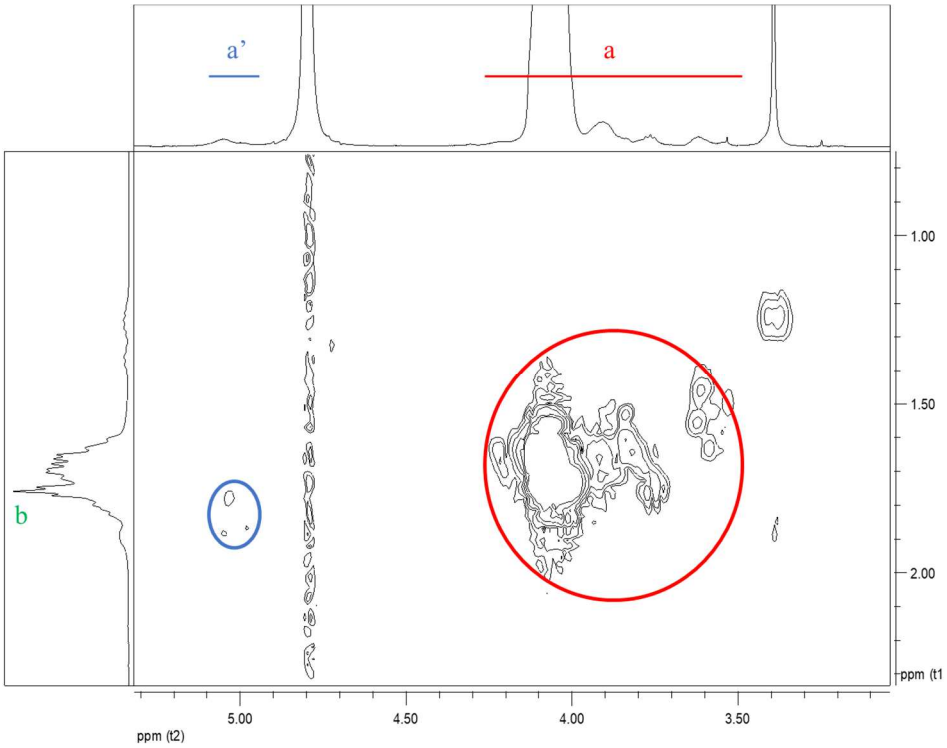

Figure 5.8 COSY-NMR spectrum of PVA@GO (D_2O, 500 MHz). The cross-correlations signals are highlighted with a red circle (a-b) and blue circle (a'-b).

The GO dispersion in water is constituted of a wide distribution in size, due to the production processes. In particular, the GO used in this section shows two main size distributions, as indicated by DLS measurements (Figure 5.9, black dashed line). Pure PVA in aqueous solution shows two size distributions (grey line) centered at hydrodynamic radius values of 6 nm, and 130 nm, respectively. The functionalization of GO with PVA resulted in three main size distribution, (black line) centered at 5 nm and 70 nm of hydrodynamic radius: those are very similar to that of the pure PVA, even though having different intensities. Such evidence could be due to the inter-chains entanglement of PVA, which could also be favoured in PVA@GO due to the close contact forced by the mutual proximity of the covalent linking sites onto the GO platform. Moreover, a multi-linkage of GO with a single PVA chain cannot be neglected.

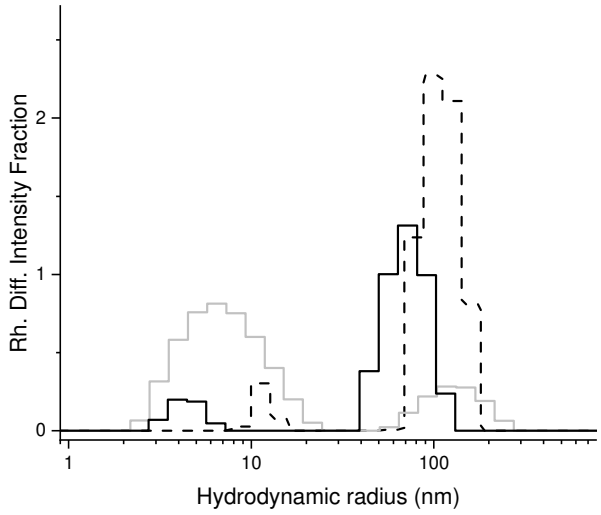

Figure 5.9 DLS size distribution of PVA (grey line), GO (black dashed line), and PVA@GO (black line) water solutions (12.5 μg/mL).

The polymer functionalization of GO influences its thermal stability, as evidenced by TGA. The pure GO (Figure 5.10, blue line) shows a water loss below 110°C and a degradation step at T_{onset} = 193°C. The pure PVA (Figure 5.10, red line) losses the bulk water below 150°C, shows the first degradation step at T_{onset} = 235°C, attributed to the elimination of the hydroxyl side-groups and chain scission reactions, and a second degradation step at T_{onset} = 410°C, due to the breakdown of the polymer backbone.[111,112]

As an effect of the covalent functionalization, the nanocomposite (Figure 5.10, black line) shows the losses of the bulk water in the same temperature range than that of the PVA: indeed, the main responsible of the water content is the hydrophilicity of the PVA chains. Nevertheless, the main degradative step has a T_{onset} = 266°C, which is higher than that of both components of the PVA@GO. These results are similar to that obtained by Salavagione et al., and are attributed to the aspect ratio differences between the GO platforms and the PVA linked to them.[110] The GO platform could inhibit the side groups elimination from PVA chains due to several reasons: GO acts as a scavenger for the free-radicals formed during PVA decomposition;[113] it interacts and stabilizes the PVA hydroxyl groups through hydrogen bonding with GO oxygenated groups; finally, GO presence creates tortuous paths in the bulky material, thus preventing the gas release.[114]

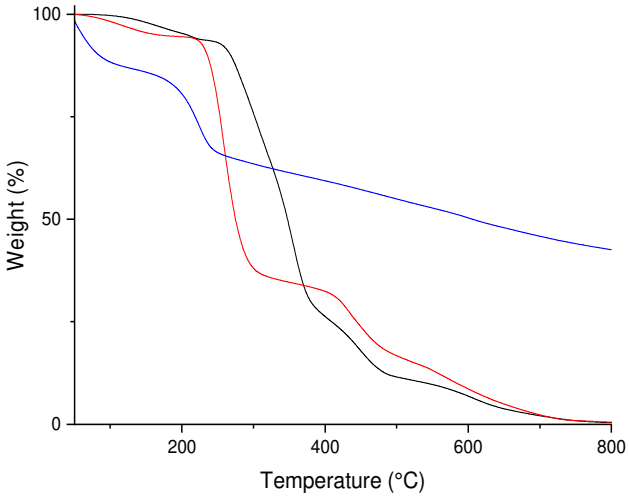

Figure 5.10 TGA traces of PVA (red line), GO (blue line), and PVA@GO (black line), nitrogen atmosphere.

5.3 One-pot method for AgNPs decoration, GO reduction and final assembly of the NanoHybrid Graphene-Polymer-Silver system

Introduction

In the field of nanotechnology, metal nanoparticles (NPs) represent a wide class of materials that are characterized by a diameter less than 100 nm size.[115] Since the interest in the physicochemical properties of such nanoscaled materials, during the last decade they have gained importance in the fields of catalysis, electronics, biotechnology and environmental remediation.[116-120]

Thanks to their nano-size, these metal NPs exhibit surface plasmon resonance which is responsible of their UV-vis absorption profile.[121] Indeed, the resonance between the collective oscillation of the conduction band electrons of the metal and the one of the incident light electric field generates a strong oscillation of the surface electrons, namely localized surface plasmon resonance (LSPR).[121] Moreover, the LSPR signal is influenced by NPs size, shape, chemical surroundings and interparticle interactions.[122]

Among all the noble metals studied, Silver is the most important metal in plasmonics,[123,124] and represents an efficient antimicrobial agent. Because of the improper use of antibiotics,[125] the bacteria have developed response mechanisms towards drugs (antimicrobial resistance)[126,127] which makes them resistant to the common therapies.[128] In this context, Silver Nanoparticles (AgNPs) resulted particularly effective towards these resistant bacteria, becoming a promising antimicrobial agent suitable for modern therapies.[29,116]

Traditionally, AgNPs are synthesized through the reduction of silver nitrate through reducing agents, such as sodium borohydride.[129] More recently, the green approach leads to the selection of more sustainable reductant and solvent medium, but also an environmentally benign and non-toxic counterpart to stabilize the NPs.[130,131] Since this need, different methods using water as a solvent and sustainable reducing and capping agents have been proposed. As examples of green reactants, ascorbic acid or β-D-glucose have been reported as reducing agents and starch or sodium citrate as capping agents.[130,132] Noteworthy, also plants extracts have been recently used to replace the common reducing agents such as leaf extract from green tea plants, and also coffee.[133-135]

In this landscape, Graphene and Graphene Oxide could act as a platform for the AgNPs, which could nucleate onto the GO oxygen functional groups. Moreover, anchoring the AgNPs onto GO surface would reduce the NPs aggregation[33-35] and might avoid their leakage in the environment.

To get an efficient and long-lasting antimicrobial coating, it is fundamental to obtain a polymer thin-film firmly attached to the substrate, otherwise, the coating could stick insufficiently, thus undergoing mechanical deterioration and subsequent leakage. The easier solution is to choose a coating made up

of the same polymer as the substrate. Due to the chemical-physical nature of GO, its suitable polymer functionalization is the mandatory solution to obtain a mechanically stable coating.

In this section, a microwave-assisted reaction is developed to reduce AgNPs over a Poly-Vynil Alcohol functionalized GO (PVA@GO), producing the nanohybrid systems named PVA@GO-AgX (Figure 5.11). The reaction here discussed was able to contemporarily reduce AgNPs from silver nitrate and the GO platform, leading to a type of potential antimicrobial hybrid nanosystems which synergistically merge the structural properties of the polymers, the high surface area of the reduced GO and the antibacterial activity of the AgNPs, from here called NanoHybrid-Graphene Polymer Silver (NanoHy-GPS).

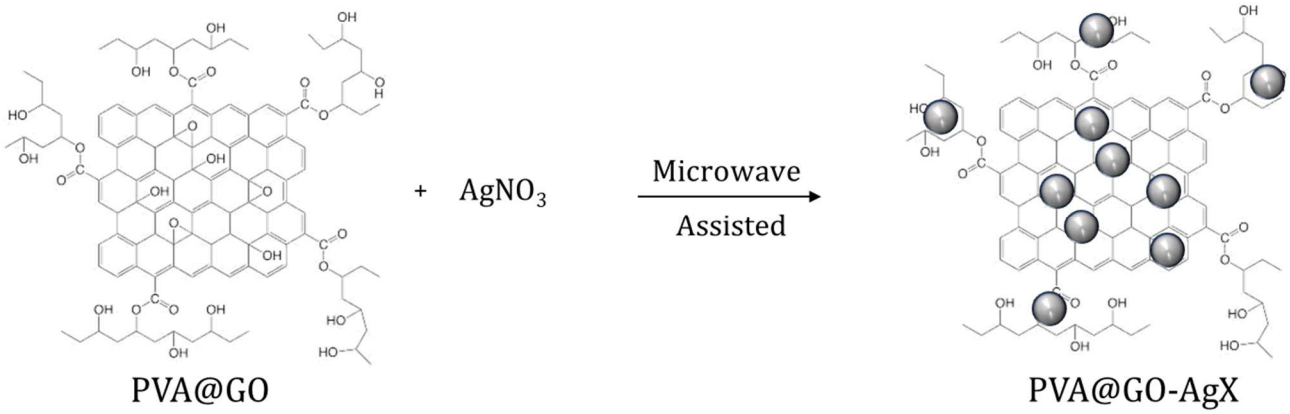

Figure 5.11 Schematic representation of PVA@GO-AgX synthesis.

The NPs reduction over the GO platform was verified using UV-vis and fluorescence spectroscopies, and SEM-EDX analyses. The hybrid system morphology was characterized through Dynamic light scattering, AFM, SEM and HR-TEM analyses.

Materials and methods

The solvents and the Silver Nitrate were purchased from Sigma Aldrich.

The reduction of Silver Nanoparticles onto the hybrid graphene-based system was performed through a microwave-assisted reaction on PVA@GO aqueous solution (1 mL, 0.5 g/L). The solution was put in a 10 mL vessel and proper amounts of $AgNO_3$ were added. Once the solution was stirred, 5 mL of DMF were added and the mixture was sonicated for 2 minutes. The vessel was capped and inserted into the microwave holder. The reaction was conducted for two minutes at a power of 300 W, cooling the system through air flux.

The total reaction mixture was diluted in methanol and concentrated using a rotary evaporator (60 °C and vacuum). Then, the mixture was precipitated in ethyl ether, the solid was separated through centrifugation (9000 rpm, 20 min, 5°C), and then dried in a vacuum oven at 50 °C overnight.
By increasing the $AgNO_3$ amount added during the synthetic procedure, three products were obtained: PVA@GO-Ag1 with 35.7 μg (0.21 μmol) of $AgNO_3$, PVA@GO-Ag2 with 0.33 mg (1.96 μmol) of $AgNO_3$ and PVA@GO-Ag3 with 3 mg (18.7 μmol) of $AgNO_3$.
For sake of comparison, employing the same microwave-assisted procedure without $AgNO_3$, samples of reduced PVA@GO (called PVA@rGO) and a sample of reduced GO (called rGO) were produced as well.

Silver Nanoparticles (AgNPs) have been synthetized through the typical reduction of silver nitrate in aqueous solution. Briefly, 750 mL of Sodium Borohydride water solution (2 mM) were prepared and left under high rpm stirring. Then, 250 mL of Silver Nitrate water solution (1 mM) were added through a dropping funnel. The reaction was left under high stirring until the end of the silver nitrate addition. In order to stabilize the suspension and have certainty about the reduction of the whole silver salt added, the mixture was stirred for additional 30 minute. The obtained AgNPs suspension, stored at 5°C, is stable for months. The LSPR signal at 394 nm of such AgNPs has been checked by UV-vis measurements.

Preliminary antibacterial tests: Bacterial population from common hand-contacted surfaces have been recovered and streaked[136] over the Plate Count Agar (PCA). In detail, sterile swabs, premoistened in Maximum Recovery Diluent (MRD), were streaked over common hand-contacted surfaces (i.e., door handles and handrails) with size 100 cm^2. In order to ensure a good capture of bacteria, the swab constantly rotated and uniformly swiped in all directions of the tested surface. Then, the microorganisms transferred to the swab were released into 10 mL of MRD, transported in the microbiology laboratory (about 5 min), and used to test the several compounds, namely, AgNPs, PVA@GO-Ag2, $AgNO_3$, and PVA@GO. Each compound (100 μL, 27 μg/mL in Ag content and/or 142 μg/mL in PVA@GO content) was previously deposited onto the PCA. Then, bacteria in MRD (100 μL) were spread on treated PCA and incubated for 24 h at 37 ◦C. Each biological experiment was performed in triplicate. As control, bacteria in MRD without any antibacterial compound was used.

Structural and chemical-physical characterizations

Through a microwave-assisted reaction, such PVA@GO nanosystem was decorated by different content of AgNPs, varying the amount of Ag salt added during the synthetic procedure. In particular, with the double aim to investigate about the Ag loading efficiency onto the PVA@GO system and to perform a thorough characterization of the nanohybrid system, three samples with increasing amount of Ag were produced, respectively PVA@GO-Ag1, PVA@GO-Ag2 and PVA@GO-Ag3 (Figure 5.12).

For a better comprehension of the nanosystem structure modifications occurred during the Microwave-assisted reaction, such a procedure was adopted also on GO and PVA@GO without adding the Ag salt (as described previously).

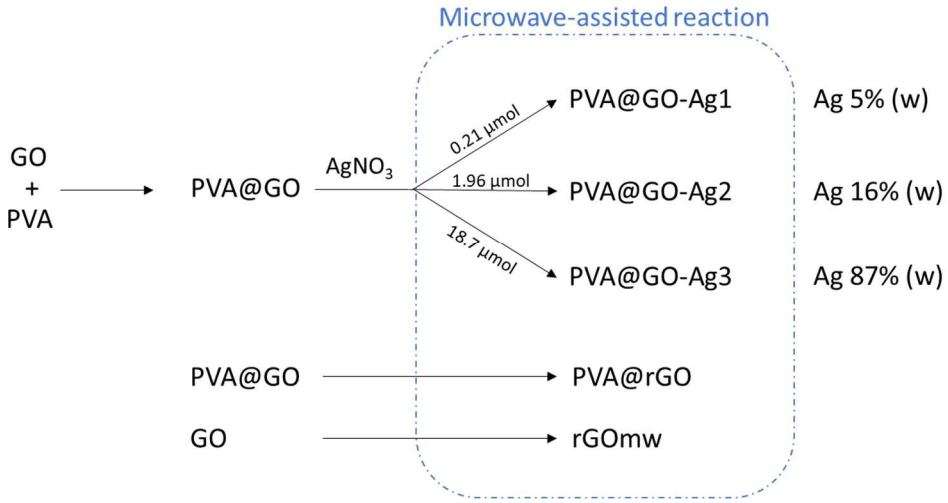

Figure 5.12 Simplified scheme of the reactions exposed in this section.

The UV-vis spectrum of PVA (0.3 g/L) shows an absorption band at 217 nm and a smaller one at 275 nm, due to the n-π* and π-π* transitions of carbonyl residual groups (Figure 5.13, grey dashed line).[137,138] Since PVA can reasonably be assumed as transparent, comparing it with a PVA@GO aqueous solution 0.3 g/L (Figure 5.13, red dashed line), it is evident a wide absorption from 800 nm to 200 nm attributable to the GO moiety. The overlapped narrow band centered at 278 nm is due to the DCC residual, that was removed opportunely during further purifications.

The PVA@rGO, due to the microwave-assisted reaction conditions shows a different slope of the absorption profile, probably attributable to reduction phenomena occurring on the GO platform.

To confirm this hypothesis, a pure GO aliquot was subjected to the microwave-assisted reaction conditions used to produce the hybrid nanosystem, to obtain the rGOmw (discussed in a previous paragraph).

The UV-vis analysis confirmed the occurrence of the GO reduction, as shown from the red-shift of the π-π* transition peak from 237 nm (GO, inset Figure 5.13 red line) to 266 nm (rGO, inset Figure 5.13, black line), together with a remarkable slope variation. Moreover, the rGOmw exhibited the increase of the absorbance in the UV-region (<230 nm), that may be attributed to a nitrogen doping of the reduced graphene platform[139] and/or to the π-π attraction between rGO platforms.[140]

A qualitative consideration about the AgNPs deposited onto the PVA@GO nanosystem could be done considering the Localized Surface Plasmon Resonance (LSPR) typical of the AgNPs. In order to use them as a blank, AgNPs were synthesised through the common sodium borohydride reduction: the UV-vis analysis of the AgNPs water solution (3.5 mg/L) shown a narrow LSPR signal centered at 394 nm (Figure 5.13, green line).

In the cases of nanohybrid systems, the different amount of $AgNO_3$ added during the synthesis, which increases from PVA@GO-Ag1 to PVA@GO-Ag3, gives rise to strong optical differences in the samples. Those differences are also visible by naked-eye, as can be checked from the digital picture shown in Figure 5.14.

By comparing through a naked-eye inspection the water solutions of PVA@GO-Ag 1,2 and 3 (Figure 5.14), it is evident the opalescence of the PVA@GO-Ag3 solution: the higher Ag amount added during the PVA@GO-Ag3 synthesis is reflected in a broad UV-vis extinction signal and a higher light scattering (Figure 5.13, cyan line).

In contrast, the PVA@GO-Ag2 water solution exhibits a transparent brownish color, and similar transparency is exhibited by the PVA@GO-Ag1 solution, despite a yellowish color. Their UV-vis spectra revealed that the PVA@GO-Ag2 shows LSPR extinction signal centered at 403 nm, while the PVA@GO-Ag1 at 420 nm, corresponding to AgNPs size of about 15 nm and 50 nm, respectively.[141] The different intensity of the LSPR extinction signal for the different samples is due to the different relative content of AgNPs, which gives rise also to the brownish and yellowish colour of their water solutions. The variation of the silver nitrate added during the synthesis of PVA@GO-Ag2 and PVA@GO-Ag1, does not modify the full width half maximum (FWHM) of the LSPR signal, which is attested to about 100 nm for both samples. As expected, the presence of the PVA@GO nanosystem influences the nucleation and the growth of the AgNPs resulting in broader LSPR bands than that of pure AgNPs (FWHM about 60 nm).

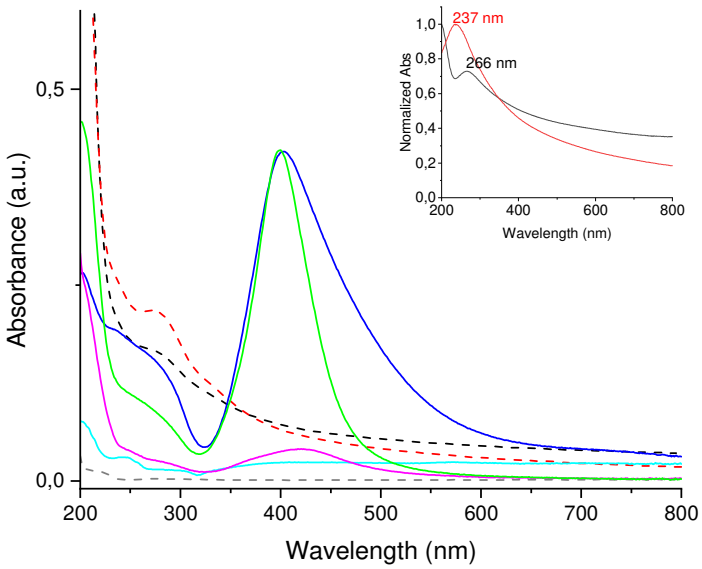

Figure 5.13 UV-vis spectra of water solution of PVA (grey dashed line), PVA@GO (red dashed line), PVA@rGO (dark dashed line), AgNPs (green line), PVA@GO-Ag1 (magenta line), PVA@GO-Ag2 (blue line), PVA@GO-Ag3 (cyan line). Inset: Normalized UV-vis spectra of GO (red line) and rGO (black line) water solution (0.3 g/L).

Figure 5.14 Digital image of water solutions (0.3 g/L) of PVA@GO-Ag1, PVA@GO-Ag2 and PVA@GO-Ag3.

The amount of Ag reduced onto the PVA@GO systems was defined by TGA analyses in air atmosphere (Figure 5.15).[35] The Ag weight (%) content of the different samples has been calculated taking into account the residue at 800°C of the PVA@GO-Ag sample subtracted by the PVA@GO one, as follows:

$$x = PVA@GOAg\ residue\ - PVA@GO\ residue$$

The calculation gives the 5% Ag content for PVA@GO-Ag1, 16% for PVA@GO-Ag2 and 87% for PVA@GO-Ag3. Moreover, by comparing the PVA@GO oxidation with the PVA@GO-Ag1 is clear that the AgNPs stabilize the first degradation step which is shifted from 217 °C for PVA@GO-Ag1, up to 227 °C for PVA@GO-Ag2 and 281 °C for PVA@GO-Ag3.

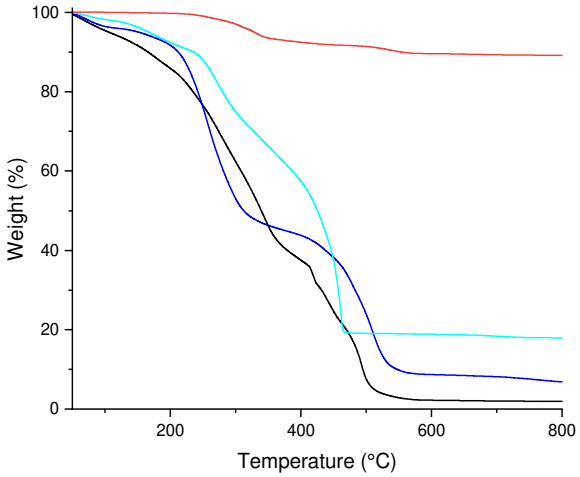

Figure 5.15 TGA thermograms of PVA@GO (black line), PVA@GO-Ag1 (blue line), PVA@GO-Ag2 (cyan line) and PVA@GO-Ag3 (red line), air atmosphere.

An accurate morphological and qualitative characterization of the hybrid nanosystems has been conducted employing SEM-EDX analysis (Figure 5.16). All the PVA@GO-Ag nanohybrid systems present similar smooth surfaces attributed to PVA@rGO backbone (Figure 5.16). The AgNPs shows spherical and quite regular morphology in all the three samples analyzed, with a distribution of agglomerates in samples PVA@GO-Ag2 and PVA@GO-Ag3. The EDX analysis confirms the nature of the nanoparticles, as evidenced by a peak at 2.98 keV attributed to Ag Kα line, and shows a strong decrease of Ag atomic percentage from PVA@GO-Ag3 to PVA@GO-Ag1.

The PVA@GO-Ag1 represents the most reliable sample to investigate about the nanohybrid system morphology, because of the lack of AgNPs agglomerates.

In fact, despite the absence of evident AgNPs in the SEM image, the related EDX spectra (Figure 5.16, C) confirms the AgNPs presence, which are well-dispersed and embedded within the PVA@rGO backbone.

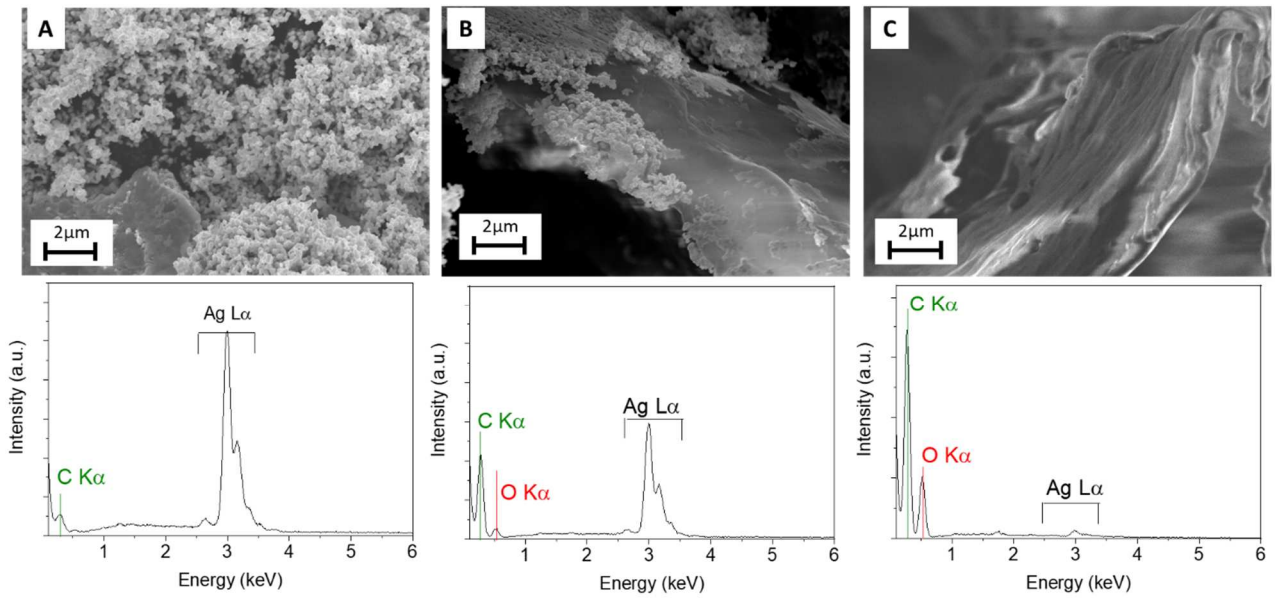

Figure 5.16 SEM images and the related EDX spectra of PVA@GO-Ag3 (A), PVA@GO-Ag2 (B) and PVA@GO-Ag1 (C).

The PVA@GO-Ag1 was also used to investigate about the nature of the nucleation sites of the NPs and about the morphology of such nanohybrid system. A higher value of Ag concentration could indeed cover the GO moiety (as evidenced by SEM analysis in Figure 5.16, A). The phase images (Figure 5.17, A and C) shown that the sample is in form of a PVA homogeneous film containing both NPs and rGO platform. The height profile calculation has revealed that the rGO moiety is basically a few layers aggregates (~50 nm, Figure 5.18), functionalized by PVA and also covered by AgNPs. Moreover, the AgNPs size distribution was ranging from few to dozens of nanometers, in accordance with the UV-vis results. The images suggest that the nucleation of the AgNPs occurs onto the GO platform, exploiting the microchemical environment of its oxygenated groups, but also within the polymer matrix, because the PVA hydroxyl groups interactions with silver surfaces influences the nucleation and growth of the AgNPs.[142]

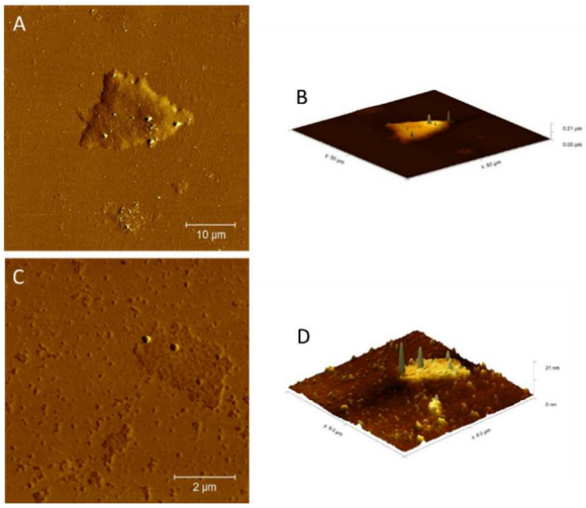

Figure 5.17 AFM Phase images 50x50 µm (A) and 8x8 µm (C) and the related 3D Height (B, D).

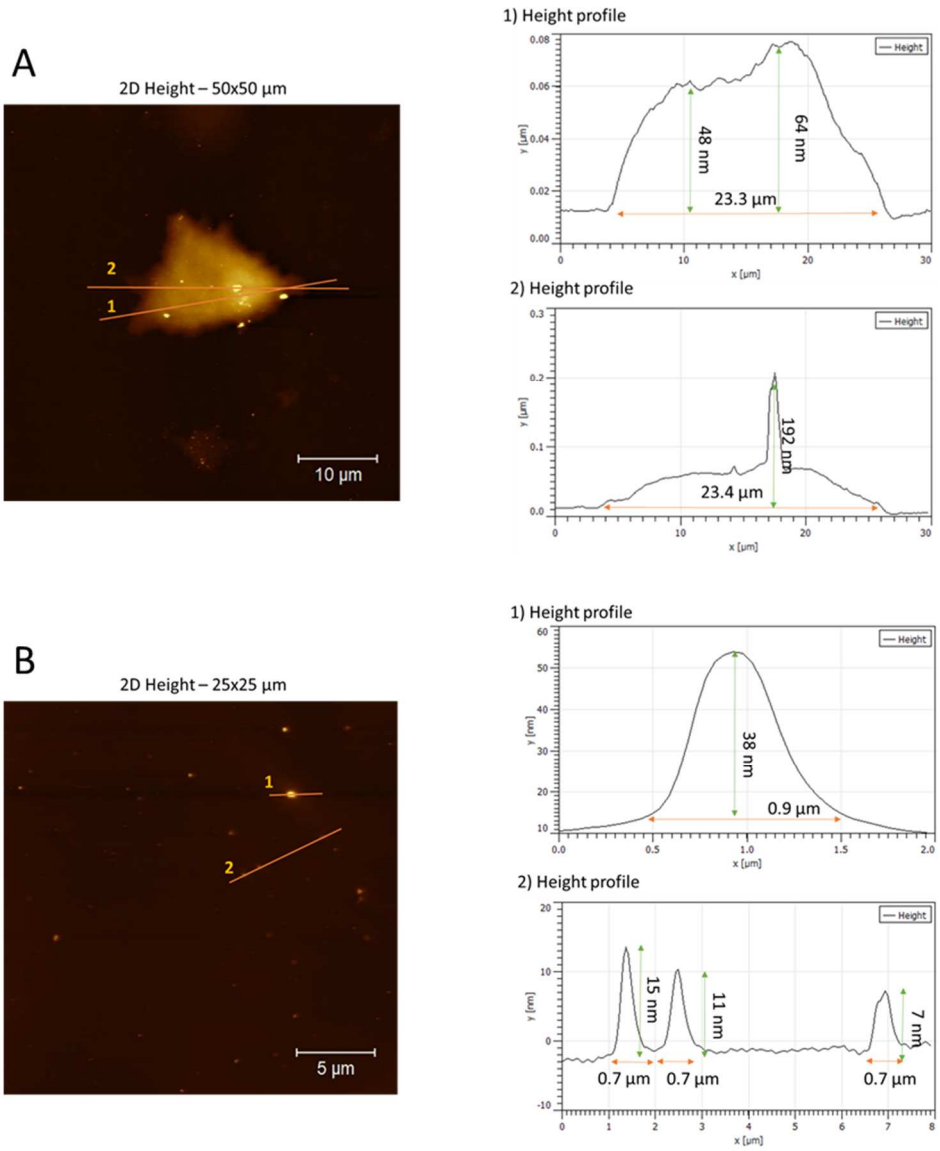

Figure 5.18 Profile height calculation of PVA@GO-Ag1

The HR-TEM images (Figure 5.19) shown a homogeneous material where it is not possible to define whether the GO moieties or the PVA ones are situated. The AgNPs are revealed as dark spots homogeneously dispersed in such a PVA@rGO background material, confirming a randomic formation of nucleation site within the polymer-based nanosystem. The random AgNPs localization also within the PVA matrix is in accordance with literature data, since the PVA acts also as a capping agent for AgNPs.[143-146] Thus, GO functional groups act as nucleation sites for AgNPs; on the other hand, AgNPs out of the GO platform could exploit the PVA -OH groups as capping agent, working as a homogeneous NPs stabilizer.

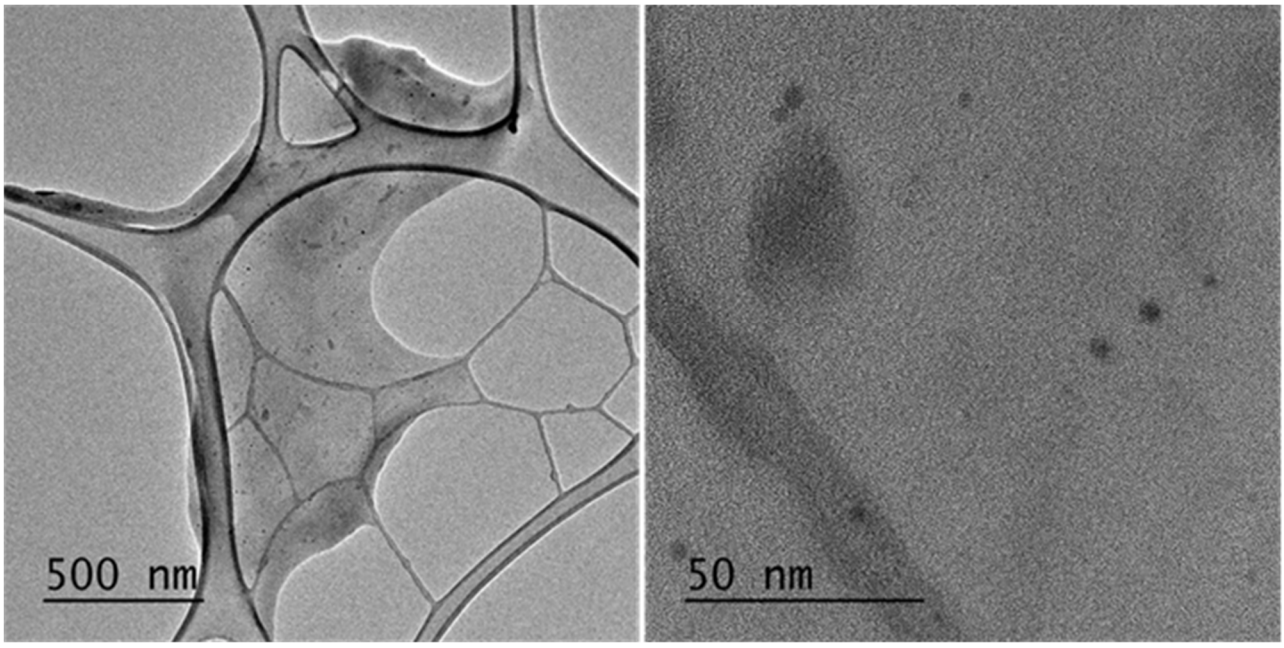

Figure 5.19 HR-TEM images of PVA@GO-Ag1 dried from aqueous solution.

Dynamic Light Scattering (DLS) analyses were performed to investigate the size of the nanosystem in water solution. The esterification of GO with PVA deeply influences the GO size distribution, resulting in two size distributions centered at 5 and 70 nm, respectively (Figure 5.20, black line). Those retrace the ones of pure PVA (Figure 5.20, black dashed line), despite the intensities of the signals the GO-polymer functionalization and the PVA entanglements effects (as previously discussed in Paragraph 5.2). Instead, the size distribution of PVA@GO-Ag1 suggests the increased hydrophilicity of the nanosystem due to the silver loading (Figure 5.20, red line).

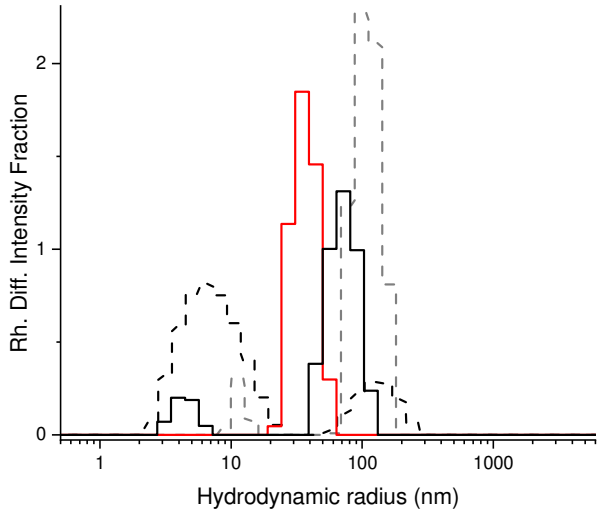

Figure 5.20 DLS measurements of GO (grey dashed line), PVA (black dashed line), PVA@GO (black line) and PVA@GO-Ag1 (red line) water solution (12.5 µg/mL).

Preliminary assay of the NanoHy-GPS Antibacterial activity

In the context of a worldwide spreading pandemic, the NanoHy-GPS become an attractive tool to limit contagion besides reducing the use and the consequent spreading of the common unhealthy disinfectants agents. Indeed, the application of the usual disinfection practices has already resulted in toxic effects towards humans, animals and the environment.[17,147]

To investigate the antibacterial performances of the PVA@GO-Ag nanosystem, an empirical test has been performed qualitatively considering the bacterial load typical of common use surfaces (i.e. keyboards, doors handle).

The anti-microbial effect of the PVA@GO-Ag-2 nanosystem has been compared with the bare AgNPs (the synthetic procedure is described in Materials and Methods) and Silver nitrate. The bacterial culture investigated was taken from surfaces and deposited over a Petri dish filled with Plate Count Agar. The experiment qualitatively compared the activity of bare AgNPs and $AgNO_3$, which are already known as antibacterial compounds, with that of PVA@GO-Ag2 (Figure 5.21). In particular, the PVA@GO-Ag2 was preferred instead of PVA@GO-Ag1, due to the higher AgNPs content. The effects of the bare PVA@GO moiety was also taken into account.

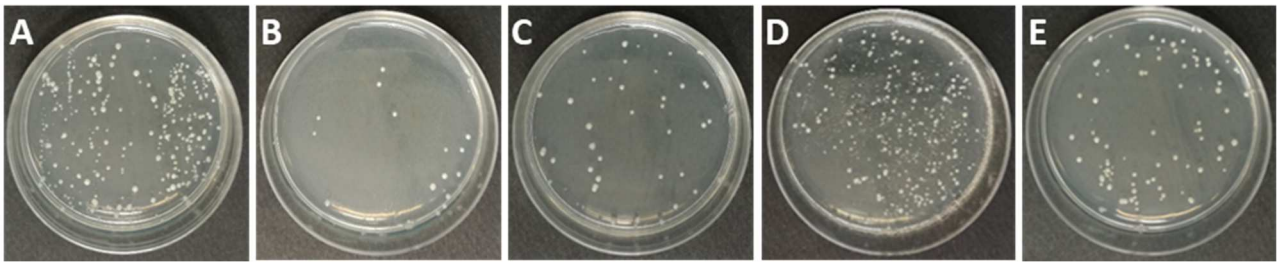

Figure 5.21 Antibacterial test in Plate Count Agar of: A) control experiment, B) PVA@GO-Ag2, C) AgNPs, D) PVA@GO, E) $AgNO_3$. The pictures were taken after incubation at 37 °C for 24 hours)

As expected, the PVA@GO-Ag2 (B) exhibited a very low bacterial proliferation compared to the control experiment (A), confirming the antibacterial efficacy of the new nanohybrid system. The bare PVA@GO shows a negligible antibacterial effect (D). Moreover, the silver treated Petri dishes (C, E) exhibited a generally lower bacterial proliferation than the control (A), confirming the occurrence of diffusion phenomenon of silver ions.

These positive results represent a proof of concept of the suitability of the nanohybrid system PVA@GO-Ag as a potential antibacterial additive for polymer matrices or coating, giving the nod to the systematic determination of the antibacterial activity. Thus, further experiments should be conducted employing model organisms such as Gram-positive *Staphylococcus aureus* and Gram-negative *Escherichia coli*, and taking into account the dosage of the Nanohybrid system and its minimum inhibitory concentration (MIC).

5.4 Conclusions

The development of a GO-based nanohybrid system has been systematically described in this Chapter, focusing on the individual development and characterization of the different moieties of the targeted nanosystem.

A microwave-assisted reduction was optimized to obtain reduced GO (rGOmw). Also, a traditional reduction of GO was performed employing hydrazine as a reducing agent (named rGOclassic), to use it as a comparative model. Structural differences have been found from TGA and FT-IR analysis. In particular, it was determined that rGOmw was more hydrophilic and exfoliated than rGOclassic. Moreover, through drying experiments on GO, rGOmw and rGOclassic, it has been found a correlation between the presence of water adsorbed and a degradation step occurring at about T=550 °C, attributed to water-mediated oxidations reactions of the carbon platform. It is noteworthy to observe that the microwave-assisted reduction does not affect the defectiveness of the rGOmw compared with pristine GO.

Subsequently, the synthesis of a PolyVinyl Alcohol (PVA) functionalized GO. The resulting PVA@GO could be assumed as GO platform esterified with PVA chains, confirmed by NMR measurements. The water-soluble material exhibited hydrodynamic radius size distribution similar to that of PVA, and has higher thermal stability than that of both PVA and GO counterparts. It is noteworthy to highlight that the GO grafting-to procedure here exposed allows the use of any polymer having suitable functionalities for esterification reactions, as side- and/or terminal-groups.

Once defined the reduction procedure and the PVA functionalization of the GO platform, the resulting PVA@GO was used as a platform to fix silver nanoparticles (AgNPs). With this aim, a microwave-assisted reduction procedure has been performed to assemble a nanohybrid system based on Polymer, Graphene and AgNPs, through a one-pot reaction which simultaneously reduces the GO and the Silver Nitrate.

The so-called PVA@GO-AgX systems were produced with different Ag content to investigate about the loading efficiency of the AgNPs and to perform valuable characterizations of the nanohybrid system. Thus, PVA@GO-Ag1, -2, and -3 were synthesised.

The reduction over the PVA@GO platform influences the AgNPs morphology: probably, the different chemical-physical properties of the nucleation sites allowed by the polymer-functionalized carbon platform allowed the growth of different shapes, which influences the LSPR UV-vis signal. As expected, the addition of increasing concentration of the silver nitrate induces the quantitative increase of the NPs presence. A quantitative determination of the silver content has been performed through TGA experiments.

The morphology of the nanosystems shows the AgNPs embedded with the PVA@GO matrix: it is supposed that the AgNPs nucleate and grow not only onto the GO platform but also within the polymer matrix, exploiting the hydroxyl groups as nucleation sites.

Nanotechnologies could fullfill the need to find an alternative to the common organic molecular systems used to make antimicrobial surfaces, especially for biomedical applications. The use of AgNPs embedded within a carbon-based nanosystem could provide a synergistic effect towards bacterial colonization. Indeed, graphene toxicity provides mechanical and oxidative stresses, while the AgNPs are a well-known broad-spectrum antibacterial agent. Moreover, the polymer functionalization is fundamental to ensure a strong sticking towards a substrate and/or a homogeneous mix within a polymer matrix. Thus, the polymer adopted must be the same or very similar (in terms of chemical-physical interactions) with the one of the treating substrate.

The synthetic pathway here exposed led to the NanoHybrid system composed of Polymer, Graphene and AgNPs, namely NanoHy-GPS. Thanks to the interchangeability of the polymer moiety, this system represents a new concept of on-demand tunable antimicrobial nanosystem.

In this context, the PVA@GO-Ag represents a useful model to confirm the designed study.

With the aim to apply the NanoHy-GPS not only over biomedical devices but also onto surfaces of common use objects, experimental proof of concept was conducted taking into account the bacterial load of doors handle. The results revealed that the PVA@GO-Ag2 exhibited similar anti-bacterial properties than that of bare AgNPs. Although further antibacterial experiments are needed to the systematic quantification of the efficiency of the nanohybrid system towards Gram-positive and/or Gram-negative model bacterial species (i.e. E. Coli and/or S. Aureus), the data reported here confirmed the potential antibacterial activity of the PVA@GO-Ag2.

The synthetic pathway adopted to synthesize the PVA@GO-Ag represents the first approach towards NanoHy-GPS synthesis. The method here exposed allows the fine-tuning of the nanosystem features, maximizing the interfacial interactions towards targeted substrates and/or optimizing the homogeneity of the dispersion within specific polymer matrices. The NanoHy-GPS is projected to be a valid alternative towards the common anti-bacterial agents, which incur to leaks within the environment and/or within organisms tissues. Indeed, thanks to the polymer-functionalization, a long-lasting coating is ensured: thus, the combined anti-bacterial activity of the hybrid system rGO-AgNPs would be expressed over-time. It is noteworthy to say that the NanoHy-GPS features are not yet explored in all their makings, and further studies are already planned. Indeed, besides the antibacterial activity, the high surface area of the rGO moiety could be also exploited as a drug-carrier. This last option is particularly interesting in biomedical on-demand devices: for example, specific drugs could be loaded onto the rGO platform, according to the patient need. So, while ensuring the anti-bacterial property, drugs (i.e. antinflammatory) could be released over-time from the device.

5.5 References

1 Costerton, J. W. Bacterial Biofilms: A Common Cause of Persistent Infections. *Science* **284**, 1318-1322, doi:10.1126/science.284.5418.1318 (1999).

2 Kingshott, P., Wei, J., Bagge-Ravn, D., Gadegaard, N. & Gram, L. Covalent Attachment of Poly(ethylene glycol) to Surfaces, Critical for Reducing Bacterial Adhesion. *Langmuir* **19**, 6912-6921, doi:10.1021/la034032m (2003).

3 Davies, D. G., Chakrabarty, A. M. & Geesey, G. G. Exopolysaccharide Production in Biofilms - Substratum Activation of Alginate Gene-Expression by Pseudomonas-Aeruginosa. *Appl Environ Microb* **59**, 1181-1186, doi:Doi 10.1128/Aem.59.4.1181-1186.1993 (1993).

4 Davies, D. G. & Geesey, G. G. Regulation of the Alginate Biosynthesis Gene Algc in Pseudomonas-Aeruginosa during Biofilm Development in Continuous-Culture. *Appl Environ Microb* **61**, 860-867, doi:Doi 10.1128/Aem.61.3.860-867.1995 (1995).

5 Sutherland, I. W. Biofilm exopolysaccharides: a strong and sticky framework. *Microbiology* **147**, 3-9, doi:10.1099/00221287-147-1-3 (2001).

6 Stoodley, P., Sauer, K., Davies, D. G. & Costerton, J. W. Biofilms as Complex Differentiated Communities. *Annual Review of Microbiology* **56**, 187-209, doi:10.1146/annurev.micro.56.012302.160705 (2002).

7 Costerton, J. W. *et al.* Bacterial Biofilms in Nature and Disease. *Annual Review of Microbiology* **41**, 435-464, doi:10.1146/annurev.mi.41.100187.002251 (1987).

8 Brown, M. R. W. & Gilbert, P. Sensitivity of biofilms to antimicrobial agents. *Journal of Applied Bacteriology* **74**, 87S-97S, doi:10.1111/j.1365-2672.1993.tb04345.x (1993).

9 Kamal, G. D., Pfaller, M. A., Rempe, L. E. & Jebson, P. J. R. Reduced Intravascular Catheter Infection by Antibiotic Bonding. *Jama* **265**, doi:10.1001/jama.1991.03460180070035 (1991).

10 Bowersock, T. L., Woodyard, L., Hamilton, A. J. & DeFord, J. A. Inhibition of Staphylococci by vancomycin absorbed on triidodecylmethyl ammonium chloride-coated intravenous catheter. *Journal of Controlled Release* **31**, 237-243, doi:10.1016/0168-3659(94)90005-1 (1994).

11 Shrivastava, A. in *Introduction to Plastics Engineering* 111-141 (2018).

12 McKeen, L. in *The Effect of Sterilization Methods on Plastics and Elastomers* 41-61 (2018).

13 Balmer, M. E. *et al.* Occurrence of methyl triclosan, a transformation product of the bactericide triclosan, in fish from various lakes in Switzerland. *Environ Sci Technol* **38**, 390-395, doi:DOI 10.1021/es030068p (2004).

14 Macherius, A. *et al.* Triclocarban, triclosan and its transformation product methyl triclosan in native earthworm species four years after a commercial-scale biosolids application. *Science of The Total Environment* **472**, 235-238, doi:10.1016/j.scitotenv.2013.10.113 (2014).

15 Fang, J.-L. *et al.* Occurrence, Efficacy, Metabolism, and Toxicity of Triclosan. *Journal of Environmental Science and Health, Part C* **28**, 147-171, doi:10.1080/10590501.2010.504978 (2010).

16 Weatherly, L. M. & Gosse, J. A. Triclosan exposure, transformation, and human health effects. *Journal of Toxicology and Environmental Health, Part B* **20**, 447-469, doi:10.1080/10937404.2017.1399306 (2017).

17 Nabi, G. *et al.* Massive use of disinfectants against COVID-19 poses potential risks to urban wildlife. *Environmental Research* **188**, doi:10.1016/j.envres.2020.109916 (2020).

18 Vasickova, P., Pavlik, I., Verani, M. & Carducci, A. Issues Concerning Survival of Viruses on Surfaces. *Food and Environmental Virology* **2**, 24-34, doi:10.1007/s12560-010-9025-6 (2010).

19 Banerjee, I., Pangule, R. C. & Kane, R. S. Antifouling Coatings: Recent Developments in the Design of Surfaces That Prevent Fouling by Proteins, Bacteria, and Marine Organisms. *Advanced Materials* **23**, 690-718, doi:10.1002/adma.201001215 (2011).

20 Kumar, A., Vemula, P. K., Ajayan, P. M. & John, G. Silver-nanoparticle-embedded antimicrobial paints based on vegetable oil. *Nature Materials* **7**, 236-241, doi:10.1038/nmat2099 (2008).

21 Desireddy, A. *et al.* Ultrastable silver nanoparticles. *Nature* **501**, 399-402, doi:10.1038/nature12523 (2013).

22 Sun, Y. Shape-Controlled Synthesis of Gold and Silver Nanoparticles. *Science* **298**, 2176-2179, doi:10.1126/science.1077229 (2002).

23 Li, W.-R. *et al.* Antibacterial activity and mechanism of silver nanoparticles on Escherichia coli. *Applied Microbiology and Biotechnology* **85**, 1115-1122, doi:10.1007/s00253-009-2159-5 (2009).

24 Morones, J. R. *et al.* The bactericidal effect of silver nanoparticles. *Nanotechnology* **16**, 2346-2353, doi:10.1088/0957-4484/16/10/059 (2005).

25 McShan, D., Ray, P. C. & Yu, H. Molecular toxicity mechanism of nanosilver. *Journal of Food and Drug Analysis* **22**, 116-127, doi:10.1016/j.jfda.2014.01.010 (2014).

26 Feng, Q. L. *et al.* A mechanistic study of the antibacterial effect of silver ions onEscherichia coli andStaphylococcus aureus. *Journal of Biomedical Materials Research* **52**, 662-668, doi:10.1002/1097-4636(20001215)52:4<662::Aid-jbm10>3.0.Co;2-3 (2000).

27 Matsumura, Y., Yoshikata, K., Kunisaki, S.-i. & Tsuchido, T. Mode of Bactericidal Action of Silver Zeolite and Its Comparison with That of Silver Nitrate. *Appl Environ Microb* **69**, 4278-4281, doi:10.1128/aem.69.7.4278-4281.2003 (2003).

28 Gupta, A., Maynes, M. & Silver, S. Effects of halides on plasmid-mediated silver resistance in Escherichia coli. *Appl Environ Microbiol* **64**, 5042-5045 (1998).

29 Rai, M. K., Deshmukh, S. D., Ingle, A. P. & Gade, A. K. Silver nanoparticles: the powerful nanoweapon against multidrug-resistant bacteria. *Journal of Applied Microbiology* **112**, 841-852, doi:10.1111/j.1365-2672.2012.05253.x (2012).

30 Liu, J., Wang, Z., Liu, F. D., Kane, A. B. & Hurt, R. H. Chemical Transformations of Nanosilver in Biological Environments. *ACS Nano* **6**, 9887-9899, doi:10.1021/nn303449n (2012).

31 Levard, C., Hotze, E. M., Lowry, G. V. & Brown, G. E. Environmental Transformations of Silver Nanoparticles: Impact on Stability and Toxicity. *Environ Sci Technol* **46**, 6900-6914, doi:10.1021/es2037405 (2012).

32 Unrine, J. M., Colman, B. P., Bone, A. J., Gondikas, A. P. & Matson, C. W. Biotic and Abiotic Interactions in Aquatic Microcosms Determine Fate and Toxicity of Ag Nanoparticles. Part 1. Aggregation and Dissolution. *Environ Sci Technol* **46**, 6915-6924, doi:10.1021/es204682q (2012).

33 Kellici, S. *et al.* Calixarene Assisted Rapid Synthesis of Silver-Graphene Nanocomposites with Enhanced Antibacterial Activity. *ACS Applied Materials & Interfaces* **8**, 19038-19046, doi:10.1021/acsami.6b06052 (2016).

34 Ocsoy, I. *et al.* Nanotechnology in Plant Disease Management: DNA-Directed Silver Nanoparticles on Graphene Oxide as an Antibacterial againstXanthomonas perforans. *ACS Nano* **7**, 8972-8980, doi:10.1021/nn4034794 (2013).

35 de Faria, A. F. *et al.* Eco-friendly decoration of graphene oxide with biogenic silver nanoparticles: antibacterial and antibiofilm activity. *Journal of Nanoparticle Research* **16**, doi:10.1007/s11051-013-2110-7 (2014).

36 Liu, S. *et al.* Antibacterial Activity of Graphite, Graphite Oxide, Graphene Oxide, and Reduced Graphene Oxide: Membrane and Oxidative Stress. *ACS Nano* **5**, 6971-6980, doi:10.1021/nn202451x (2011).

37 Hu, W. *et al.* Graphene-Based Antibacterial Paper. *ACS Nano* **4**, 4317-4323, doi:10.1021/nn101097v (2010).

38 Tang, J. *et al.* Graphene Oxide–Silver Nanocomposite As a Highly Effective Antibacterial Agent with Species-Specific Mechanisms. *ACS Applied Materials & Interfaces* **5**, 3867-3874, doi:10.1021/am4005495 (2013).

39 Compton, O. C. & Nguyen, S. T. Graphene Oxide, Highly Reduced Graphene Oxide, and Graphene: Versatile Building Blocks for Carbon-Based Materials. *Small* **6**, 711-723, doi:10.1002/smll.200901934 (2010).

40 Hsiao, M. C. *et al.* Preparation of Covalently Functionalized Graphene Using Residual Oxygen-Containing Functional Groups. *Acs Applied Materials & Interfaces* **2**, 3092-3099, doi:10.1021/am100597d (2010).

41 Park, S. *et al.* Hydrazine-reduction of graphite- and graphene oxide. *Carbon* **49**, 3019-3023, doi:10.1016/j.carbon.2011.02.071 (2011).

42 Stankovich, S. *et al.* Synthesis of graphene-based nanosheets via chemical reduction of exfoliated graphite oxide. *Carbon* **45**, 1558-1565, doi:10.1016/j.carbon.2007.02.034 (2007).

43 Park, S. *et al.* Colloidal Suspensions of Highly Reduced Graphene Oxide in a Wide Variety of Organic Solvents. *Nano Letters* **9**, 1593-1597, doi:10.1021/nl803798y (2009).

44 Fernández-Merino, M. J. *et al.* Vitamin C Is an Ideal Substitute for Hydrazine in the Reduction of Graphene Oxide Suspensions. *The Journal of Physical Chemistry C* **114**, 6426-6432, doi:10.1021/jp100603h (2010).

45 Gao, J. *et al.* Environment-Friendly Method To Produce Graphene That Employs Vitamin C and Amino Acid. *Chem Mater* **22**, 2213-2218, doi:10.1021/cm902635j (2010).

46 Zhang, J. *et al.* Reduction of graphene oxide vial-ascorbic acid. *Chem. Commun.* **46**, 1112-1114, doi:10.1039/b917705a (2010).

47 Shin, H. J. *et al.* Efficient Reduction of Graphite Oxide by Sodium Borohydride and Its Effect on Electrical Conductance. *Advanced Functional Materials* **19**, 1987-1992, doi:10.1002/adfm.200900167 (2009).

48 Ambrosi, A., Chua, C. K., Bonanni, A. & Pumera, M. Lithium Aluminum Hydride as Reducing Agent for Chemically Reduced Graphene Oxides. *Chem Mater* **24**, 2292-2298, doi:10.1021/cm300382b (2012).

49 Schniepp, H. C. *et al.* Functionalized Single Graphene Sheets Derived from Splitting Graphite Oxide. *The Journal of Physical Chemistry B* **110**, 8535-8539, doi:10.1021/jp060936f (2006).

50 Cote, L. J., Cruz-Silva, R. & Huang, J. Flash Reduction and Patterning of Graphite Oxide and Its Polymer Composite. *Journal of the American Chemical Society* **131**, 11027-11032, doi:10.1021/ja902348k (2009).

51 Wang, H., Robinson, J. T., Li, X. & Dai, H. Solvothermal Reduction of Chemically Exfoliated Graphene Sheets. *Journal of the American Chemical Society* **131**, 9910-9911, doi:10.1021/ja904251p (2009).

52 Liao, K.-H. *et al.* Aqueous Only Route toward Graphene from Graphite Oxide. *ACS Nano* **5**, 1253-1258, doi:10.1021/nn1028967 (2011).

53 Zhou, Y., Bao, Q., Tang, L. A. L., Zhong, Y. & Loh, K. P. Hydrothermal Dehydration for the "Green" Reduction of Exfoliated Graphene Oxide to Graphene and Demonstration of Tunable Optical Limiting Properties. *Chem Mater* **21**, 2950-2956, doi:10.1021/cm9006603 (2009).

54 Williams, G., Seger, B. & Kamat, P. V. TiO2-Graphene Nanocomposites. UV-Assisted Photocatalytic Reduction of Graphene Oxide. *ACS Nano* **2**, 1487-1491, doi:10.1021/nn800251f (2008).

55 Akhavan, O. & Ghaderi, E. Photocatalytic Reduction of Graphene Oxide Nanosheets on TiO2 Thin Film for Photoinactivation of Bacteria in Solar Light Irradiation. *The Journal of Physical Chemistry C* **113**, 20214-20220, doi:10.1021/jp906325q (2009).

56 Wang, Z., Zhou, X., Zhang, J., Boey, F. & Zhang, H. Direct Electrochemical Reduction of Single-Layer Graphene Oxide and Subsequent Functionalization with Glucose Oxidase. *The Journal of Physical Chemistry C* **113**, 14071-14075, doi:10.1021/jp906348x (2009).

57 Ramesha, G. K. & Sampath, S. Electrochemical Reduction of Oriented Graphene Oxide Films: An in Situ Raman Spectroelectrochemical Study. *The Journal of Physical Chemistry C* **113**, 7985-7989, doi:10.1021/jp811377n (2009).

58 Stankovich, S. *et al.* Graphene-based composite materials. *Nature* **442**, 282-286, doi:10.1038/nature04969 (2006).

59 Choi, B. G. *et al.* Solution Chemistry of Self-Assembled Graphene Nanohybrids for High-Performance Flexible Biosensors. *ACS Nano* **4**, 2910-2918, doi:10.1021/nn100145x (2010).

60 Liu, S. *et al.* Stable Aqueous Dispersion of Graphene Nanosheets: Noncovalent Functionalization by a Polymeric Reducing Agent and Their Subsequent Decoration with Ag Nanoparticles for Enzymeless Hydrogen Peroxide Detection. *Macromolecules* **43**, 10078-10083, doi:10.1021/ma102230m (2010).

61 Yang, F., Liu, Y., Gao, L. & Sun, J. pH-Sensitive Highly Dispersed Reduced Graphene Oxide Solution Using Lysozyme via an in Situ Reduction Method. *The Journal of Physical Chemistry C* **114**, 22085-22091, doi:10.1021/jp1079636 (2010).

62 López, V. *et al.* Chemical Vapor Deposition Repair of Graphene Oxide: A Route to Highly-Conductive Graphene Monolayers. *Advanced Materials* **21**, 4683-4686, doi:10.1002/adma.200901582 (2009).

63 Zólyomi, V., Koltai, J. & Kürti, J. Resonance Raman spectroscopy of graphite and graphene. *physica status solidi (b)* **248**, 2435-2444, doi:10.1002/pssb.201100295 (2011).

64 Ferrari, A. C. & Basko, D. M. Raman spectroscopy as a versatile tool for studying the properties of graphene. *Nature Nanotechnology* **8**, 235-246, doi:10.1038/nnano.2013.46 (2013).

65 Wu, J.-B., Lin, M.-L., Cong, X., Liu, H.-N. & Tan, P.-H. Raman spectroscopy of graphene-based materials and its applications in related devices. *Chemical Society Reviews* **47**, 1822-1873, doi:10.1039/c6cs00915h (2018).

66 Kotov, N. A., Dékány, I. & Fendler, J. H. Ultrathin graphite oxide-polyelectrolyte composites prepared by self-assembly: Transition between conductive and non-conductive states. *Advanced Materials* **8**, 637-641, doi:10.1002/adma.19960080806 (1996).

67 Pei, S. & Cheng, H.-M. The reduction of graphene oxide. *Carbon* **50**, 3210-3228, doi:10.1016/j.carbon.2011.11.010 (2012).

68 Luo, D., Zhang, G., Liu, J. & Sun, X. Evaluation Criteria for Reduced Graphene Oxide. *The Journal of Physical Chemistry C* **115**, 11327-11335, doi:10.1021/jp110001y (2011).

69 Etacheri, V., Michlits, G., Seery, M. K., Hinder, S. J. & Pillai, S. C. A Highly Efficient TiO2–xCx Nano-heterojunction Photocatalyst for Visible Light Induced Antibacterial Applications. *ACS Applied Materials & Interfaces* **5**, 1663-1672, doi:10.1021/am302676a (2013).

70 Wang, H., Xu, J.-Z., Zhu, J.-J. & Chen, H.-Y. Preparation of CuO nanoparticles by microwave irradiation. *Journal of Crystal Growth* **244**, 88-94, doi:10.1016/s0022-0248(02)01571-3 (2002).

71 Wada, Y. *et al.* Preparation of Nano-sized Nickel Metal Particles by Microwave Irradiation. *Chemistry Letters* **28**, 607-608, doi:10.1246/cl.1999.607 (1999).

72 Zhu, Y. *et al.* Microwave assisted exfoliation and reduction of graphite oxide for ultracapacitors. *Carbon* **48**, 2118-2122, doi:10.1016/j.carbon.2010.02.001 (2010).

73 Chen, W., Yan, L. & Bangal, P. R. Preparation of graphene by the rapid and mild thermal reduction of graphene oxide induced by microwaves. *Carbon* **48**, 1146-1152, doi:10.1016/j.carbon.2009.11.037 (2010).

74 Nethravathi, C. & Rajamathi, M. Chemically modified graphene sheets produced by the solvothermal reduction of colloidal dispersions of graphite oxide. *Carbon* **46**, 1994-1998, doi:10.1016/j.carbon.2008.08.013 (2008).

75 Mermoux, M., Chabre, Y. & Rousseau, A. Ftir and C-13 Nmr-Study of Graphite Oxide. *Carbon* **29**, 469-474, doi:Doi 10.1016/0008-6223(91)90216-6 (1991).

76 Chua, C. K. & Pumera, M. The reduction of graphene oxide with hydrazine: elucidating its reductive capability based on a reaction-model approach. *Chemical Communications* **52**, 72-75, doi:10.1039/c5cc08170j (2016).

77 Ossonon, B. D. & Bélanger, D. Synthesis and characterization of sulfophenyl-functionalized reduced graphene oxide sheets. *Rsc Adv* **7**, 27224-27234, doi:10.1039/c6ra28311j (2017).

78 He, D. *et al.* Mechanism of a green graphene oxide reduction with reusable potassium carbonate. *Rsc Adv* **5**, 11966-11972, doi:10.1039/c4ra14511a (2015).

79 D'Urso, L., Compagnini, G. & Puglisi, O. sp/sp2 bonding ratio in sp rich amorphous carbon thin films. *Carbon* **44**, 2093-2096, doi:10.1016/j.carbon.2006.04.016 (2006).

80 Kudin, K. N. *et al.* Raman Spectra of Graphite Oxide and Functionalized Graphene Sheets. *Nano Letters* **8**, 36-41, doi:10.1021/nl071822y (2008).

81 Malard, L. M., Pimenta, M. A., Dresselhaus, G. & Dresselhaus, M. S. Raman spectroscopy in graphene. *Physics Reports* **473**, 51-87, doi:10.1016/j.physrep.2009.02.003 (2009).

82 Russo, P., Compagnini, G., Musumeci, C. & Pignataro, B. Raman Monitoring of Strain Induced Effects in Mechanically Deposited Single Layer Graphene. *Journal of Nanoscience and Nanotechnology* **12**, 8755-8758, doi:10.1166/jnn.2012.6827 (2012).

83 Sengupta, R., Bhattacharya, M., Bandyopadhyay, S. & Bhowmick, A. K. A review on the mechanical and electrical properties of graphite and modified graphite reinforced polymer composites. *Progress in Polymer Science* **36**, 638-670, doi:10.1016/j.progpolymsci.2010.11.003 (2011).

84 Han, Z. & Fina, A. Thermal conductivity of carbon nanotubes and their polymer nanocomposites: A review. *Progress in Polymer Science* **36**, 914-944, doi:10.1016/j.progpolymsci.2010.11.004 (2011).

85 Potts, J. R., Dreyer, D. R., Bielawski, C. W. & Ruoff, R. S. Graphene-based polymer nanocomposites. *Polymer* **52**, 5-25, doi:10.1016/j.polymer.2010.11.042 (2011).

86 Caseri, W. Nanocomposites of polymers and metals or semiconductors: Historical background and optical properties. *Macromolecular Rapid Communications* **21**, 705-722, doi:Doi 10.1002/1521-3927(20000701)21:11<705::Aid-Marc705>3.0.Co;2-3 (2000).

87 Usuki, A. *et al.* Synthesis of nylon 6-clay hybrid. *Journal of Materials Research* **8**, 1179-1184, doi:10.1557/jmr.1993.1179 (2011).

88 Miao, C. & Hamad, W. Y. Cellulose reinforced polymer composites and nanocomposites: a critical review. *Cellulose* **20**, 2221-2262, doi:10.1007/s10570-013-0007-3 (2013).

89 Paul, D. R. & Robeson, L. M. Polymer nanotechnology: Nanocomposites. *Polymer* **49**, 3187-3204, doi:10.1016/j.polymer.2008.04.017 (2008).

90 Cano, M. *et al.* Improving the mechanical properties of graphene oxide based materials by covalent attachment of polymer chains. *Carbon* **52**, 363-371, doi:10.1016/j.carbon.2012.09.046 (2013).

91 May, P., Khan, U., O'Neill, A. & Coleman, J. N. Approaching the theoretical limit for reinforcing polymers with graphene. *J. Mater. Chem.* **22**, 1278-1282, doi:10.1039/c1jm15467b (2012).

92 Fang, M., Wang, K., Lu, H., Yang, Y. & Nutt, S. Covalent polymer functionalization of graphene nanosheets and mechanical properties of composites. *Journal of Materials Chemistry* **19**, doi:10.1039/b908220d (2009).

93 Layek, R. K. & Nandi, A. K. A review on synthesis and properties of polymer functionalized graphene. *Polymer* **54**, 5087-5103, doi:10.1016/j.polymer.2013.06.027 (2013).

94 Salavagione, H. J. & Martínez, G. Importance of Covalent Linkages in the Preparation of Effective Reduced Graphene Oxide–Poly(vinyl chloride) Nanocomposites. *Macromolecules* **44**, 2685-2692, doi:10.1021/ma102932c (2011).

95 Liu, Z., Robinson, J. T., Sun, X. & Dai, H. PEGylated Nanographene Oxide for Delivery of Water-Insoluble Cancer Drugs. *Journal of the American Chemical Society* **130**, 10876-10877, doi:10.1021/ja803688x (2008).

96 Sun, S. & Wu, P. A one-step strategy for thermal- and pH-responsive graphene oxide interpenetrating polymer hydrogel networks. *Journal of Materials Chemistry* **21**, doi:10.1039/c1jm10276a (2011).

97 Shan, C. *et al.* Water-Soluble Graphene Covalently Functionalized by Biocompatible Poly-l-lysine. *Langmuir* **25**, 12030-12033, doi:10.1021/la903265p (2009).

98 Vuluga, D. *et al.* Straightforward synthesis of conductive graphene/polymer nanocomposites from graphite oxide. *Chemical Communications* **47**, doi:10.1039/c0cc04623j (2011).

99 Sun, S., Cao, Y., Feng, J. & Wu, P. Click chemistry as a route for the immobilization of well-defined polystyrene onto graphene sheets. *Journal of Materials Chemistry* **20**, doi:10.1039/c0jm01269f (2010).

100 Xu, Z. & Gao, C. In situPolymerization Approach to Graphene-Reinforced Nylon-6 Composites. *Macromolecules* **43**, 6716-6723, doi:10.1021/ma1009337 (2010).

101 Hassan, C. M. & Peppas, N. A. in *Biopolymers · PVA Hydrogels, Anionic Polymerisation Nanocomposites Advances in Polymer Science* Ch. Chapter 2, 37-65 (2000).

102 Oka, M. Biomechanics and repair of articular cartilge. *Journal of Orthopaedic Science* **6**, 448-456, doi:10.1007/s007760170014 (2001).

103 Oka, M. *et al.* Development of an artificial articular cartilage. *Clinical Materials* **6**, 361-381, doi:10.1016/0267-6605(90)90053-x (1990).

104 Stammen, J. A., Williams, S., Ku, D. N. & Guldberg, R. E. Mechanical properties of a novel PVA hydrogel in shear and unconfined compression. *Biomaterials* **22**, 799-806, doi:10.1016/s0142-9612(00)00242-8 (2001).

105 Święszkowski, W., Ku, D. N., Bersee, H. E. N. & Kurzydlowski, K. J. An elastic material for cartilage replacement in an arthritic shoulder joint. *Biomaterials* **27**, 1534-1541, doi:10.1016/j.biomaterials.2005.08.032 (2006).

106 Kita, M. *et al.* Evaluation of polyvinyl alcohol hydrogel as a soft contact lens material. *Graefe's Archive for Clinical and Experimental Ophthalmology* **228**, 533-537, doi:10.1007/bf00918486 (1990).

107 Neises, B. & Steglich, W. Simple Method for the Esterification of Carboxylic Acids. *Angewandte Chemie International Edition in English* **17**, 522-524, doi:10.1002/anie.197805221 (1978).

108 Hu, H. *et al.* Preparation and properties of graphene nanosheets–polystyrene nanocomposites via in situ emulsion polymerization. *Chemical Physics Letters* **484**, 247-253, doi:10.1016/j.cplett.2009.11.024 (2010).

109 Neri, G. *et al.* Engineering of carbon based nanomaterials by ring-opening reactions of a reactive azlactone graphene platform. *Chemical Communications* **51**, 4846-4849, doi:10.1039/c5cc00518c (2015).

110 Salavagione, H. J., Gómez, M. n. A. & Martínez, G. Polymeric Modification of Graphene through Esterification of Graphite Oxide and Poly(vinyl alcohol). *Macromolecules* **42**, 6331-6334, doi:10.1021/ma900845w (2009).

111 Ballistreri, A., Foti, S., Montaudo, G. & Scamporrino, E. Evolution of aromatic compounds in the thermal decomposition of vinyl polymers. *Journal of Polymer Science: Polymer Chemistry Edition* **18**, 1147-1153, doi:10.1002/pol.1980.170180401 (1980).

112 Tsuchiya, Y. & Sumi, K. Thermal decomposition products of poly(vinyl alcohol). *Journal of Polymer Science Part A-1: Polymer Chemistry* **7**, 3151-3158, doi:10.1002/pol.1969.150071111 (1969).

113 Jellinek, H. H. G. Polymer degradation, by Tibor Kelen, Van Nostrand Reinhold, New York, 1982. *Journal of Polymer Science: Polymer Letters Edition* **21**, 956-958, doi:10.1002/pol.1983.130211119 (1983).

114 Cobos, M., Fernández, M. & Fernández, M. Graphene Based Poly(Vinyl Alcohol) Nanocomposites Prepared by In Situ Green Reduction of Graphene Oxide by Ascorbic Acid: Influence of Graphene Content and Glycerol Plasticizer on Properties. *Nanomaterials* **8**, doi:10.3390/nano8121013 (2018).

115 Rahim, M. *et al.* in *Inorganic Frameworks as Smart Nanomedicines* 185-237 (2018).

116 Franci, G. *et al.* Silver Nanoparticles as Potential Antibacterial Agents. *Molecules* **20**, 8856-8874, doi:10.3390/molecules20058856 (2015).

117 Burdușel, A.-C. *et al.* Biomedical Applications of Silver Nanoparticles: An Up-to-Date Overview. *Nanomaterials* **8**, doi:10.3390/nano8090681 (2018).

118 Kamyshny, A. & Magdassi, S. Conductive Nanomaterials for Printed Electronics. *Small* **10**, 3515-3535, doi:10.1002/smll.201303000 (2014).

119 Vigneshwaran, N., Kathe, A. A., Varadarajan, P. V., Nachane, R. P. & Balasubramanya, R. H. Functional Finishing of Cotton Fabrics Using Silver Nanoparticles. *Journal of Nanoscience and Nanotechnology* **7**, 1893-1897, doi:10.1166/jnn.2007.737 (2007).

120 Zhou, X., Liu, G., Yu, J. & Fan, W. Surface plasmon resonance-mediated photocatalysis by noble metal-based composites under visible light. *Journal of Materials Chemistry* **22**, doi:10.1039/c2jm31902k (2012).

121 Rycenga, M. *et al.* Controlling the Synthesis and Assembly of Silver Nanostructures for Plasmonic Applications. *Chemical Reviews* **111**, 3669-3712, doi:10.1021/cr100275d (2011).

122 Kelly, K. L., Coronado, E., Zhao, L. L. & Schatz, G. C. The Optical Properties of Metal Nanoparticles: The Influence of Size, Shape, and Dielectric Environment. *The Journal of Physical Chemistry B* **107**, 668-677, doi:10.1021/jp026731y (2003).

123 Wiley, B., Sun, Y. & Xia, Y. Synthesis of Silver Nanostructures with Controlled Shapes and Properties. *Accounts of Chemical Research* **40**, 1067-1076, doi:10.1021/ar7000974 (2007).

124 Le Ru, E. C. & Etchegoin, P. G. *Principles of surface-enhanced Raman spectroscopy : and related plasmonic effects*. 1st edn, (Elsevier, 2009).

125 Dos Santos, C. A. *et al.* Silver Nanoparticles: Therapeutical Uses, Toxicity, and Safety Issues. *Journal of Pharmaceutical Sciences* **103**, 1931-1944, doi:10.1002/jps.24001 (2014).

126 Andersson, D. I. & Hughes, D. Antibiotic resistance and its cost: is it possible to reverse resistance? *Nature Reviews Microbiology* **8**, 260-271, doi:10.1038/nrmicro2319 (2010).

127 D'Costa, V. M. *et al.* Antibiotic resistance is ancient. *Nature* **477**, 457-461, doi:10.1038/nature10388 (2011).

128 Walker, B. *et al.* Looming Global-Scale Failures and Missing Institutions. *Science* **325**, 1345-1346, doi:10.1126/science.1175325 (2009).

129 Lee, P. C. & Meisel, D. Adsorption and surface-enhanced Raman of dyes on silver and gold sols. *The Journal of Physical Chemistry* **86**, 3391-3395, doi:10.1021/j100214a025 (1982).

130 Raveendran, P., Fu, J. & Wallen, S. L. Completely "Green" Synthesis and Stabilization of Metal Nanoparticles. *Journal of the American Chemical Society* **125**, 13940-13941, doi:10.1021/ja029267j (2003).

131 Sharma, V. K., Yngard, R. A. & Lin, Y. Silver nanoparticles: Green synthesis and their antimicrobial activities. *Advances in Colloid and Interface Science* **145**, 83-96, doi:10.1016/j.cis.2008.09.002 (2009).

132 Qin, Y. *et al.* Size control over spherical silver nanoparticles by ascorbic acid reduction. *Colloids and Surfaces A: Physicochemical and Engineering Aspects* **372**, 172-176, doi:10.1016/j.colsurfa.2010.10.013 (2010).

133 Hebbalalu, D., Lalley, J., Nadagouda, M. N. & Varma, R. S. Greener Techniques for the Synthesis of Silver Nanoparticles Using Plant Extracts, Enzymes, Bacteria, Biodegradable Polymers, and Microwaves. *ACS Sustainable Chemistry & Engineering* **1**, 703-712, doi:10.1021/sc4000362 (2013).

134 Moulton, M. C. *et al.* Synthesis, characterization and biocompatibility of "green" synthesized silver nanoparticles using tea polyphenols. *Nanoscale* **2**, doi:10.1039/c0nr00046a (2010).

135 Nadagouda, M. N. & Varma, R. S. Green synthesis of silver and palladium nanoparticles at room temperature using coffee and tea extract. *Green Chemistry* **10**, doi:10.1039/b804703k (2008).

136 Davidson, C. A., Griffith, C. J., Peters, A. C. & Fielding, L. M. Evaluation of two methods for monitoring surface cleanliness—ATP bioluminescence and traditional hygiene swabbing. *Luminescence* **14**, 33-38, doi:10.1002/(sici)1522-7243(199901/02)14:1<33::Aid-bio514>3.0.Co;2-i (1999).

137 Devi, C. U., Sharma, A. K. & Rao, V. V. R. N. Electrical and optical properties of pure and silver nitrate-doped polyvinyl alcohol films. *Materials Letters* **56**, 167-174, doi:10.1016/s0167-577x(02)00434-2 (2002).

138 Kandhol, G., Wadhwa, H., Chand, S., Mahendia, S. & Kumar, S. Study of dielectric relaxation behavior of composites of Poly (vinyl alchohol) (PVA) and Reduced graphene oxide (RGO). *Vacuum* **160**, 384-393, doi:10.1016/j.vacuum.2018.11.051 (2019).

139 Peng, T., Sun, H., Peng, T., Liu, B. & Zhao, X. Structural Regulation and Electroconductivity Change of Nitrogen-Doping Reduced Graphene Oxide Prepared Using p-Phenylene Diamine as Modifier. *Nanomaterials* **7**, doi:10.3390/nano7100292 (2017).

140 Yao, S., Li, Y., Zhou, Z. & Yan, H. Graphene oxide-assisted preparation of poly(vinyl alcohol)/carbon nanotube/reduced graphene oxide nanofibers with high carbon content by electrospinning technology. *RSC Advances* **5**, 91878-91887, doi:10.1039/c5ra15985g (2015).

141 Agnihotri, S., Mukherji, S. & Mukherji, S. Size-controlled silver nanoparticles synthesized over the range 5–100 nm using the same protocol and their antibacterial efficacy. *RSC Adv.* **4**, 3974-3983, doi:10.1039/c3ra44507k (2014).

142 Kyrychenko, A., Pasko, D. A. & Kalugin, O. N. Poly(vinyl alcohol) as a water protecting agent for silver nanoparticles: the role of polymer size and structure. *Physical Chemistry Chemical Physics* **19**, 8742-8756, doi:10.1039/c6cp05562a (2017).

143 Ajitha, B., Kumar Reddy, Y. A., Reddy, P. S., Jeon, H.-J. & Ahn, C. W. Role of capping agents in controlling silver nanoparticles size, antibacterial activity and potential application as optical hydrogen peroxide sensor. *Rsc Adv* **6**, 36171-36179, doi:10.1039/c6ra03766f (2016).

144 Saha, S. K., Chowdhury, P., Saini, P. & Babu, S. P. S. Ultrasound assisted green synthesis of poly(vinyl alcohol) capped silver nanoparticles for the study of its antifilarial efficacy. *Applied Surface Science* **288**, 625-632, doi:10.1016/j.apsusc.2013.10.085 (2014).

145 Ananth, A. N., Daniel, S. C. G. K., Sironmani, T. A. & Umapathi, S. PVA and BSA stabilized silver nanoparticles based surface–enhanced plasmon resonance probes for protein detection. *Colloids and Surfaces B: Biointerfaces* **85**, 138-144, doi:10.1016/j.colsurfb.2011.02.012 (2011).

146 Filippo, E., Serra, A. & Manno, D. Poly(vinyl alcohol) capped silver nanoparticles as localized surface plasmon resonance-based hydrogen peroxide sensor. *Sensors and Actuators B: Chemical* **138**, 625-630, doi:10.1016/j.snb.2009.02.056 (2009).

147 Chang, A. *et al.* Cleaning and Disinfectant Chemical Exposures and Temporal Associations with COVID-19 — National Poison Data System, United States, January 1, 2020–March 31, 2020. *MMWR. Morbidity and Mortality Weekly Report* **69**, 496-498, doi:10.15585/mmwr.mm6916e1 (2020).

6 General Conclusions and perspectives

The work exposed in this PhD thesis highlighted the fundamental role of the polymers in tuning the Graphene Oxide features to obtain useful properties for applications in different fields such as nanomedicine, health and environmental remediation. In-depth investigations about the GO structure, the suitable procedures for its polymer functionalization and the subsequential effects on the chemical-physical properties of the GO derivatives have been performed.

With the aim to synthesize advanced functional materials, covalent and non-covalent approaches towards the GO functionalization have been used to take full advantage of the polymer features.

Thus, it has been demonstrated that by designing the synthetic procedure and choosing the nature of the polymers, it is possible to fine-tune the synergetic properties of the resulting GO-based polymer derivative, making this last feasible for specific applications.

It has been shown that the purposes of both polymer and GO change case-by-case, thus allowing the engineering of different nano-devices through the synergistic matching of the two components, assembling: optical sensors for water pollutants, polymer-supported GO-based photocatalysts, drug carriers, and antibacterial coatings.

Polymer-based GO nanosystems confirm themselves as a promising future alternative for smart nano-devices. Because the inorganic finite sources are the main raw material for advanced nanotechnology devices (as an example, the photocatalysts for water remediation are mainly based on titanium dioxide), to support the sustainability of technology it is necessary to switch towards cheap and widespread sources, such as the carbon-based materials.

The potential of the Polymer-based GO systems here exposed is not yet exploited in full. Apart from further optimization of the nanosystems here described, the perspectives of this work are oriented to the multi-purposeness of the GO-based systems.

Particular interests are involved in NanoHy-GPS concept. Indeed, the need to find an alternative to the common antimicrobial agents is well-defined worldwide, especially in a post-pandemic scenario. The results exposed here confirmed the potential application of the NanoHy-GPS as a universal antimicrobial coating and/or nanofiller. Furthermore, other features could be added to this system, such as triggered drug release. In this way, biomedical on-demand tunable multi-purpose devices able to prevent infections and perform localized therapies, could be produced on the needs of the treated patient.

This work represents a starting point to unveil the potentialities of polymer-based GO nanosystems, which will be fully exploited in the next future.

7 Methods

7.1 MALDI-TOF

MALDI-TOF mass spectra were acquired with a Voyager DE (PerSeptive Biosystem) which, using the delay extraction device[1,2] (25 kV applied after 2600 ns, with a potential gradient of 454 V mm^{-1} and a wire voltage of 25 V), detects the ions in linear mode. Trans-2-[3-(4-tert-Butylphenyl)-2-methyl-2-propenylidene] malononitrile (DCTB) was used as matrix. Mass spectrometer calibration was performed as previously published,[3] and weight-average molecular weights were determined using a Grams software (PerSeptive Biosystem) applied on the spectra corrected for the offset and the baseline, in accordance with a previously reported method.[2] Each m/z value reported in the spectra and in the present text, refers to the ion containing the most abundant isotope of each element present in the molecule.

7.2 NMR analysis

^{1}H-NMR, COSY, and ROESY spectra were obtained using a ^{UNITY}INOVA Varian instrument operating at 500 MHz (^{1}H) using VNMR for software acquisition and processing. The samples were dissolved in CD_2Cl_2 and the chemical shifts were expressed in ppm and compared with the CH_2Cl_2 residue signal. The spectra were acquired at 27 °C, with a 0.5 second spinlock time.

7.3 Spectroscopic techniques

UV-visible spectra were recorded with a Shimadzu UV-1601 spectrophotometer at 25 ± 0.1 °C, using quartz cuvettes with a 1 cm path length and water (LC-mass grade), THF (Sigma-Aldrich) or CH_2Cl_2 as solvents.

Luminescence measurements were carried out using a Jasco FP-8200 spectrophotometer, equipped with a 150 W xenon lamp, using quartz cuvettes with a 1 cm path length.

FT-IR spectra were obtained by using a Perkin Elmer Spectrum One spectrophotometer. The samples were prepared by using the KBr pellet method.

Surface Enhanced Raman Scattering (SERS) experiments were performed using a Witech Alpha 300 RS Raman spectrometer. The samples in form of solid powder were deposited onto Silicon wafer as a substrate. Raman spectra have been excited with a 633 nm laser line of a Coherent Compass

Sapphire Laser, with10x10s accumulations, and have been collected with a 50x objective (spot size of about 2 μm).

7.4 Thermal Analysis

Thermogravimetric analyses were conducted using a Perkin-Elmer TGA 7 equipped with a TAC 7/DX with a thermal ramp of 10 °C min^{-1}, in oxidative atmosphere (air, 60 mL min^{-1}).
Differential scanning calorimetry (DSC) measurements were conducted by means of a TA Q20 instrument, equipped with a Refrigerant Cooling System, with a heating rate of 10 °C min^{-1}, in the −90 to +90 °C temperature range and under an anhydrous N_2 atmosphere (60 mL min^{-1}).

7.5 SEM-EDX

Surface morphology was investigated using field emission scanning electron microscopy (FE-SEM) using a ZEISS SUPRA 55 VP instrument. The samples were deposited on carbon-tape.
The atomic composition of the samples was analysed through energy dispersive X-ray (EDX) analysis, using an INCA-Oxford windowless detector, having a resolution of 127 eV as the full width half maximum (FWHM) of the Mn Kα.

7.6 Microwave reactor

Microwave-assisted reactions were performed ina single-mode microwave reactor (CEM Discover S-Class) equipped with a calibrated infrared temperature sensor (maximum temperature 300 °C, maximum power 300 W, maximum pressure 300 psi).

7.7 HR-TEM

HRTEM images were obtained using a high-resolution transmission electron microscope HR-TEM FEI Titan G2 60–300 (Thermo Fisher Scientific, Waltham, MA, USA) with an X-FEG type emission gun, operating at 80 kV. This microscope was also supplied with a Cs image corrector and a STEM High-Angle Annular Dark-Field detector (HAADF). For these analyses, a droplet of the material ultrapure H2O dispersion (0.1 mg mL-1) was deposited onto a carbon-coated copper grid and dried.

7.8 AFM

Combined system NTEGRA Spectra (NT-MDT, Russia) was utilized to acquire sample topography (software Nova Px. 3.4.0 rev. 19040). The surface morphology was obtained by the means of semi-contact mode (height and phase) with the NSG30 (High Resolution NONCONTACT "GOLDEN", NT-MDT, Russia) cantilever having a force constant of 22-100 N/m and resonant frequency 240 – 440 kHz and the ACTA-SS (AppNano, USA) cantilever having a force constant of 13-77 N/m and resonant frequency of 200 – 400 kHz. The scanning rate was 0.3 Hz. During the measurement, the humidity was in range of 45-55% and the temperature was RT. The height profile was calculated using Gwyddion 2.51 software.

The sample was dissolved in water and sonicated at least 60 min. Total volume of 3 μL of the as-prepared sample was deposited at freshly cleaved MICA substrate via drag and drop method and left to dry.

7.9 References

1 Mineo, P., Vitalini, D., Scamporrino, E., Bazzano, S. & Alicata, R. Effect of delay time and grid voltage changes on the average molecular mass of polydisperse polymers and polymeric blends determined by delayed extraction matrix-assisted laser desorption/ionization time-of-flight mass spectrometry. *Rapid Commun Mass Sp* **19**, 2773-2779, doi:10.1002/rcm.2123 (2005).

2 Vitalini, D., Mineo, P. & Scamporrino, E. Effect of combined changes in delayed extraction time and potential gradient on the mass resolution and ion discrimination in the analysis of polydisperse polymers and polymer blends by delayed extraction matrix-assisted laser desorption/ionization time-of-flight mass spectrometry. *Rapid Commun Mass Sp* **13**, 2511-2517, doi:10.1002/(Sici)1097-0231(19991230)13:24<2511::Aid-Rcm819>3.0.Co;2-Y (1999).

3 Scamporrino, E., Vitalini, D. & Mineo, P. Synthesis and MALDI-TOF MS characterization of high molecular weight poly(1,2-dihydroxybenzene phthalates) obtained by uncatalyzed bulk polymerization of O,O'-phthalid-3-ylidenecatechol or 4-methyl-O,O'-phthalid-3-ylidenecatechol. *Macromolecules* **29**, 5520-5528, doi:10.1021/Ma960051+ (1996).

8 Research Products

8.1 Peer reviewed Journal Publications

11. Piperno, A.; Foti, C.; Mineo, P.G.; **Nicosia, A.**; Scala, A.; Neri, G. Recent Advances of Graphene Based Strategies for Arsenic Remediation, *Frontiers in Chemistry, section Green and Sustainable Chemistry,* Article in Press
10. **Nicosia, A.**; Vento, F.; Pellegrino, A.L.; Ranc, V.; Piperno, A.; Mazzaglia, A.; Mineo, P. Polymer-Based Graphene Derivatives and Microwave-Assisted Silver Nanoparticles Decoration as a Potential Antibacterial Agent, *Nanomaterials*, 2020, 10(11), 2269, DOI: 10.3390/nano10112269
9. Tomasella, P.; Sanfilippo, V.; Bonaccorso, C.; Cucci, L.M.; Consiglio, G.; **Nicosia, A.**; Mineo, P.G.; Forte, G.; Satriano, C. Theranostic Nanoplatforms of Thiolated Reduced Graphene Oxide Nanosheets and Gold Nanoparticles, *Applied Sciences*, 2020, 10(16), 5529, DOI: 10.3390/app10165529
8. **Nicosia, A.**; Vento, F.; Satriano, C.; Villari, V.; Micali, N.; Cucci, L. M.; Sanfilippo, V.; Mineo, P. G. Light-Triggered Polymeric Nanobombs for Targeted Cell Death, *ACS Applied Nano Materials*, 2020, 3, 2, 1950–1960, DOI: 10.1021/acsanm.9b02552
7. Gentile, D.; Floresta, G.; Patamia, V.; **Nicosia, A.**; Mineo, P. G.; Rescifina, A. Cucurbit[7]uril as a catalytic nanoreactor for one-pot synthesis of isoxazolidines in water, *Organic & Biomolecular Chemistry*, 2020, 18, 1194-1203, DOI: 10.1039/C9OB02352F
6. Micali, N.; Mineo, P.; Vento, F.; **Nicosia, A.**; Villari, V. Supramolecular structures formed in water by Graphene Oxide and Nonionic PEGylated Porphyrin: Interaction mechanisms and fluorescence quenching effects, *The Journal of Physical Chemistry C*, 2019, 123, 42, 25977–25984, DOI: 10.1021/acs.jpcc.9b06800
5. Castriciano, M.A.; Cardiano, P.; Fazio, E.; Mineo, P. G.; **Nicosia, A.**; Zagami, R.; Trapani, M.; Monsù Scolaro, L.; Lo Schiavo, S. Novel Luminescent Ionic Adducts Based on Pyrene-1-sulfonate, *ACS Omega*, 2018, 3, 12, 18811–18820, DOI: 10.1021/acsomega.8b02961
4. Scala, A.; Piperno, A.; Torcasio, S. M.; **Nicosia, A.**; Mineo, P. G.; Grassi, G. "Clickable" polylactic acids obtained by solvent free intra-chain amidation, *European Polymer Journal*, 2018, 109, 341-346, DOI: 10.1016/j.eurpolymj.2018.10.004
3. Mineo P.G.; Vento, F.; Abbadessa, A.; Scamporrino, E.; **Nicosia, A.*** An optical sensor of acidity in fuels based on a porphyrin derivative, *Dyes and Pigments*, 2019, 161, 147-154, DOI: 10.1016/j.dyepig.2018.09.045

2. Varrica, M. G.; Zagni, C.; Mineo, P. G.; Floresta, G.; Monciino, G.; Pistara, V.; Abbadessa, A.; **Nicosia, A.**; Castilho, R. M.; Amata, E.; Rescifina, A. DNA intercalators based on (1,10-phenanthrolin-2-yl)isoxazolidin-5-yl core with better growth inhibition and selectivity than cisplatin upon head and neck squamous cells carcinoma, *European Journal of Medicinal Chemistry*, 2018, 143, 583-590, DOI: 10.1016/j.ejmech.2017.11.067
1. Mineo, P.; Abbadessa, A.; Rescifina, A.; Mazzaglia, A.; **Nicosia, A.**; Scamporrino, A. PEGylate porphyrin-gold nanoparticles conjugates as removable pH-sensor nano-probes for acidic environments, *Colloids and Surfaces A: Physicochemical and Engineering Aspects*, 2018, 546, 40-47, DOI: 10.1016/j.colsurfa.2018.02.061

8.2 Conference Contributions

[† Oral, ‡ Poster]

† Abstract in conference proceeding "Workshop delle sezioni Sicilia e Calabria della Società Chimica Italiana 2017", in "*Spontaneous symmetry breaking phenomenon of porphyrin aggregates in stagnant aqueous solution: action of an asymmetric weak thermal gradient"*

† Abstract in conference proceeding "Workshop delle sezioni Sicilia e Calabria della Società Chimica Italiana 2017", in "Hybrid nano-structured systems pophyrin based for biomedical applications"

† Abstract in conference proceeding "XXVI Congresso Nazionale della Società Chimica Italiana", in "*Synthesis and characterization of copolycarbonates having azobenzene units in the main chain as an active group for optical logic gate devices"*

† Abstract in conference proceeding "Workshop delle sezioni Sicilia and Calabria della Società Chimica Italiana 2018", in "*Correlation between building blocks structure and effects on symmetry breaking about supramolecular aggregates of porphyrin derivatives*"

† Abstract in conference proceeding "MacroGiovani 2018, Associazione Italiana di Scienza e Tecnologia delle Macromolecole", in "*Correlation between building blocks structure and effects on Symmetry Breaking Phenomenon in supramolecular aggregates made of porphyrin based polymers*"

† Abstract in conference proceeding "XXIII Convegno Nazionale Associazione Italiana di Scienza e Tecnologia delle Macromolecole" in "*Structure-effects correlation on Symmetry Breaking Phenomenon in supramolecular aggregates of porphyrin based polymers"*

† Abstract in conference proceeding "Merck & Elsevier Young Chemists Symposium XVIII Edition" in "*Structure-effects correlation on Symmetry Breaking Phenomenon in supramolecular aggregates of porphyrin based polymers"*

† Abstract in conference proceeding "Workshop delle sezioni Sicilia e Calabria della Società Chimica Italiana 2020", in "*Laser triggered Polymer-based Nanobombs for localized cellular treatments"*

‡ 09\02-10\02\2017 Conference of "Italian Chemical Society", entitled "*Spontaneous symmetry breaking phenomenon of porphyrin aggregates in stagnant aqueous solution: action of an asymmetric weak thermal gradient*"

‡ 05/03/2019 "RSC Twitter Poster Conference 2019", entitled"*Spontaneous Symmetry Breaking: the perfect imperfection of the nature*"

8.3 Awards and recognitions

• 09/08/2019 Winner of the *"Best Solution Award"* at EIT health Traslational Fellowship program 2019 (held at St'Anne College – Oxford University), with a pitch about "Nano-HyGPS: A nano defence against bacterial contaminations"

• 06-07/11/2019 Invited poster presentation at "EIT Health Alumni Showcase 2019", held in Lisbon (Portugal), entitled "NanoHyGPS: a nanodefence against bacterial contaminations"

• 28/01/2020 Winner of the "Chemistry's Got Talent" awarded by University of Florence, with a digital graphic drawing titled "Periodic Table of the Elements: the alphabet of the Universe"

9 Other Scientific activities

9.1 Teaching activity

• May-August 2020, Tutor of 2 academic courses for students during the II° semester of the academic year 2019-2020:

- "Macromolecular Chemistry" (Bachelor's degree in "Chemistry")
- "Fundaments of Polymer Chemistry and Laboratory" (Bachelor's degree in "Industrial Chemistry")

• Co-supervisor of 2 Bachelor's degree Thesis and 1 Master's degree Thesis:

-Giovanni Di Benedetto, "Validazione delle Performance di un Catalizzatore a base di TiO_2 Supportato su Matrici Polimeriche", Bachelor's degree in "Industrial Chemistry"

-Lidia Mezzina, "Fotocatalizzatori Organici supportati su matrice polimerica: sintesi, caratterizzazione e studio preliminare della funzionalità fotocatalitica", Bachelor's degree in "Industrial Chemistry"

-Gisella Maria Di Mari, "Compositi a base di TiO_2 supportati su matrice polimerica: sintesi, caratterizzazione e studio delle prestazioni fotocatalitiche per l'abbattimento di inquinanti in fase acquosa", Master's degree in "Material Chemistry"

9.2 Scientific Disseminations

- 01\02\2018, Lecture at "Settimana della Cultura Scientifica" in Polymer's science (University of Catania, Department of Chemical Sciences)
- 21\02\2018 and 21/02/2019, Lectures at "Open Days" in Polymer science (University of Catania, Department of Chemical Sciences)
- 27/09/2018 and 27/09/2019 Presentations at "European Researcher's Night - Sharper" in Polymer Science, at University Square, Catania
- 25\01\2019 Lecture at Upper Secondary School "Rita Levi Montalcini" (Gagliano Castelferrato, Enna) in Polymer science, during the lessons of the "Piano Nazionale Lauree Scientifiche – Chimica"

9.3 Meeting Organization and Jury member

• Member of the administrative office of the XXXIII° National Conference of Italian Macromolecules Association (AIM)

• Jury member of "Premio Nazionale Divulgazione Scientifica – Giancarlo Dosi", during the editions 2018, 2019 and 2020

9.4 Scientific training courses

Training courses at University of Palermo:

-21/05/2018 Prof. M. Cannas (University of Palermo), "Time resolved fluorescence measurements and their application to materials investigation"
-22/05/2018 Prof. F. Giacalone (University of Palermo), “Chemical functionalization of Carbon nanoforms”
-22/05/2018 Prof. F. Giannici (University of Palermo), “X-ray absorption spectroscopy”
-23/05/2018 Prof. F. Giacalone (University of Palermo), “Chemical functionalization of Carbon nanoforms”
-23/05/2018 Prof. F. Giannici (University of Palermo), “X-ray absorption spectroscopy”
-24/05/2018 Prof. S. Agnello (University of Palermo), “Raman and MicroRaman spectroscopy and their application to materials investigation"

9.5 Seminars attended

1. 24/11/2017 Prof. T. Ogura (Tokyo University), *“Industrial Applications of Interfacial Science Techniques for Household products”*
2. 12/12/2017 Dr. G. Brancato (Scuola normale superiore di Pisa e INFN), *“Molecular modeling of engineered protein channels: MscL, Hemolysin and Ferritin as Test Cases”*
3. 31/01/2018 Dr. Dimitriya Bozukova, MOVERIM, Project Challenge (Horizon 2020), *“Scientific peer-review article writing”*
4. 22/03/2018 Prof. Paola E. Colavita, School of Chemistry and AMBER Research centre, Trinity College Dublin, *“Saccharide functional layers: novel scalable tools for surface biomimicry”*
5. 02/05/2018 Prof. Felix Juan Zamora Abanades, Department of Inorganic Chemistry, Universidad autónoma de Madrid, *"New materials based on Covalent Organic Frameworks: From Design to Potential Applications"*
6. 08/05/2018 Prof. Ayse Karakeçili, Faculty of engineering, chemical engineering department, Ankara University, *“Tissue engineering scaffolds: from 3D porous structures to hydrogels”*
7. 30/05/2018 Dr. Izabela Firkovska Boden, OttoSchott Institute of Materials Research (OSIM), Friedrich Schiller University of Jena (Germany), *“Simplistic Approach toward Advanced Bio- and Thermal Management Materials”*
8. 30/05/2018 Prof. Klaus D. Jandt, Chair of Materials Science, OttoSchott Institute of Materials Research (OSIM), Friedrich Schiller University of Jena (Germany), *“Advances in Polymer Matric-CNT nanocomposite: to make outstanding CNT properties Accessible”*

9. 01/06/2018 Prof. Klaus D. Jandt, Chair of Materials Science, OttoSchott Institute of Materials Research (OSIM), Friedrich Schiller University of Jena (Germany), *"Polymer-based Nanoparticle Libraries for targeted Anti-inflammatory Strategies"*
10. 20/09/2018 Prof. Roberto Paolesse, Università Tor Vergata, Roma (Italy), *"Porphyrinoids and chemical sensors: developments and applications"*
11. 30/10/2018 Prof. Paolo Samorì, Institut de Sciences et d'Ingégnerie Supramoléculaires, Université de Strasbourg & CNRS, Strasbourg (France), *"Nanomaterials properties tuned by their environment: integrating supramolecular concepts into sensing devices"*
12. 29/11/2018 Prof. Liliya A. Yatsunyk, Department of Chemistr and Biochemistry, Swarthmore College, Pennsylvania (USA), *"Biophysical and structural investigations of non-canonical DNA implicated in cancer"*
13. 17/04/2019 PhD. Peter Korevaar, Radboud University Nijmegen, *"Non-equilibrium approaches in adaptive and self-assembling life-like systems"*
14. 17/05/2019 Prof. Joanna Aizenberg, Harvard University, *"When Chemistry meets biology, optics and surface nanoscience"*
15. 18/06/2019 Prof. Kerstin G. Blanck, Max Planck Institute, Germany, *"Coiled coils as Molecular force sensors"*